2024-2025 Spring Semester-Department of Physics

Faculty of Art and Science

Entropy Analysis in Qubit and Qutrit Systems and the Behavior of Entropy During the Quantum Teleportation

Uğur Yerlikaya-21022902

Advisor: Prof.Dr.Orhan Özdemir

ABSTRACT

This study investigates the behavior of von Neumann entropy in qubit and qutrit systems, with a particular focus on how entropy evolves during the process of quantum teleportation. After discussing the theoretical background of entropy and quantum information, the von Neumann entropy was calculated for randomly generated qubit and qutrit states. Numerical simulations using the QuTiP library showed that entropy increases when the probability amplitudes become more balanced. In the second part of the study, the quantum teleportation protocol was simulated, and entropy was measured at each step. The results demonstrate that although entropy appears to fluctuate during the process, it returns to its original value after successful teleportation, indicating the preservation of quantum information. These findings provide further insights into the informational structure of quantum systems.

.

SHANNON ENTROPY

To understand Shannon entropy, we must first introduce the concept of an unknown event. Let us consider a random variable X as an example. X is a random variable whose value becomes known only upon measurement. The Shannon entropy of quantifies the amount of uncertainty that exists before the value of is learned.In other words, Shannon entropy measures the uncertainty present in a physical system prior to any observation.

This idea can be illustrated with a simple analogy involving a six-faced dice. In an ideal case—where the dice is perfectly balanced—each face has an equal probability of of appearing. Before rolling the dice, attempting to guess the outcome is highly uncertain, and the probability of correctly guessing the result is very low.Thus, before the measurement, the system exhibits maximum uncertainty.When the die is rolled and the outcome is observed, the amount of information gained is at its maximum as well.Both perspectives indicate that the system's entropy is at its highest value.

This analogy highlights an important point: when all possible outcomes are distributed symmetrically (each outcome is equally probable), the entropy reaches its maximum value.
Shannon entropy becomes particularly powerful in real-life applications because it provides a rigorous method to quantify uncertainty in probabilistic systems.

With this understanding, the Shannon entropy can be mathematically defined as a function of the probability distribution

$$H(X) \equiv H(p_1, \ldots, p_n) \equiv -\sum_x p_x \log p_x.$$

VON NEUAMANN ENTROPY

Von Neumann entropy is basically the quantum analogue of Shannon entropy, and their mathematical forms are very similar..To calculate von Neumann entropy, we first introduce the density matrix of the system:

$$S(\rho) \equiv -\mathrm{tr}(\rho \log \rho).$$

Where p is the density oparator: |Ψ><Ψ|= p.

QUANTUM TEELPORTATİON

Quantum teleportation is a technology that enables the transfer of an exact quantum state from one location to another without any physical connection. While classical communication is still required for transmitting certain information, the quantum state itself can be transferred without any physical link. This seemingly "spooky" transmission is made possible through a quantum phenomenon we discussed earlier: entanglement

MATERİAL AND METHODS

In this study, all quantum simulations and von Neumann entropy calculations were performed using the Python programming language and the open-source QuTiP (Quantum Toolbox in Python) library. Qubit and qutrit systems were defined, and their corresponding density matrices were obtained. Entropy values were then calculated numerically based on these density matrices. The quantum teleportation protocol was modeled step by step, and the behavior of entropy was analyzed throughout the process. All simulations were carried out in the Jupyter Notebook environment.

NUMERICAL ENTROPY ANALYSIS OF QUBITS AND QUTRTIS

QUBİTS

In this section, the analysis of qubits begins with the construction of a simple pure qubit state.

$$|\psi\rangle = a|0\rangle + b|1\rangle$$

When constructing a qubit, special attention must be given to the coefficients. Since the analysis will be conducted numerically, these coefficients will be randomly chosen for each simulation. However, it is essential that the sum of the squares of the absolute values of the coefficients always equals one. Otherwise, the qubit would not be considered well-defined.And that will directly effect our result.

For this reason, two random variables must be selected from the interval [0,1]. These variables will later be normalized to ensure that the resulting qubit state is valid.

Let randvar1 and randvar2 be the randomly generated values. The normalized coefficients and are then defined as:
With this construction, the qubit is now properly defined and ready for entropy calculations.
When we examined the qubits that genrated the difference between coefficients, we observed a clear pattern: the closer a and b are to each other, the higher the entropy becomes.
This relation was also visualized in a graph, showing that entropy is directly affected by how balanced the coefficients are.

$$a = \frac{\mathrm{randvar}_1}{\sqrt{|\mathrm{randvar}_1|^2+|\mathrm{randvar}_2|^2}} \qquad b = \frac{\mathrm{randvar}_2}{\sqrt{|\mathrm{randvar}_1|^2+|\mathrm{randvar}_2|^2}}$$

$$|a|^2 + |b|^2 = 1$$

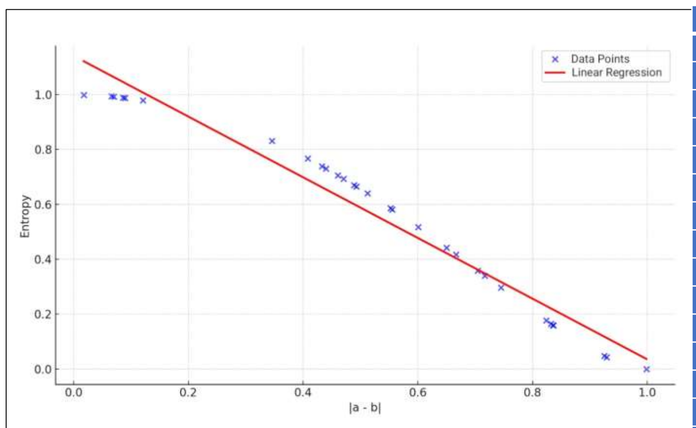

Qubit	a	b	Entropy
1	0.001588	0.999999	0.000051
2	0.997633	0.068765	0.043332
3	0.072348	0.997379	0.047195
4	0.152049	0.988373	0.158612
5	0.152892	0.988243	0.159998
6	0.987759	0.155985	0.165114
7	0.986611	0.163094	0.177041
8	0.973468	0.228825	0.296343
9	0.967930	0.251219	0.339673
10	0.260598	0.964547	0.358080
11	0.290383	0.956910	0.417230
12	0.953032	0.302869	0.442217
13	0.940426	0.339997	0.516574
14	0.927885	0.372866	0.581690
15	0.374920	0.927057	0.585717

QUTRTİS:

When analyzing the behavior of entropy in qutrits, we follow a very similar approach to that used in the analysis of qubits Our qutrit is constructed as shown below:

$$|\psi\rangle = a|0\rangle + b|1\rangle + c|2\rangle \qquad |a|^2 + |b|^2 + |c|^2 = 1$$

After constructing valid qutrit states with normalized coefficients we analyzed the relationship between these coefficients and the resulting von Neumann entropy.The analysis showed that entropy increases as the coefficients become more balanced. The corresponding graph for qutrits illustrating this pattern are presented below.

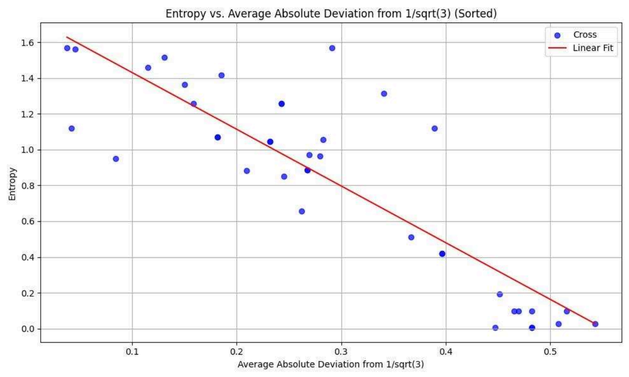

Von Neuamn Entropy For Qubits in Quantum Teleportaion

In this section, we analyze the changes in the von Neumann entropy of qubits at each step of the quantum teleportation process. Unlike in the previous section where we examined qubits and qutrits with random coefficients, here we will use fixed coefficients. For the sake of clarity and simplification, we set the entropy to its maximum value by choosing a=b=1/√2. This choice makes the analysis more straightforward.

The qubit system was analyzed through the four main steps of quantum teleportation, and entropy was measured at each stage.The graph below shows that entropy temporarily exceeds its expected maximum (reaching) but returns to its original value by the end of the process.This demonstrates that quantum information—and thus von Neumann entropy—is fully preserved during teleportation.

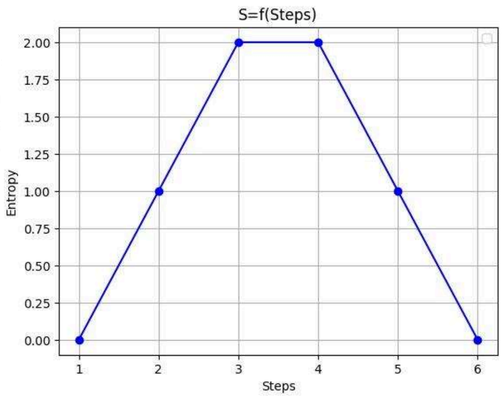

CONCLUSION

By analyzing von Neumann entropy in qubit and qutrit systems, this study provides a clearer understanding of how entropy behaves in different quantum structures.In the second part, the focus shifts to quantum teleportation, where entropy is tracked throughout the process. Although temporary increases are observed, the entropy eventually returns to its original value, confirming that quantum information remains preserved.Looking at teleportation from the perspective of information entropy may help us better understand how entropy can be used to influence or guide the teleportation process.

KAYNAKÇA

[1]Quantum Compıtation and Quanntum Information by Micheal A. Nielsen and Isaac L. Chuang
[2] Introduction to Quantum Mechanics Second Edition by David J. Griffiths.
[3] Modern Quantum Mechanics Revised Edition by J.J. Sakurai

YTU FACULTY of ARTS and SCIENCES

2024-2025 Spring Semester Department Of Physics

PARTICLE IDENTIFICATION WITH MACHINE LEARNING IN ALICE

Eren KÖYBAŞI 20022009

Supervisor: Prof.Dr.Ayben KARASU UYSAL

Abstract

This study explores the use of machine learning (ML) techniques for particle identification (PID) in heavy-ion collisions, focusing on the ALICE Experiment. It presents ML models developed for PID, emphasizing solutions to key challenges such as missing data and discrepancies between simulation and experimental results. An attention-based mechanism is introduced for handling incomplete data, and domain adaptation methods, including DANN, are used to address data mismatches. The integration of ML-based PID into the ALICE analysis framework is also discussed. Results demonstrate the potential of ML to enhance the efficiency and accuracy of particle physics analyses.

An Overview To ALICE

ALICE (A Large Ion Collider Experiment) is a detector at CERN designed to study heavy-ion collisions. It aims to explore the quark-gluon plasma that existed in the early moments of the universe. It is important for particle identification because it can distinguish a large number of low-momentum particles with high precision. This plays a critical role in understanding the behavior of the fundamental building blocks of matter. Below is a schematic view of the ALICE dedector and its particle identification performance. The figure shows dE/dx vs. momentum for ITS and TPC, β vs. momentum for TOF, and Cherenkov angle vs. momentum for HMPID. Each sub-detector contributes to particle separation in different momentum ranges [1].

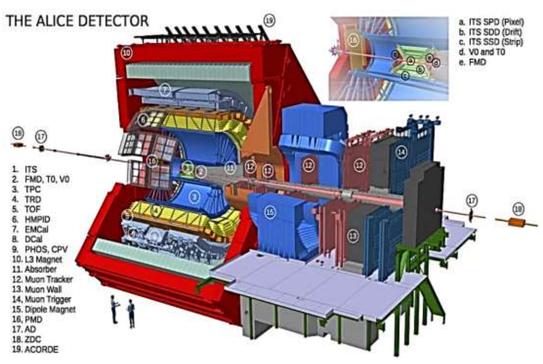

Figure 1: Components of the ALICE detector in its Run 2 configuration.

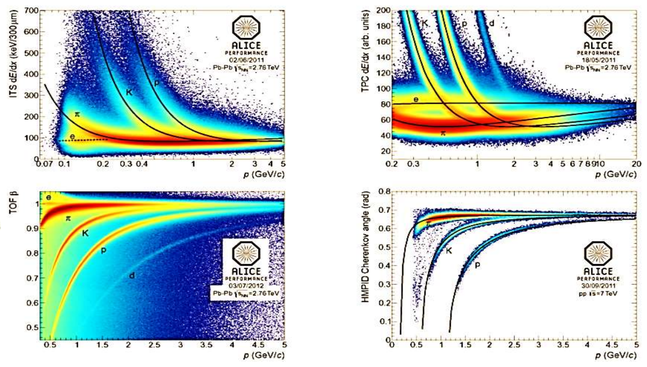

Figure 2: Schematic view of the ALICE dedector and its PID performance.

Methodology for Particle Identification

The machine learning model developed for particle identification in the ALICE experiment, capable of handling incomplete detector data and based on the attention mechanism:

- Converts input features (detector signals, momentum, spatial coordinates) into feature–value pairs.
- Transforms these pairs into embedded vectors processed by a Transformer encoder with multi-head self-attention.
- Summarizes variable-length inputs into a fixed-size vector using attention pooling.
- Applies a binary classifier for each particle type (one-vs-all strategy).
- Trains on both complete and incomplete data, eliminating the need for artificial data imputation or data loss [2].

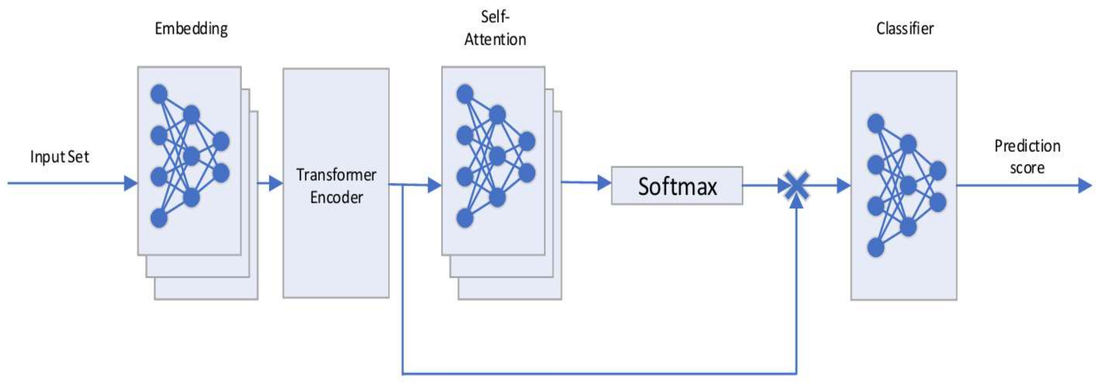

Figure 3: The proposed model architecture. The architecture applies stacked layers independently to each vector in the set, whereas standalone blocks operate on the input as a complete unit [2].

Model Architecture

- **Architecture:** 3 hidden layers with **64 → 32 → 16** neurons.
- **Activation:** ReLU, dropout rate = **0.1** after each layer.
- Imputation models: input size = **19** (all missing values filled).
- Ensemble: input sizes = **19, 17, 17, 15**, based on missing values in TOF/TRD (each has 2 features).
- **Embedding network:** 1 hidden layer (**128 → 32**)
- **Transformer encoder:** 2 layers, **2 heads**, dropout = 0.1
- **Self-attention pooling** to merge variable-length sets.
- **Classifier network:** hidden layer with **64 units**, output = 1
- Trained end-to-end on both **complete and incomplete data**, without imputation [2].

The Table of Layers and the Number of Neurons in Each Layer [2]

Embedding			Transformer Encoder						Self-Attention			Classifier		
			Encoder Layer					Num Layers						
			Multi-Head Attention		Neural Network									
Input	Hidden	Output	Dimension	Heads	Input	Hidden	Output		Input	Hidden	Output	Input	Hidden	Output
20	128	32	32	2	32	128	32	2	32	64	32	32	64	1

Dataset

- **Source**: Monte Carlo simulations of √s = 13 TeV pp collisions (PYTHIA 8 + GEANT, Run 2 detector conditions)
- **Size**: **2,751,934** tracks
- Features (19 total):
  - Detector responses: TPC (1), TOF (2), TRD (2)
  - Kinematic info: p_T, p_x, p_y, p_z, charge
  - Geometry: DCA (d_{xy}, d_z), spatial coords (x, y, z, α)
  - Track metadata (e.g., track type, cluster count)
- Only ~**37%** of samples are complete
- ~**63%** contain at least one missing value (mainly TOF & TRD) [2].

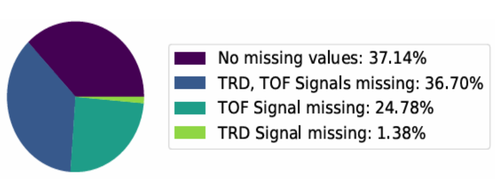

Figure 4: Missing values distribution. Over 62.8 of the examples are missing at least one value [2].

Results

All models are evaluated on both **complete and incomplete** data using standard classification metrics. Attention-based model consistently achieved **high performance across all particle types**, even when detector data was partially missing. To evaluate performance, the model is compared against a traditional PID method based on *nσ* cuts [2]:

- For particles with **transverse momentum** p_T < 0.5:
  - $|n_{\sigma,TPC}| < 3$
- For particles with transverse momentum p_T > 0.5:
  - $\sqrt{n_{\sigma,TPC}^2 + n_{\sigma,TOF}^2} < 3$

Classification results for kaon (on left) and proton (on right) identification using data with missing values [2].

Model	Precision	Recall	F_1
Standard	**92.87 ± 0.01**	60.37 ± 0.05	73.17 ± 1.57
Ensemble	91.18 ± 02.00	82.72 ± 01.42	86.74 ± 0.16
Mean	90.83 ± 01.71	82.32 ± 0.96	86.36 ± 0.34
Proposed	91.55 ± 0.71	**83.68 ± 0.82**	**87.44 ± 0.14**
Regression	91.17 ± 01.00	81.78 ± 0.21	86.22 ± 0.46

Model	Precision	Recall	F_1
Standard	**99.40 ± 0.01**	59.72 ± 0.03	74.61 ± 1.88
Ensemble	97.16 ± 0.46	93.74 ± 0.30	95.42 ± 0.12
Mean	97.85 ± 0.41	93.34 ± 0.32	95.54 ± 0.06
Proposed	97.80 ± 0.44	**93.86 ± 0.27**	**95.79 ± 0.07**
Regression	97.38 ± 0.40	93.67 ± 0.38	95.49 ± 0.15

To complement the numerical results, key performance metrics are **visualized** through:

- **Precision–Recall and PR curves** for the classification tasks.
- Metric comparisons across different **momentum (p_T) intervals**,

Performance of different PID methods in kaon selection task as a function of particle momentum and PR curve for different ML based approaches with missing data [2].

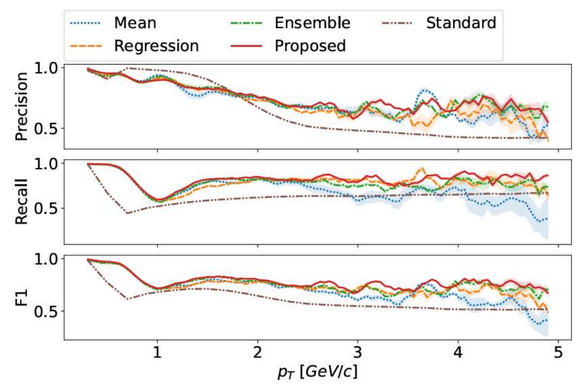

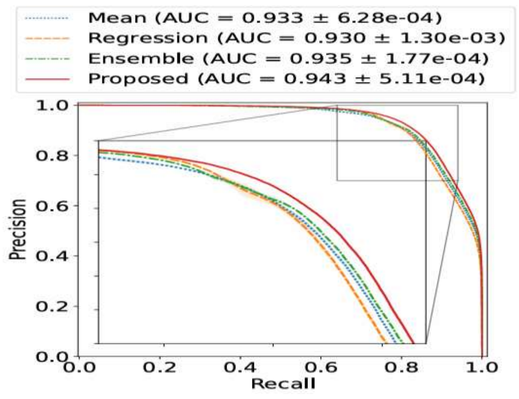

Performance of different PID methods in proton selection task as a function of particle momentum and PR curve for different ML based approaches with missing data [2].

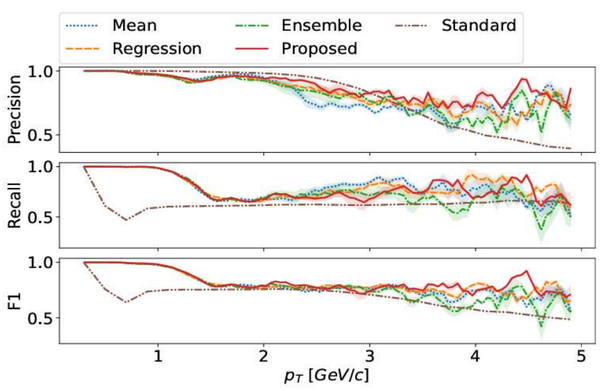

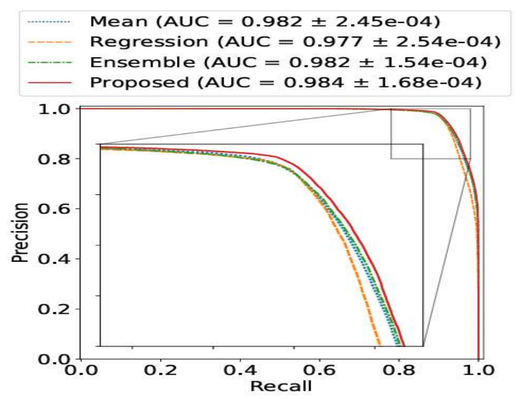

Future Works

- With Run 4 bringing a tenfold increase in data, AI-based analysis will become essential [3].
- Physics-Informed Neural Networks (PINNs) offer promising tools for integrating physical laws into learning [3], improving robustness and enabling rare event detection [4].
- CNNs and RNNs can support anomaly detection and temporal event modeling [4].

.

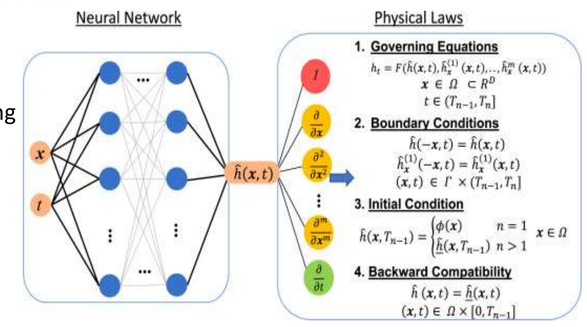

Figure 5: Physics Informed Neural Networks [4].

Bibliography

[1] K. Aamodt et al. The ALICE experiment at the CERN LHC. JINST, 3:S08002,2008
[2] Milosz Kasak, et.al. Machine-learning-based particle identification with missing data. The European Physical Journal C, 84(7), July2024
[3] C. L. Wight and J. Zhao, "Solving Allen-Cahn and Cahn-Hilliard equations using the adaptive physics informed neural networks," arXiv preprint arXiv:2007.04542, 2020.
[4] Maja Karwowska, et.al. Particle identification with machine learning in ALICE Run 3.EPJ Web Conf., 295:09029, 2024

2024-2025 Bahar Yarıyılı

FİZİK BÖLÜMÜ

Konvansiyonel MV Foton Lineer Hızlandırıcılara Karşı Inverse-Compton (ICS) Kaynaklı X/γ-Işınları: Fiziksel Temeller, Klinik Potansiyel ve Gelecek Perspektifi

Ahmet KUZYURT 2102084

Danışman: Mehmet KILIÇ

ÖZET

Günümüz radyoterapisinde altın standart kabul edilen 6 MV foton lineer hızlandırıcıları (linac) son yıllarda kompakt inverse-Compton (ICS) kaynaklı X/γ-ışınlarıyla kıyaslanma durumuna gelmiştir. Bu çalışma, linac ve ICS sistemlerini **enerji spektrumu, doz dağılımı, dozimetrik belirsizlik ve maliyet–altyapı gereksinimi** açısından kapsamlı biçimde karşılaştırmaktadır. İlk aşamada linac'ın geniş bant bremsstrahlung spektrumu (2–6 MeV) ile BriXS (60 keV) ve ThomX (90 keV) ICS prototiplerinin dar bant (ΔE/E ≈ %3) demetleri Monte Carlo yöntemiyle modellenmiştir. 30×30×30 cm^3 su fantomunda yapılan simülasyonlar, linac'ta yüzde derinlik-doz eğrisinin 10 cm'de %67'ye düştüğünü; ICS'te ise dozun 1 cm'de %65, 10 cm'de yalnızca %2 seviyesine indiğini göstermiştir. TG-51 protokolü kullanılarak linac kanalında toplam doz belirsizliği ±0,8 %'e indirilirken, < 100 keV su-dozu standardının eksikliği nedeniyle ICS kanalında belirsizlik ±1,8 % olarak hesaplanmıştır. Kalkan hesapları, linac odasında 1,8 m beton gerektirirken ICS için 0,4 m betonun yeterli olduğunu ortaya koymuş; buna rağmen 10 yıllık toplam maliyetin ICS için linac'ın yaklaşık 1,4 katı olduğu belirlenmiştir. SWOT analizi, ICS'nin düşük kalkan gereksinimi ve faz-kontrast görüntü potansiyelini "fırsat", düşük doz-hızı ile belirsiz k_Q değerlerini ise "tehdit" olarak öne çıkarmıştır. Sonuç olarak ICS kaynakları yüzeyel lezyon ve görüntü-yönlendirmeli uygulamalar için umut verici görünmekte; ancak klinik yaygınlık, <100 keV birincil standardın geliştirilmesi ve doz-hızın ≥ 0,5 Gy dk^{-1} eşiğine çıkarılmasına bağlıdır.

AMAÇLAR

- Linac & ICS demet parametrelerini karşılaştırmak
- PDD eğrilerini üst üste analiz etmek
- k_Q/ belirsizlik bütçesini çıkarmak
- Bunker ve CAPEX farkını hesaplamak
- SWOT ile klinik yaygınlık potansiyelini değerlendirmek

k_Q FAKTÖRÜ

k_Q, bir iyonizasyon odasının ^{60}Co'da kalibre edilmiş mutlak doz katsayısını ($N_{D,w}^{60Co}$) ölçüm yapmak istediğiniz başka bir ışın kalitesine (Q) uyarlamak için kullanılan "ışın kalitesi düzeltme katsayısıdır."

$$N_{D,w}^{Q} = k_Q \cdot N_{D,w}^{60Co}$$

INVERSE-COMPTON KAYNAKLI X/γ-IŞINLARI

Inverse-Compton saçılması, relativistik (≈ MeV–GeV) elektronların düşük enerjili lazer fotonlarını (kızıl-ötesi veya görünür) "ters yönde" saçıp foton enerjisini X veya γ bandına (10 keV – tens MeV) yükseltmesidir. Klasik Compton olayında elektron dinlenim hâlindedir; "inverse" versiyonunda enerjisi çok yüksek olan elektron, fotondan aslen "enerji çalar" – fakat elektron zaten relativistik olduğu için sonuçta foton enerjisi büyük oranda artar.

6 MV LINAC

6 MV linac, derin yerleşimli tümörler için yüksek doz iletimini ve modüle edilebilir alanları ekonomik zaman diliminde sağlayan, klinikte standardize edilmiş bir foton kaynağıdır; ancak kompakt inverse-Compton sistemlerinin sunduğu düşük kalkan gereksinimi ve dar-bant spektrum avantajlarını sağlamaz.

BRIXS (BRIGHT X-RAY SOURCE) PROTOTİPİ

BriXS, "mini-senkrotron" parlaklığını **laboratuvar ölçeğinde** sunmayı hedefleyen doğrusal (linac-tabanlı) bir inverse-Compton (ICS) ışın kaynağıdır.

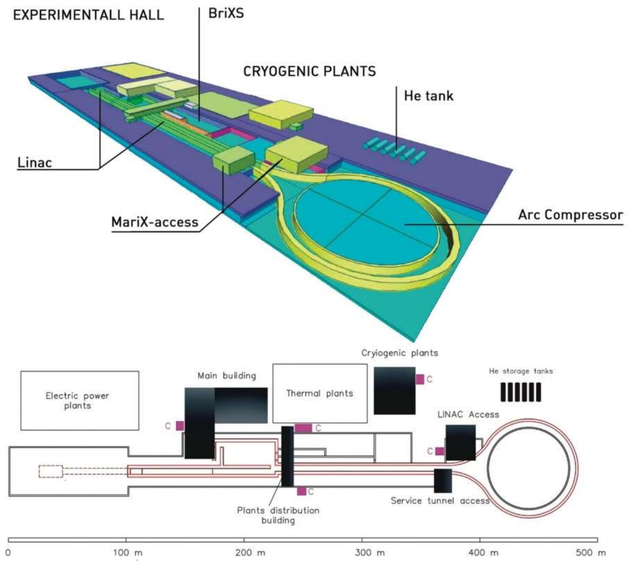

THOMX (THOMSON X-RAY) PROTOTİPİ

ThomX, **depohalkası tabanlı** (storage-ring) inverse-Compton kaynağıdır; amacı, tıp ve endüstride kullanılan 40–90 keV monokromatik demet talebini ring mimarisiyle karşılamaktır.

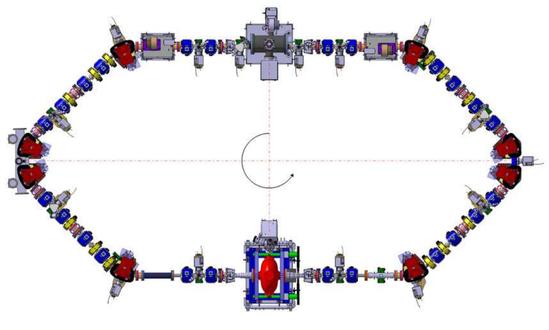

MATERYAL & YÖNTEM

Donanım: 6 MV Elekta Versa HD linac; BriXS-60 keV ve ThomX-90 keV ICS prototip spektrumları
Dozimetri: PTW 30013 Farmer odası ($N_{D,w}^{60Co}$= 5,133 x 10^7 Gy/C), EBT-XD film, TLD-100 doğrulaması
Simülasyon: Geant4 10.7 + G4EmLivermore, 1×10^8 foton, 30×30×30 cm^3 su fantomu
Maliyet: NCRP-151 kalkan formülleri & üretici katalog verileri

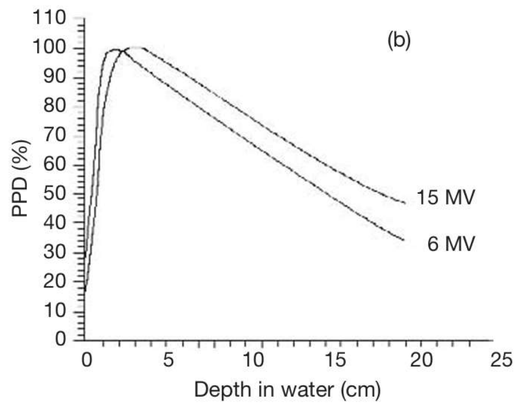

Şekil 2.1 100 cm SSD ve 10 x 10 cm^2 alan boyutu için 6 MV ve 15 MV foton demetleriyle su içinde elde edilen tipik merkez eksen PDD eğrileri.

SONUÇLAR

Ölçüt	Linac 6 MV	ICS 60 keV	ICS 90 keV
%dd(10)	67 %	2 %	4 %
Toplam belirsizlik (k = 1)	±0,8 %	±1,8 %	±1,6 %
Beton kalkan kalınlığı	1,80 m	0,40 m	0,45 m
10 y CAPEX	7,6 M $	10,3 M $	12,5 M $

- ICS, yüzeysel bölgede doz yoğunluğunu arttırırken derin dokuda doz %2'nin altına düşer.
- < 100 keV su-dozu standardı mevcut olmadığından belirsizlik hedef sınır (± 1,5 %) aşılmıştır.
- Beton kalkan %78 azalmasına rağmen toplam maliyet artmıştır.

BUNKER VE KALKAN HESAPLARI

Linac (6 MV): NCRP-151 formülüyle 100 cm SSD, 1* Gy haftalık iş yükü için 1,8 m beton + 4 mm kurşun kaplama gerekir
ICS (60-90 keV): 3 mm Cu HVL, saçılma faktörü 0.05; aynı iş yükü için .4 m beton gereklidir. Kalkan kalınlığı yaklaşık olarak 4.5 kat azalır.

SWOT ANALİZİ

	Güçlü Yanlar	Zayıf Yanlar
Linac	Yüksek doz-hızı; IMRT/VMAT olgun teknoloji	Kalın beton; geniş oda; >10 MV'de nötron riski
ICS	Düşük kalkan; faz-kontrast görüntü; yüzeyel RT	Düşük doz-hızı; <100 keV k_Q belirsizliği

SONUÇ VE ÖNERİLER

- ICS kaynakları, cilt lezyonları ve faz-kontrast görüntülemeye yönelik düşük kalkanlı bir seçenek sunar.
- Derin tümör tedavisi için doz-hız ≥ 0,5 Gy dk^{-1} seviyesine çıkarılmalıdır.
- NPL/PTB < 100 keV su kalorimetresinin devreye girmesiyle belirsizlik ± 1,2 % altına düşebilir.
- Teknik olgunlaşma sonrasında ilk klinik nişler: veteriner onkoloji, biyopsi rehberli mikro-CT

KAYNAKÇA

[1] **IAEA**, *Absorbed Dose Determination in External Beam Radiotherapy: An International Code of Practice* (TRS-398), Uluslararası Atom Enerjisi Ajansı, Viyana, 2000.
[2] S. **Liu**, W. **Huang**, H. **Li** ve X. C. **Tang**, "Monte Carlo modelling of a compact inverse-Compton X-ray source for medical applications," *Phys. Med. Biol.*, cilt 64, 085008, 2019.
[3] D. W. O. **Rogers**, "The Physics of the AAPM's TG-51 Protocol," *Clinical Dosimetry Measurements in Radiotherapy*, AAPM Summer School Monograph 34, pp. 233–272, 2009.

YTÜ FEN EDEBİYAT FAKÜLTESİ

2024-2025 Bahar Yarıyılı

FİZİK BÖLÜMÜ

Investigation of Supercapacitor Performance of Fe-S Active Material on Copper Current Collector

Muharrem COŞKUN 19022058

Supervisor: Prof.Dr. Zeynep Güven Özdemir

In response to growing global energy demands and environmental concerns, this research focuses on advancing supercapacitor technology by addressing its primary limitation: energy density. To solve this, iron sulfide (FeS)—a material known for its low cost, natural abundance, and high theoretical pseudocapacitance—was chosen as the active electrode material. The FeS electrodes were fabricated using a hydrothermal synthesis method followed by a uniform deposition onto a copper current collector via spin coating. The electrochemical performance was then systematically evaluated using cyclic voltammetry (CV) and galvanostatic charge-discharge (GCD) techniques in a 1 M KOH electrolyte. The investigation revealed exceptional results, with the electrode achieving a maximum specific capacitance of 321.74 F/g at a current density of 1 A/g, a value that surpasses many previously reported FeS-based systems. While the capacitance decreased at higher charge-discharge rates, it notably stabilized around 66 F/g above 3 A/g, demonstrating the material's excellent structural integrity and cyclic reversibility. Ultimately, these compelling findings establish the hydrothermally synthesized FeS electrode as a highly promising and competitive candidate for developing next-generation, high-performance supercapacitors.

Energy Storage

Here is a condensed version of the text:

Energy storage, the process of saving energy for later use, aims to improve efficiency, reduce environmental impact, and ensure a stable energy supply. It has become essential due to the limitations and environmental damage of traditional fossil fuels and the critical need to integrate variable renewable sources like wind and solar into the modern electricity grid. By reducing power fluctuations, storage systems increase grid stability and flexibility. Major energy storage technologies are classified into four categories: mechanical (e.g., pumped hydro), electrical (superconductors), chemical (batteries), and magnetic (supercapacitors).

Supercapasitör

Supercapacitors (SCs) are advanced energy storage devices that store energy electrostatically, offering exceptional power performance and an extremely long cycle life. They achieve capacitance values thousands of times higher than traditional capacitors by using advanced electrode materials and two key storage mechanisms: electric double-layer formation and pseudocapacitive redox reactions. This unique combination allows supercapacitors to bridge the performance gap between conventional capacitors and batteries, delivering both high power and significant energy density.

In this prepared sample, our first step involved precisely cutting our copper plate to dimensions of 2 cm by 3 cm. This plate then served as the surface onto which our active FeS material would be deposited. Subsequently, we prepared the precursor solution for synthesis: we dissolved 0.075 mmol of thiourea and 0.075 mol of iron(III) chloride in 25 mL of hydrazine hydrate, ensuring a homogeneous mixture through continuous stirring with a magnetic stirrer. This solution was critically important for the formation of the FeS coating on the copper plate.

In this study, FeS-coated supercapacitor electrodes were fabricated via a hydrothermal synthesis method. A precursor solution of thiourea, iron(III) chloride, and hydrazine hydrate was used to synthesize FeS, which was subsequently deposited onto a 2x3 cm copper substrate using spin coating. Each electrode contained approximately 0.001 g of active FeS material. The electrochemical performance was then evaluated in a 1 M KOH electrolyte using a potentiostat–galvanostat. Key characteristics were determined through cyclic voltammetry (CV) at scan rates of 20-200 mV/s and galvanostatic charge-discharge (GCD) tests at current densities of 1-5 A/g to assess the electrode's specific capacitance and overall performance for comparison with existing literature.

$$c_p = \frac{A}{2\nu\Delta V m}\,(F/g) \quad (1)$$

$$E = \frac{1}{2} c_p (\Delta V)^2\,(Wh/kg) \quad (2)$$

$$P = \frac{E}{\Delta t}\,(W/kg) \quad (3)$$

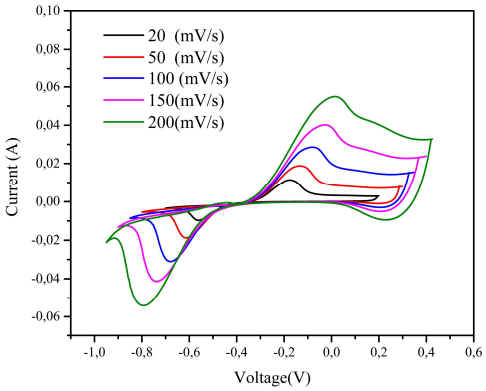

Graph 1. CV graph of FeS active materials

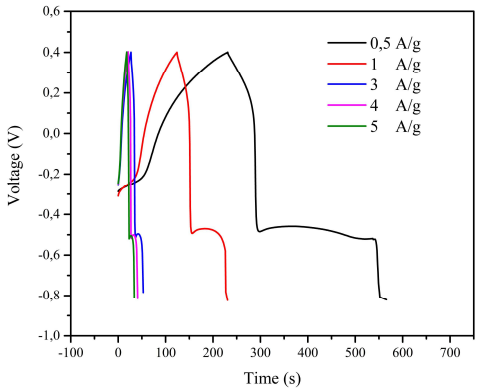

Graph 1. CV graph of FeS active materials

Table 1

Study	Scan Rate (V/s)	Specific Capacitance (F/g)	Electrode Material	Synthesis Method
This Study	0.02	91.18	FeS	Hydrothermal (Thioacetamide + FeCl3 in hydrazine)
Zhou et al.	0.02	82	FeS-Graphene	Hydrothermal
Fe_3O_4/rGO	0.02	88	Fe_3O_4/rGO	Hydrothermal
Fe_3O_4*C	0.02	72	Fe_3O_4–C Hybrid	Oolite-filled tubular structure

Table 2

Electrode Material	Technique	Electrolyte	Scan Rate (V/s)	CV Capacitance (F/g)
FeS	Hydrothermal	1 M KOH	0.02	91.18
MnO_2 on CNTs	Electrodeposition	1 M Na_2SO_4	0.01	275
Fe_3O_4–C	Oolitic templated	6 M KOH	0.01	178
Co_3O_4/Ni foam	Solvothermal	2 M KOH	0.01	210
$NiCo_2S_4$-rGO	Hydrothermal	6 M KOH	0.01	395
Mn_3O_4 nanospheres	Sol-gel	1 M Na_2SO_4	0.01	160

Table 3

Study	Current Density (A/g)	Specific Capacitance (F/g)	Electrode Material	Synthesis Method
This Study	1	321.74	FeS	Hydrothermal (Thioacetamide + FeCl3 in hydrazine)
Zhou et al.	1	308	FeS on Ni Foam	Hydrothermal
Fe_3O_4/rGO	1	661	Fe_3O_4/rGO	Hydrothermal
Fe_3O_4–C	1	178	Mn_3O_4–Fe_3O_4–C	Oolite-filled tubular structure

Table 4

Elektrot Malzemesi	Akım Yoğunluğu (A/g)	GCD Kapasitansı (F/g)
This Study (FeS)	1	321.74
This Study (FeS)	2	208
This Study (FeS)	3	66
$NiMnO_3$ on carbon cloth	1	2330
Fe_3O_4/rGO	1	661
Fe_3O_4–C	1	178
FeS–W_xO_m Composite	1	558
MoS2–FeS_2 Core–Shell	1	386
β-Ni(OH)₂ Nanoplates on Graphene (G)	2.8	1335
β-Ni(OH)₂ Nanoplates on G	45.7	953
RGO–CNT–WO_3	2	633.3

Our CV data provides a clear picture of the electrochemical behavior and, specifically, the rate dependency of our FeS-coated electrode. The highest specific capacitance of 91.175 F/g, achieved at our lowest scan rate of 0.02 V/s, underscores the electrode's capacitive potential and its efficient interaction with the electrolyte at slower rates. This suggests that all active sites on and within your material are accessible to ions, allowing optimal charge storage mechanisms to occur. However, a gradual decrease in specific capacitance is quite evident as the scan rate increases: to 74.775 F/g at 0.05 V/s, 65.832 F/g at 0.1 V/s, 64.099 F/g at 0.15 V/s, and 68.542 F/g at 0.2 V/s. This decline is a common phenomenon in supercapacitor electrodes, primarily attributed to ion diffusion limitations. At higher scan rates, electrolyte ions simply cannot penetrate the electrode's porous structure or reach all active sites quickly enough, hindering the full contribution of the active material to the capacitance. This CV trend is consistent with the rate dependency observed in our GCD data, where capacitance also decreased with increasing current density. Both measurements indicate that while your electrode performs excellently at lower rates, there is potential for optimizing ion transport kinetics or material morphology for high-rate applications, focusing on factors like porosity, surface area, or electrical conductivity to enhance overall high-rate performance. Our GCD data, presented visually, clearly illustrates the capacitive behavior and performance of your FeS-coated electrode across different current densities.At your lowest current density of 1 A/g, you achieved a specific capacitance of 321.7391 F/g. This value strongly indicates the high energy storage potential of your electrode and suggests that its active sites are efficiently accessed by electrolyte ions, allowing for optimal charge storage mechanisms at lower charge-discharge rates. However, a noticeable decrease in capacitance is observed as the current density increases. The capacitance drops to 208 F/g at 2 A/g. This initial sharp decline suggests that your electrode experiences some limitations when transitioning to higher rates. Subsequently, as the current density is further increased, the capacitance stabilizes considerably, showing values around 66.10169 F/g at 3 A/g, 66.1157 F/g at 4 A/g, and 66.66667 F/g at 5 A/g. This stabilization implies that while the material maintains its capacity beyond a certain high current density, it can only utilize a fraction of its maximum potential under such conditions. Overall, this trend highlights rate capability challenges commonly encountered in supercapacitor electrodes. At high current densities, electrolyte ions face difficulties rapidly penetrating the electrode's internal porous structure and interacting with all active sites, primarily due to ion diffusion limitations. Your data strongly suggests that while your FeS-coated electrode is well-suited for low-rate energy storage applications, optimizing ion transport kinetics and active material utilization through structural modifications (such as enhancing porosity, surface area, or electrical conductivity) may be necessary for high-power demanding scenarios

[1] Riaz, J., Aslam, F., Arif, M., Huma, T., & Bibi, A. (2025). First investigation of high-performance FeS-based W 18 O 49 asymmetric supercapacitors operating at 1.6 V. Nanoscale Advances, 7(1), 231-241.

[2] Lin, T. W., Dai, C. S., & Hung, K. C. (2014). High energy density asymmetric supercapacitor based on NiOOH/Ni3S2/3D graphene and Fe3O4/graphene composite electrodes. *Scientific reports*, *4*(1), 7274.

[3] Ran, J., Liu, Y., Yang, T., Feng, H., Zhan, H., & Shi, H. (2023). MnO2- MoS2/RGO hollow structure as high-performance supercapacitor electrode materials. *Journal of Energy Storage*, *64*, 107216.

YTU FACULTY of ARTS and SCIENCES

2024-2025 Spring Semester Department of Physics

UNDERSTANDING THE AdS/CFT CORRESPONDENCE: A THEORETICAL APPROACH

Muhammed Yusuf ŞAHİN 21022002

Supervisor: Prof. Dr. Ayben KARASU UYSAL

ABSTRACT

The AdS/CFT correspondence was studied as a tool to understand weakly interacting duals of strongly coupled quantum systems through classical gravity. The Ryu–Takayanagi prescription was applied to compute entanglement entropy for a ball-shaped region in CFT_2, reproducing the expected logarithmic behaviour. The quark-gluon plasma was modelled using a black hole in AdS_5, and the universal result for shear viscosity to entropy density ratio, $\eta/s = 1/4\pi$, was derived. These applications illustrate how geometric methods offer insights into strongly coupled quantum systems and demonstrate the unlimited potential of the correspondence in distinct fields in physics.

INTRODUCTION

The AdS/CFT correspondence is a revolutionary duality in theoretical physics, relating a gravitational theory in Anti-de Sitter space to a conformal field theory on its boundary. Initially emerging from string theory with Maldacena's argument, it has since evolved into a universal tool for probing quantum gravity and strongly coupled field theories.

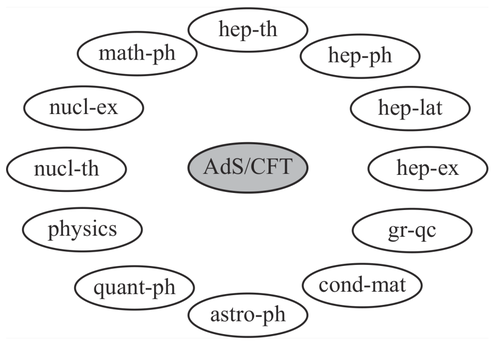

Its impact spans across physics — from high-energy collisions, lattice simulations, and astrophysics, to quantum information and condensed matter. To this day, it has enjoyed a wide ranging spectrum of interest among physicists and enjoys a prominent place at the forefront of modern mathematical physics.

THE LARGE-Nc LIMIT OF GAUGE THEORIES

In 1974, t'Hooft formulated a strong relation between quark diagrams and topology. This revealed the first hints of the duality.

There are three colors in QCD, but in the large-Nc gauge theory, one considers a large number of colors. There are two parameters in QCD, the coupling constant *g* and the number of colours Nc. Here, the t'Hooft coupling λ is defined and used. Double-line notation is used for tracking color flow.

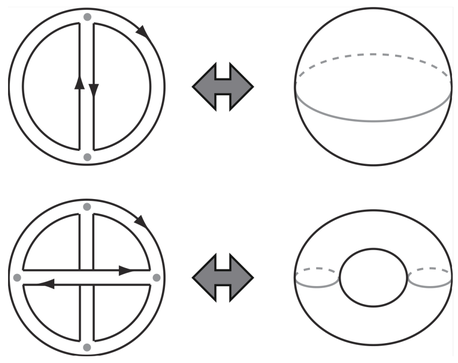

From the Feynman rules, one can get for the amplitudes

$$\left(\frac{N_c}{\lambda}\right)^V \left(\frac{\lambda}{N_c}\right)^E N_c^F = \lambda^{E-V} N_c^{V-E+F}$$

Planar diagram in the figure scales as

$$\left(\frac{N_c}{\lambda}\right)^2 \left(\frac{\lambda}{N_c}\right)^3 N_c^3 = \lambda N_c^2$$

and the non-planar as

$$\left(\frac{N_c}{\lambda}\right)^4 \left(\frac{\lambda}{N_c}\right)^6 N_c^2 = \lambda^2$$

In the limit Nc → ∞ with $\lambda := g_{YM}^2 N_c$ fixed and large, planar (sphere-like) diagrams dominate and the gauge theory is simplified. Each diagram forms a discretised 2D surface, with its topology (genus, *h*) determining its Nc -scaling. This yields a topological expansion that reorganises the usual perturbative loop expansion of QCD.

$$\ln Z_{\text{gauge}} = \sum_{h=0}^{\infty} N_c^{2-2h} f_h(\lambda)$$

This structure mirrors the genus expansion of the string partition function [2].

MALDACENA'S CONJECTURE

In November 1997, a groundbreaking duality was proposed by Juan Maldacena that has since become recognised as one of the most profound insights in theoretical physics.

Nc = rank of the gauge group, number of colours

λ = The t'Hooft Coupling

$$N_c^2 = \frac{\pi}{2}\frac{L^3}{G_5}\,, \qquad \lambda = \left(\frac{L}{l_s}\right)^4$$

L: AdS radius

ℓs: string length

G_5: 5D Newton Constant

These results relate gauge and string theory parameters and are known as the *AdS/CFT Dictionary*. The dictionary maps difficult to calculate gauge dynamics to tractable classical gravity in AdS [1].

THE RYU-TAKAYANAGI CONJECTURE

$$S_A = \frac{\text{Area of } \gamma_A}{4G_N^{(d+2)}}$$

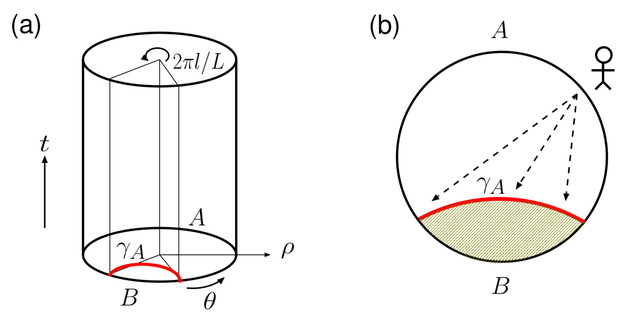

In light of AdS/CFT, the conjecture states that the entanglement entropy of a CFT region A is computed by the codimension-2 bulk surface γ_A minimising area, analogous to the Bekenstein-Hawking formula. In the figure, (a) a boundary region *A* in CFT_2 corresponds to a minimal surface in the bulk AdS_3, whose area gives the entanglement entropy. (b) The geodesic's — here, a semicircle — minimal surface γ_A is anchored to a spatial interval *A* on the boundary and plays the role of a holographic screen for an observer in *A* [3].

THE QUARK-GLUON PLASMA

The vertical axis represents temperature, and the horizontal axis represents the baryon chemical potential. "χSB" (chiral symmetry breaking) region represents the hadron phase or confinement, and "CSC" represents the colour superconducting phase.

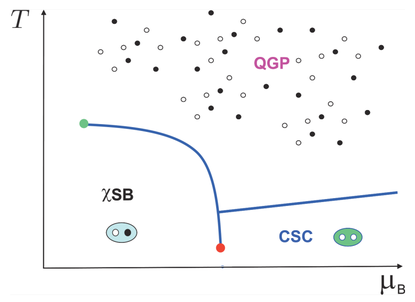

While deconfinement suggests perturbative QCD should work for QGP, the coupling remains strong at experimentally accessible energies (decreasing only as 1/logE), requiring non-perturbative approaches like AdS/CFT to study QGP properties.

At high temperature, the quarks and gluons are deconfined by the Debye screening, this is the quark-gluon plasma phase [2].

HYDRODYNAMIC ANALYSIS

$$ds^2_{\text{SAdS}_5} = \left(\frac{r_0}{L}\right)^2 \frac{1}{u^2}(-h dt^2 + dx_3^2) + L^2 \frac{du^2}{h u^2}\,, \qquad h = 1 - u^4$$

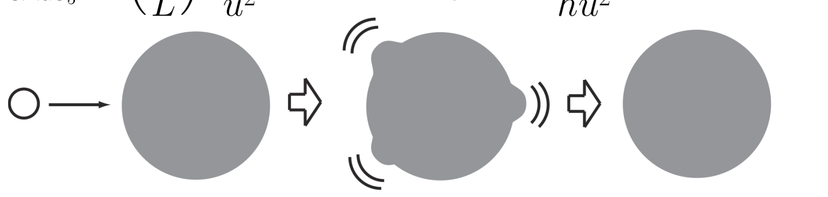

At finite temperature, $SAdS_5$ black holes map to N=4 SYM plasma via gauge/gravity duality. This framework allows computation of various transport coefficients, like viscosity, by analysing how different bulk perturbations propagate in the AdS spacetime. Most notably, AdS/CFT predicts a universal lower bound for the shear viscosity to entropy density ratio $\eta/s = 1/4\pi$ [2].

COMPARISON WITH EXPERIMENTS

The elliptic flow v_2, observed in off-central heavy-ion collisions, reflects the momentum anisotropy of the QGP. Its magnitude depends on the plasma's viscosity.

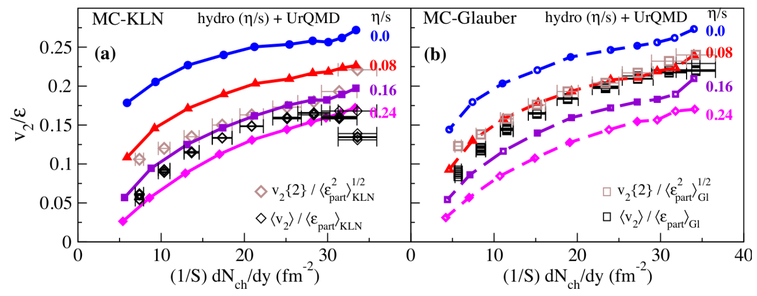

The horizontal axis represents the initial particle density per transverse area and is related to the system's energy density.

The plots show RHIC data vs hydrodynamic simulations with KLN and Glauber initial conditions for different values of η/s. RHIC data constrain QGP viscosity to the holographic bound [4].

$$\frac{1}{4\pi} < \frac{\eta}{s} < 2.5 \times \frac{1}{4\pi}\,, \qquad (T_c < T \lesssim 2T_c)$$

OPEN QUESTIONS

The AdS/CFT correspondence has profoundly reshaped our understanding of quantum gravity, strongly coupled systems, and holography. Yet, fundamental questions remain unresolved.

- **How** spacetime geometry emerges from the entanglement structure of the boundary CFT?
- **What** distinguishes "holographic" CFTs from those without gravitational duals?
- **How** can holography be extended into flat or de Sitter spacetimes?

REFERENCES

[1] J. M. Maldacena, "The Large N limit of superconformal field theories and supergravity", *Adv. Theor. Math. Phys.*, 1998.
[2] M. Natsuume, "AdS/CFT Duality User Guide", 2016.
[3] S. Ryu and T. Takayanagi, "Holographic Derivation of Entanglement Entropy from the anti–de Sitter Space Conformal Field Theory Correspondence", *Physical Review Letters*, 2006.
[4] H. Song et al., "200 A GeV Au + Au Collisions Serve a Nearly Perfect Quark-Gluon Liquid", *Phys. Rev. Lett.*, 2011

2024-2025 YARIYILI FİZİK BÖLÜMÜ

HYPERNUCLEUS IN NUCLEAR PHYSICS

Selin ULUDOĞAN 19022605

Supervisor: Prof. Dr. Kutsal BOZKURT

ABSTRACT

This study investigates hypernuclei, nuclear systems in which one or more hyperons (Λ, Σ, Ξ) are bound to ordinary nuclei. These systems allow the investigation of baryon-baryon interactions involving strangeness. Due to limited scattering data, hypernuclear structure—especially binding energies and decay spectra—offers indirect insight into hyperon–nucleon (YN) and hyperon–hyperon (YY) interactions. Various theoretical models including meson-exchange theory, chiral effective field theory, and relativistic mean field theory are discussed. This work highlights the multidisciplinary relevance of hypernuclei in nuclear, particle, and astrophysical contexts.

INTRODUCTION

.

Hypernucleus systems that go beyond conventional nuclei—occupy a significant position at the intersection of nuclear and particle physics. A hypernucleus is formed when at least one hyperon (such as Λ, Σ, or Ξ, which are baryons containing a strange quark) is bound to an ordinary nucleus. This configuration serves as a unique laboratory for investigating both the effects of strangeness propagation in nuclear matter and the fundamental nature of the strong interaction [1].

The field of hypernuclear physics emerged in the early 1950s from the analysis of unusual nuclear tracks observed in cosmic ray experiments. In 1953, M. Danysz and J. Pniewski discovered the first hypernucleus by detecting the binding of a Λ hyperon to a nucleus. This discovery revealed that nuclear structure is not limited to nucleons alone, and that heavier baryons can also exist stably within the nuclear environment.

Hypernucleus and the production of strangeness provide an ideal setting for testing key features of QCD [2].

Hypernucleus also offer indirect insights into hyperon-nucleon (YN) and hyperon-hyperon (YY) interactions. The short lifetimes of hyperons and the resulting limitations in direct scattering experiments make it extremely challenging to study these interactions directly. However, the observation of a hyperon stably bound within a nucleus provides valuable information about the nature of these interactions. Therefore, measurements of hypernuclear energy levels, binding energies, and decay products play a critical role in the development and validation of theoretical models.

Today, hypernuclear physics contributes not only to our understanding of fundamental particle interactions but also to the study of astrophysical systems—especially in extreme-density environments such as neutron stars, where hyperonic matter is expected to exist. The presence of strangeness in dense matter directly influences various mechanisms and the internal structure of such stars. For this reason, hypernuclear research is of significant importance in astrophysics as well.

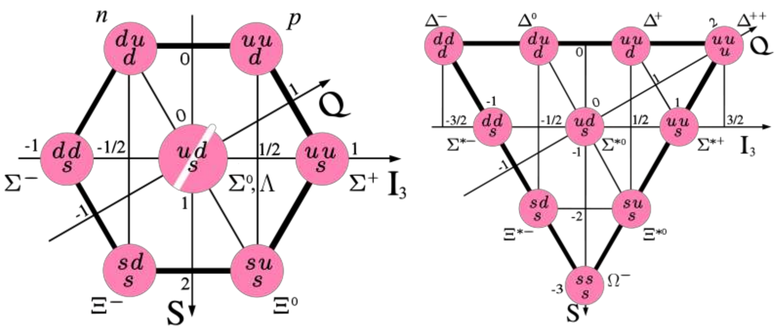

Figure 1 The spin-1/2 baryon and the spin-2/3 baryon decuplet

Λ, Σ, AND Ξ HYPERNUCLEI

Hypernuclei are classified according to the type of hyperon they contain, most commonly Λ, Σ, or Ξ. Each of these hyperons exhibits distinct interaction characteristics with nucleons, shaping the formation, stability, and observability of the corresponding hypernuclear systems.

Λ-hypernuclei

Λ-hypernuclei are the most extensively studied class. The Λ hyperon, being electrically neutral and carrying zero isospin, interacts attractively with nucleons. This interaction is relatively weak and spin-independent, which allows Λ particles to occupy deeply bound states in a wide variety of nuclei. Importantly, the Λ hyperon is not subject to the Pauli exclusion principle within the nucleus, making it an ideal, non-perturbing probe of the nuclear interior. As such, Λ-hypernuclei serve as the primary experimental source for constraining hyperon–nucleon (YN) interaction models.

Σ-hypernuclei

In contrast, Σ-hypernuclei are more elusive. Σ hyperons carry isospin 1 and can have electric charges of +1, 0, or –1. Their interaction with nucleons is highly sensitive to spin and isospin channels, and is often repulsive—particularly for Σ^- in dense nuclear matter. As a result, stable Σ-hypernuclei are rare. Even when they form, Σ hyperons tend to rapidly undergo conversion into Λ via the strong interaction process $\Sigma N \rightarrow \Lambda N$, which further limits their lifetime and detectability as bound systems

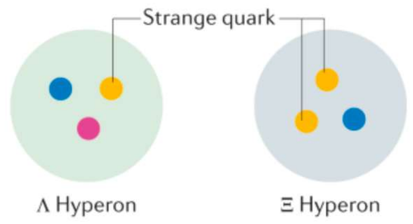

Figure 2 Representation of as Λ and Ξ hyperons with quarks

Ξ-hypernuclei

Ξ-hypernuclei represent a heavier and experimentally less accessible class of strange nuclear systems. The Ξ hyperon contains two strange quarks and interacts attractively with nucleons, although the interaction remains poorly constrained due to the scarcity of direct data. In particular, the negatively charged Ξ^- may be bound in heavy nuclei through a combination of strong and Coulomb forces. One of the most important features of Ξ-hypernuclei is their role in producing double-Λ hypernuclei via the conversion reaction $\Xi^- + p \rightarrow \Lambda + \Lambda$. This process enables access to the S = –2 sector and provides rare observational input for hyperon–hyperon (YY) interactions.

Hyperon and Quark Content	cτ [cm]	Mean lifetime [s]	Mass [GeV/c^2]	Main decay and branching fraction
Λ (uds)	7.89	$(2.632 \pm 0.020) \cdot 10^{-10}$	1.116	$p\pi^-$ (63.9 ± 0.5)% $n\pi^0$ (35.8 ± 0.5%)
Σ^+ (uus)	2.404	$(8.018 \pm 0.026) \cdot 10^{-11}$	1.189	$p\pi^0$ (51.57 ± 0.30)% $n\pi^+$ (48.31 ± 0.30%)
Σ^0 (uds)	$2.22 \cdot 10^{-9}$	$(7.4 \pm 0.7) \cdot 10^{-20}$	1.193	Λγ (100)%
Σ^- (dds)	4.434	$(1.479 \pm 0.011) \cdot 10^{-10}$	1.197	$n\pi^-$ (99.848 ± 0.005)%
Ξ^0 (uss)	8.71	$(2.90 \pm 0.09) \cdot 10^{-10}$	1.315	$\Lambda\pi^0$ (99.524 ± 0.012)%
Ξ^- (dss)	4.91	$(1.639 \pm 0.015) \cdot 10^{-10}$	1.322	$\Lambda\pi^-$ (99.887 ± 0.035)%
Ω^- (sss)	2.461	$(8.21 \pm 0.11) \cdot 10^{-11}$	1.672	ΛK^- (67.8 ± 0.7)% $\Xi^0\pi^-$ (23.6 ± 0.7)% $\Xi^-\pi^0$ (8.6 ± 0.4)%

Table 1 Mean decay length, mean lifetime and mass for the strange ground statehyperons. The most common decay modes are cited together with the branching ratio. [2]

BARYON-BARYON INTERACTIONS

Baryon–baryon interactions are fundamental for understanding both ordinary nuclei (via NN interactions) and hypernuclei (via YN and YY interactions). While the nucleon–nucleon (NN) interaction is well-constrained through decades of scattering data, the situation is very different for systems involving hyperons.

YN interactions: Only ~37 data points exist, mostly from old bubble chamber experiments.

YY interactions: No experimental data are available.[3]

Because hyperons are short-lived, they cannot form intense or stable beams for standard scattering experiments. As a result, hypernuclear structure becomes the primary indirect probe for investigating these interactions.

Properties such as binding energies, spin states, and level splittings in light hypernuclei are used to constrain effective baryon–baryon potentials involving strangeness. This justifies the need for theoretical modeling.

THEORETICAL FRAMEWORK: YN/YY INTERACTION MODELS

Due to the short lifetimes of hyperons, direct scattering experiments for hyperon–nucleon (YN) and hyperon–hyperon (YY) interactions are extremely limited. Therefore, several theoretical models are used to construct effective interaction potentials based on symmetry principles and meson exchange mechanism.The main models are given below:

Nijmegen models (NSC89, NSC97, ESC04/08): Based on one-boson exchange and SU(3) flavor symmetry, including its explicit breaking.

Bonn–Jülich models: Include multi-meson exchange and emphasize short-range interactions.

Chiral Effective Field Theory (EFT): Low-energy expansion based on QCD symmetries, using Goldstone bosons (π, K, η). Calculations include LO and NLO levels.

These models aim to describe quantities such as scattering lengths, spin dependence, and binding energies. Due to the absence of YY scattering data, predictions for double-strangeness systems remain purely theoretical.

STRUCTURE MODELING: HYPERNUCLEAR APPLICATIONS

Once interaction potentials are constructed, they are applied to study the internal structure of hypernuclei. These modeling approaches aim to describe how a hyperon behaves within a nuclear medium and how it modifies the energy levels of the nucleus.

Shell Model: Λ is placed into quantized nuclear orbits, leading to observable single-particle energy levels. This model helps identify new symmetries in Λ–nucleus systems.

Relativistic Mean Field (RMF) Theory: Treats baryons as Dirac spinors interacting with meson fields (σ, ω, ρ). RMF successfully reproduces binding energies and spin-orbit splittings.

SU(3)–SU(6) Symmetry Extensions: The Sakata model combines proton, neutron, and Λ into SU(3) flavor multiplets. When merged with spin SU(2), this yields an extended SU(6) symmetry for light hypernuclei.

These models are calibrated using hypernuclear observables such as level spacings and Λ binding energies. They also allow investigation of three-body ΛNN forces, which play a significant role in few-body systems.

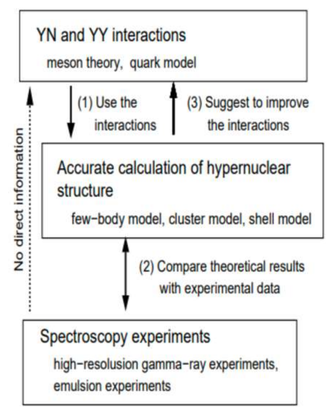

Figure 3 Approach for obtaining insights into YN and YY interactions through the examination of light hypernuclear structure

CONCLUSION

Hypernuclei—nuclear systems containing one or more hyperons—provide a rare and essential opportunity to explore the dynamics of baryon–baryon interactions involving strange quarks. These systems extend nuclear structure beyond nucleons and allow the study of Quantum Chromodynamics (QCD) in environments where confinement, symmetry breaking, and many-body effects intersect.

A major theoretical challenge in this field is the lack of reliable experimental data for hyperon–nucleon (YN) and especially hyperon–hyperon (YY) interactions. Due to the short lifetimes and neutral nature of hyperons, direct scattering experiments are severely limited or altogether infeasible. As a result, the few available YN data points (~37) are insufficient to determine even basic quantities like scattering lengths with high confidence.

To overcome this, hypernuclear observables—such as binding energies, spin–parity levels, and decay spectra—are used as indirect probes. These allow for the construction and refinement of effective interaction models, including:

Meson-exchange models (Nijmegen, Jülich),

Chiral Effective Field Theory, based on low-energy QCD,

Quark-based approaches using SU(3)/SU(6) symmetries.

However, the interpretation of these models is often highly dependent on theoretical assumptions, especially in the absence of empirical constraints. This makes model-dependence a central problem in hypernuclear theory.

To mitigate this, interaction models are embedded within nuclear structure frameworks such as the shell model and relativistic mean field (RMF) theory. These tools allow hypernuclear properties to be calculated and compared with experimental data from reactions like (K^-, π^-), (π^+, K^+), and electroproduction. In light hypernuclei, few-body models are employed to study three-body forces like ΛNN, which are not captured by two-body potentials alone.

Beyond nuclear structure, hypernuclear physics has far-reaching implications for astrophysics. In the high-density cores of neutron stars, the presence of strange baryons alters the equation of state, influencing stellar stability and maximum mass. Hypernuclear research thus plays a vital role in bridging microscopic strong interactions with macroscopic cosmic phenomena.

In conclusion, the study of hypernuclei offers both a solution to the challenge of inaccessible YN/YY data and a path forward in our understanding of the strong force, nuclear matter, and the role of strangeness in the universe.

KAYNAKÇA

[1] A. Gal, E. V. Hungerford, and D. J. Millener, "Strangeness in nuclear physics," *arXiv preprint*, arXiv:1605.00557v2, 2016. [Online]. Available: https://arxiv.org/abs/1605.00557

[2] J. Regina, Time for Hyperons, M.Sc. thesis, Lund University, 2014

[3] H. Bando, “Essence of hypernuclear physics,” Tokyo Univ., Tech. Rep., 1982.

YTÜ FEN EDEBİYAT FAKÜLTESİ

2024-2025 SPRING SEMESTER

PHYSİCS DEPARTMENT

CANCER TREATMENT WITH MUONS

Miraç Ezgi ÖZDEMİR 20022604
Prof Dr.Kutsal BOZKURT

ABSTRACT

Muon-based cancer therapy presents a novel approach for treating deep-seated and radio-resistant tumors by utilizing the unique physical properties of muons, such as high penetration power and low lateral scattering. This study reviews the current literature, evaluates simulation data using the Geant4 platform, and analyzes the technical potential of the KEK prototype muon therapy system in Japan. Results suggest that muons offer precise dose delivery with minimal secondary radiation, providing a promising alternative to conventional hadron therapies for challenging tumor cases.

STANDART MODEL OF ELEMANTARY PARTICLES

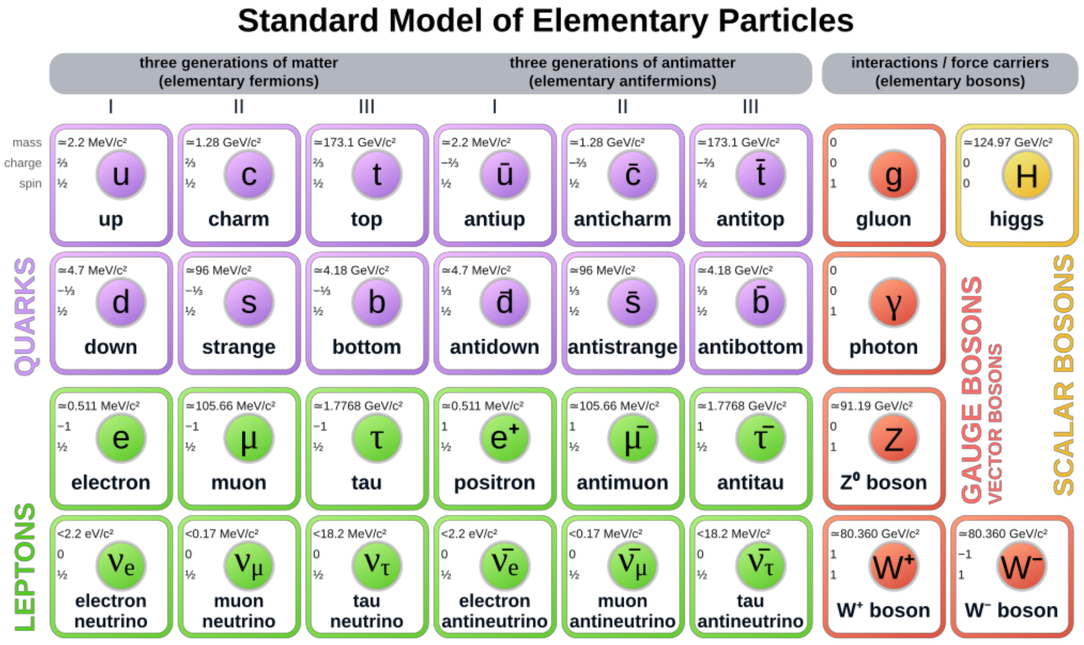

Fig1. Standart model of elemantary particles

The Standard Model explains the fundamental particles of the universe and their interactions. The muon, a second-generation lepton in this model, is the focus of this study.

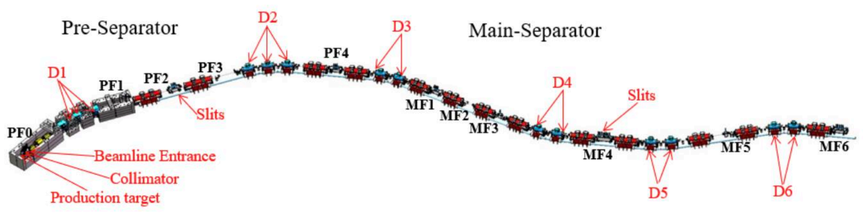

Fig2. KEK Muon Beamline

This diagram shows the KEK muon beamline where muons are produced and directed. At the “production target,” high-energy protons collide and generate muons. “Collimators” straighten the direction of particles, while “magnetic separators” remove unwanted particles, allowing only muons to pass through. “Slits” are narrow openings that control the shape and width of the beam.

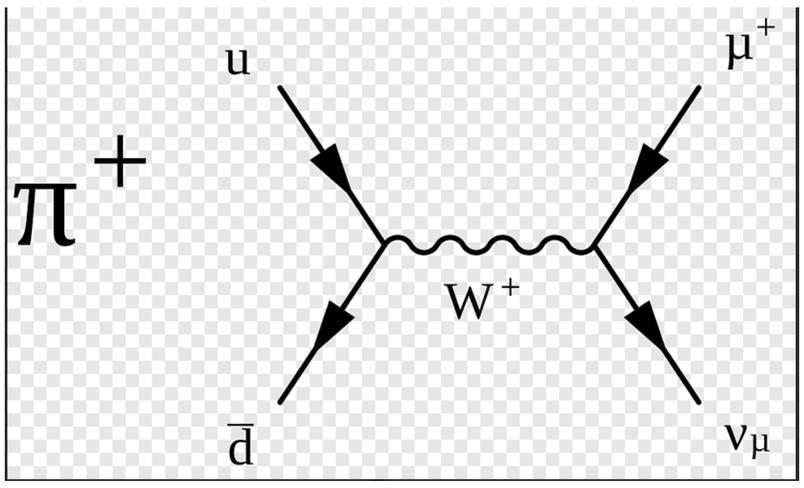

Fig3. The weak interaction decay of a pion into a muon and a muon neutrino. This process is the basis of laboratory muon production.

This diagram shows the weak interaction decay of a pion into a muon and a muon neutrino. This process is the fundamental mechanism for generating high-intensity muon beams in laboratory settings.

This system measures how muons scatter as they pass through matter, providing insight into tissue density and structure. In this thesis, such imaging platforms were evaluated for their potential use in tumor detection and dose distribution analysis.

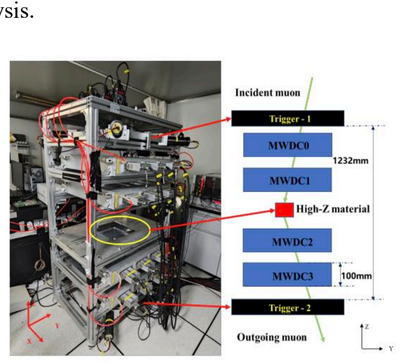

Fig. 1. Multi-Wire Drift Chamber Muon Imaging Platform and 2D Plane Schematic Diagram(YZ_palne)

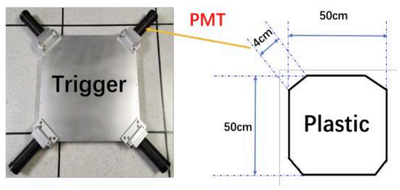

Fig. 2. Large-area plastic scintillator trigger detector. (Left): Physical photograph; (Right): Diagram of shape parameters.

Fig4. Muon Imaging and Triggering System

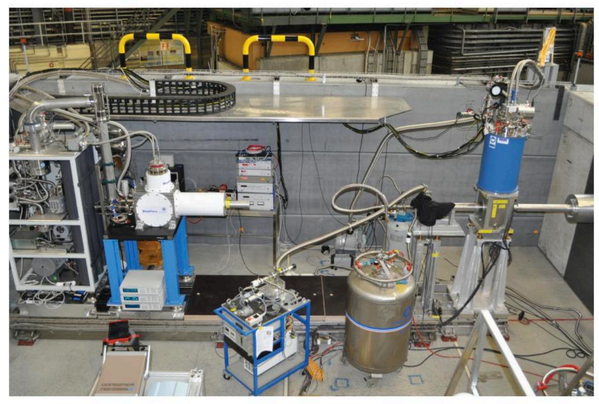

Fig5.Muon Computed Tomography

This experimental setup integrates muon beamlines with precise trigger systems, enabling the validation of Geant4-based simulations under conditions comparable to the KEK prototype facility.

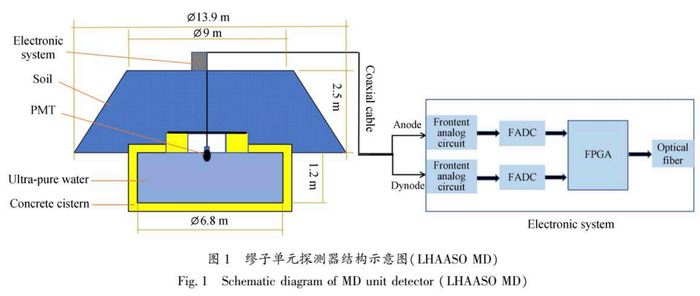

图 1 缪子单元探测器结构示意图(LHAASO MD)

Fig. 1 Schematic diagram of MD unit detector (LHAASO MD)

Fig6. Structure of LHAASO Muon Detector (MD) Unit

This detector system enables high-precision muon measurements by minimizing environmental noise. In this thesis, it is considered as a reference model for accurately detecting and analyzing signals generated as muons pass through deep tissues.

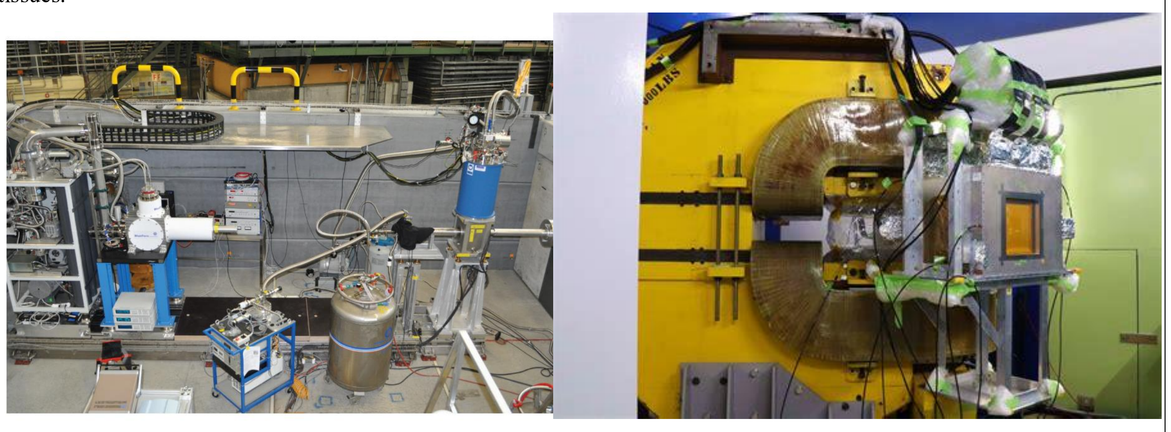

Fig7. Muon Detector Module Under Strong Magnetic Field , Fig8. Particle Accelerator Beamline and Collimation System

These two visuals represent synthetic experimental setups used for the production and guidance of muon beams. The first image shows a detector module operating under a strong magnetic field, designed to separate and steer particles based on their momenta—an essential component in prototype muon therapy systems such as those developed at the KEK Research Center. The second image illustrates a beamline setup at a particle accelerator facility, where muons are focused and delivered to the target through collimators. Both systems serve as physical counterparts to the Geant4-based simulations discussed in this thesis.

REFERENCES

[1] T. Sato et al., "Prototype Design of Muon Radiotherapy Beamline at KEK," ChinaXiv:202503.00082V1 (2025).
[2] C. Liu et al., "A Portable Muon Imaging System Based on MWDC," ChinaXiv:202306.00596V1.
[3] Y. Zhao et al., "Geant4 Simulation Study of Muon Energy Loss in Biological Tissue," ChinaXiv:202404.00057V1.
[4] T. Sato et al., "Technical Feasibility of a Muon Therapy Beamline at KEK," ChinaXiv:202503.00082V1.

2024-2025 Bahar Yarıyılı FİZİK BÖLÜMÜ

Özel Görelilik ve Zaman Genişlemesi

Gülsu Kılıç 19022049

Danışman: Prof.Dr. Zeynel YALÇIN

ÖZET

Bu çalışmanın temel amacı, Albert Einstein'ın ortaya sunduğu özel görelilik teorisi ve bu teorinin en büyük bulgularından biri olan zaman genleşmesi olayını detaylı bir şekilde ele almaktır. Bu tez, özel göreliliğin ortaya çıkış nedenini, temel postülatlarını ve sonuçlarını, Lorentz dönüşümlerinin detaylandırılarak zaman genleşmesinin nicel ifadesinin ortaya çıkışını, ikizler paradoksunu ve eşzamanlılık kavramını hem teorik hem deneysel olarak açıklamayı amaçlamaktadır.

ÖZEL GÖRELİLİK VE ZAMAN GENİŞLEMESİ

Özel Görelilik Teorisi Nedir ?

Özel görelilik Teorisi, 1905 yılında Albert Einstein 'ın "Hareketli Cisimlerin Elektrodinamiği Üzerine " adlı yazısında öne sürülmüştür. Bu teorinin ana yapısı zaman ve uzay kavramlarına dayanır. Yüzyıllardır fiziğin temeli olarak kabul görmüş mutlak zaman ve uzay, görelilik teorisinin öne sürdüğü gözlemcinin hareketine dayalı zaman ve uzay kavramı ile çürütülmüş ve bu teori ile birlikte bilimde yeni bir çağın kapısı aralanmıştır.

Ortaya Çıkma Nedenleri

- Newton mekaniğinin, Maxwell teorisinde öne sürülmüş olan ışığın dalgalar halinde ve sabit hızla yayılma varsayımı ile çelişki göstermesi.
- Michelson-Morley deneyi ile birlikte ışığın yayıldığı ortam olarak varsayılan eter kavramının çökertilmesi : ışık hızının her yönde aynı olması
- Galilei dönüşümlerinin (hızları toplama kuralı) ışık hızı sabitliliğini açıklamaktaki yetersizliği

Einstein Postülatları

- Görelilik ilkesi: Fizik yasaları (elektromanyetizma da dahil) tüm eylemsiz sistemler için aynı şekilde gerçekleşir.
- Işık hızının sabitliği: Işık hızı tüm gözlemciler için aynıdır.

Özel Göreliliğin Sonuçları

- **Zaman Genişlemesi:** Hareket eden saatler, durağan saatlere göre daha yavaş çalışır.
- **Uzunluk Kısalması:** Hareket eden cismin boyunda kısalma meydana gelir. ($L = \frac{L_0}{\gamma}$)
- **Eşzamanlılığın Göreliliği:** Bir referans sisteminde aynı anda olan olaylar, farklı referans sistemleri için farklı zamanlarda olabilir.
- **Kütle-Enerji Eşdeğerliği ($E=mc^2$):** Kütle ve enerji birbiri ile ilşkilidir. Kütle, enerjiye dönüşebilir.

Zaman Genişlemesi Nedir?

Hareketli sistemlerde zaman daha yavaş akar. Hareketli saatler,durağan saatlere göre daha yavaş çalışır. Zaman genişlemesi, matematiksel olarak Lorentz dönüşümlerinden türetilen Lorentz faktörü ile ifade edilir.

$\gamma = \frac{1}{\sqrt{1-(\frac{v^2}{c^2})}}$ (gama faktörü) $\Delta t' = \Delta t\ \gamma$ (t': hareketli gözlemci için geçen zaman, t : durağan zaman)

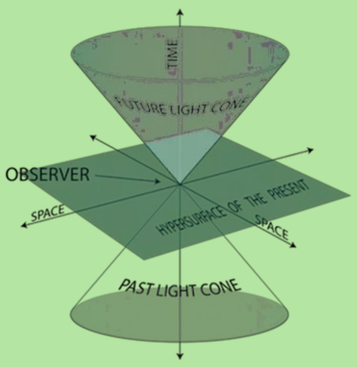

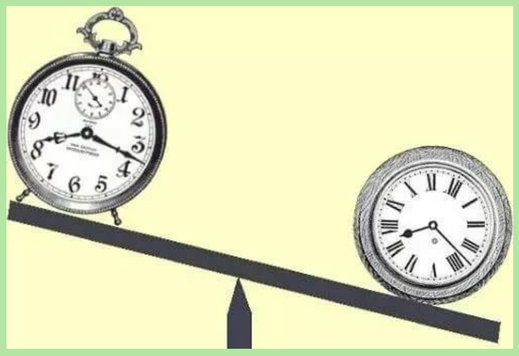

İkizler Paradoksu

Jenny ve Johnny ikiz kardeşlerdir. Uzayda yolculuğa çıkan astronot ikiz Jenny, yolculuğu bitip Dünya'ya geri döndüğünde, Dünya'da kalan ikize Johnny'e göre daha genç olacaktır. Bunun sebeni ise hareketli sistemde zamanın, durgun sisteme göre daha yavaş akmasından kaynaklanmaktadır.

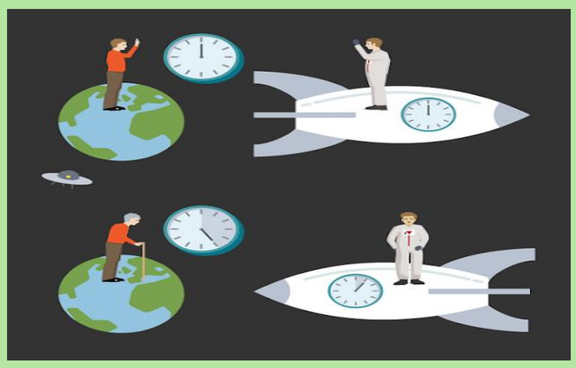

ZAMAN GENİŞLEMESİ UYGULAMALARI ve DENEYSEL KANITLAR

Hafele-Keating Deneyi (1971):
Atom saatleri jet uçaklarına ve Dünya yüzeyine yerleştirildi.
Hareketli saatler, yerdeki saatlere göre **nanosaniyeler** seviyesinde yavaş çalıştı (öngörülenle uyumlu)

Müon Deneyleri:
Rossi –Hall Deneyi : İlk muon deneyi olarak bilinir. Atmosferde oluşan müonlar, ömürleri dolayısıyla Newton mekaniğine göre yeryüzüne ulaşmadan bozunmalıydı.
Ancak **yüksek hızları** nedeniyle zaman genişlemesi sayesinde yere ulaştıkları doğrulandı.

Parçacık Hızlandırıcı Verileri:
CERN'deki protonlar ışık hızının %99.99'una ulaştığında, bozunma süreleri binlerce kat uzar.
Yüksek hızlı parçacıklar (ışık hızına yakın) normalden çok daha uzun süre bozunmadan kalır.Örneğin, müonlar yerdeki gözlemcilere göre daha uzun ömürlüdür.

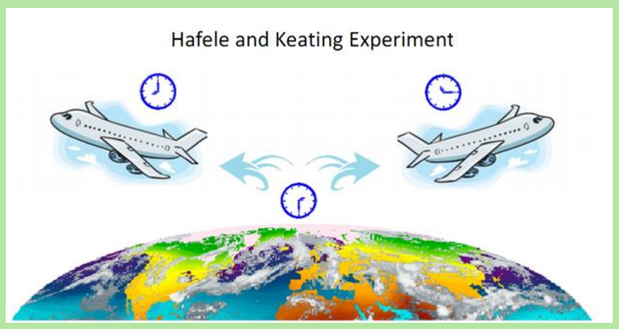

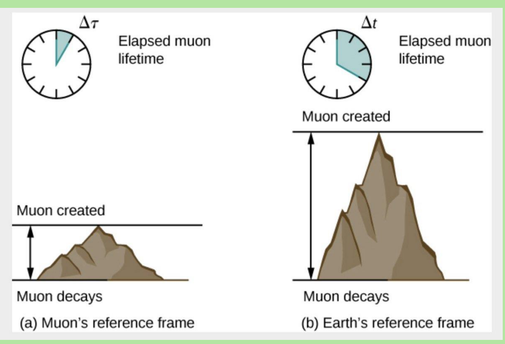

SONUÇ

Özel görelilik teorisi, zamanın mutlak olmadığını ve gözlemcinin hareketine bağlı olduğunu kanıtlamıştır. Zaman genişlemesi, teorik ve deneysel olarak desteklenmekte ve modern teknolojide kritik bir rol oynamaktadır. Bu çalışma, özel göreliliğin temel kavramlarını ve uygulamalarını bir araya getirerek konuya bütüncül bir bakış sunmaktadır.

KAYNAKÇA

[1] Einstein, A. (1989). İzafiyet teorisi: Özel ve genel görelilik. (Orijinal çalışma 1916'da yayımlandı).
[2] Einstein, A. (2005). Özel görelilik. Bilim ve Teknik, 447
[3] Albayrak, H. (2020). Hareket ve Newton Fiziği Üzerine Notlar.

2024-2025 Bahar Yarıyılı FİZİK BÖLÜMÜ

Yeni Nesil Radyasyon Zırhlayıcılar

Eylül Yağmur Topal 20022074

Danışman: Dr. Öğr. Üyesi Yaşar KARABUL

ÖZET

Günümüzde nükleer teknolojilerin ve radyasyon uygulamalarının yaygınlaşmasıyla birlikte, iyonlaştırıcı radyasyona karşı hafif, çevre dostu ve yüksek performanslı zırhlama malzemelerine olan talep giderek artmaktadır. Geleneksel olarak kullanılan kurşun bazlı koruyucular, ağırlıkları, toksik etkileri ve işlenme zorlukları nedeniyle yerini alternatif malzemelere bırakmaktadır. Bu çalışmada yeni nesil radyasyon zırhlama malzemeleri incelenmiştir. Elde edilen sonuçlar, yeni nesil radyasyon zırhlama kompozitlerinin, geleneksel çözümlere kıyasla daha hafif, çevre dostu ve yüksek koruma sağlayan bir seçenek sunduğunu ortaya koymaktadır.

YENİ NESİL RADYASYON ZIRHLAYICLAR

Radyasyon Nedir?

Radyasyon, enerjinin dalgalar veya parçacıklar halinde yayılması olarak tanımlanabilir. Modern fizikte elektromanyetik radyasyon ve parçacık radyasyonu olarak iki ana gruba ayrılır. Radyasyonun doğal ve yapay kaynakları bulunur ve tıptan enerji üretimine kadar birçok alanda kullanılmaktadır. Bununla birlikte, kontrolsüz maruziyet canlılar için ciddi riskler oluşturabilir.

Günlük yaşamda kullanılan mikrodalgalar, radyo dalgaları ve X-ışınları gibi çeşitli radyasyon türleri; pişirme, iletişim ve tıbbi incelemeler gibi alanlarda yaygın olarak kullanılmaktadır. Radyasyon, aynı zamanda radyoaktif maddelerden de kaynaklanır. Bu maddeler doğada kendiliğinden bulunabildiği gibi, yapay olarak da üretilebilir. Radyasyonları, maddelerde oluşturdukları etkilere göre iki ana kategoriye ayırmak mümkündür: İyonlaştırıcı ve iyonlaştırıcı olmayan radyasyonlar. Ayrıca, radyasyon kaynağına bağlı olarak doğal ve yapay radyasyon olarak da sınıflandırılabilir.

Geleneksel Zırhlama Yöntemleri

1. Temel Zırhlama Prensibi

Radyasyon zırhlama, radyasyonun madde ile etkileşerek enerjisini kaybetmesini sağlar. Amaç:

- Emilim (absorpsiyon)
- Saçılma (scattering)
- Zayıflatma (attenuation)

Bu prensiplere göre yoğunluğu yüksek, atom numarası büyük malzemeler tercih edilir.

2. Kurşun (Pb) – En Yaygın Geleneksel Malzeme

Avantajları:

- Yüksek atom numarasına sahiptir (Z=82) ve yüksek yoğunluktadır (11.34 g/cm^3)
- Gama ve X-ışınlarına karşı çok etkilidir.
- Kolay şekil verilebilir, ince levha olarak kullanılabilir.

Dezavantajları:

- Toksik ve çevreye zararlıdır
- Ağırdır, taşınabilirlik zayıftır
- Mekanik dayanımı düşüktür
- Radyasyon geçirgenliği, yüksek enerjili parçacıklar için yetersiz kalabilir

Kullanım Alanları: Röntgen odaları, laboratuvarlar, radyoterapi merkezleri, nükleer santraller

3. Beton

Avantajları:

- Ucuzdur ve yaygın bulunabilir.
- Kalın dökümlerle iyi zayıflatma sağlar.
- Geniş alanlarda (nükleer santral, radyasyon sığınakları) kullanılabilir.

Dezavantajları:

- Kalınlık gerektirir bu da yer ve ağırlık sorununa yol açar.
- Gama ve nötronlar için tek başına yetersiz olabilir.
- Mikroyapısı gözenekli olduğu için zamanla zayıflayabilir.

Ağır betonlara barit, hematit veya manyetit gibi mineraller eklenerek zayıflatma kabiliyeti artırılabilir.

4. Çelik (Paslanmaz Çelik, Kurşunlu Çelik)

Özellikle reaktörler ve konteynerler gibi yüksek sıcaklığa ve basınca dayanıklı ortamlarda kullanılır. Kurşuna göre daha dayanıklıdır, ancak maliyeti yüksektir.

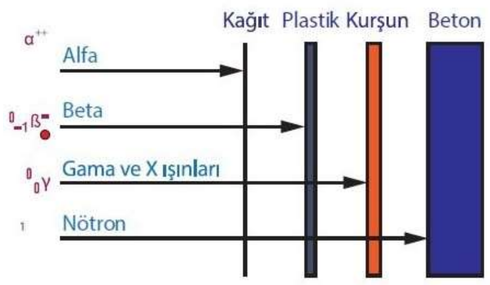

.

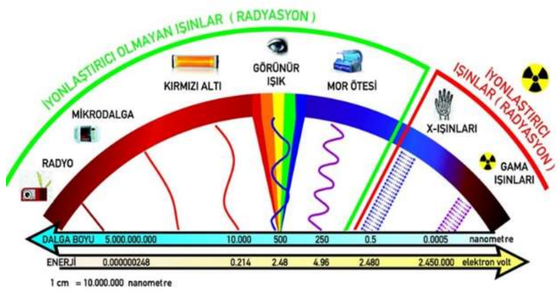

Yeni Nesil Zırhlayıcıların Genel Özellikleri

- Kurşunsuz ya da düşük toksisiteye sahiplerdir.
- Hafif ve mekanik olarak güçlülerdir.
- Gama, nötron, X-ışını gibi farklı radyasyon türlerine karşı etkilidir.
- Çevre dostu ve sürdürülebilirdir.
- Polimer matrislerle şekillendirilebilir ve modüler üretime uygundur.

Yeni Nesil Radyasyon Zırhlarında Kullanılan Malzemeler ve Yapılar

Yeni nesil zırhlarda, radyasyonu doğrudan soğuran katkı maddeleri bir **matris** içinde dağılır. Bu matris; malzemeye şekil verilebilirlik, esneklik ve hafiflik kazandırır. Aynı zamanda katkı maddelerini homojen dağıtarak koruma verimini arttırır.

Yaygın Matris Türleri:

- **Epoksi Reçineler**: Sertleşince dayanıklı olur, yüksek bağlayıcılık sağlar.
- **Poliüretan**: Esnektir, darbe dayanımı yüksektir.
- **Silikon**: Isı dayanımı iyidir, biyouyumlu ve esnektir.
- **Polivinil Alkol (PVA), Polietilen (PE)** gibi termoplastikler.

Bu matris türleri; hafiflik, üretim kolaylığı, esneklik ve kaplanabilirlik sağlar.

Katkı Maddeleri (Radyasyonu Zayıflatan Asıl Bileşenler)

1. Ağır Metal Oksitler (Gama ve X-Işını İçin)

- **Bizmut Oksit (Bi_2O_3):** Kurşuna yakın derecede bir koruma sağlar ve toksik değildir.
- **Barit ($BaSO_4$):** Ucuzdur ve yaygın kullanılır. Kütlece yoğun bir yapıya sahiptir.
- **Tungsten Oksit (WO_3):** Yoğunluğu ve zayıflatma etkisi yüksektir.
- **Seramik katkılar (ZnO, SnO_2, CuO, TiO_2):** Yardımcı koruma ve mekanik güç artışı sağlar.

2. Bor ve Türevleri (Nötronlar İçin)

- **Borik Asit (H_3BO_3):** Polimer içinde kolay dağılır.
- **Bor oksit (B_2O_3):** Cam yapımında da kullanılır.

3. Doğal ve Destekleyici Yapılar

- **Jüt, Kenevir, Hindistan Cevizi Lifi:** Epoksi içinde hem dayanım hem sürdürülebilirlik sağlar.
- **Selüloz Nanoeliyafları:** Hafif ama sağlam yapılar için kullanılır.
- **Perlit, Manyetit, Bentonit:** İzolasyon, mekanik güç ve radyasyon tutuculuk sağlar.

4. Kompozit ve Çok Katmanlı Yapılar

Yeni nesil zırh sistemleri genellikle çok katmanlı veya hibrit olarak tasarlanır.

- **İç katman**: Nötron soğurucu (bor katkılı polimer)
- **Orta katman**: Gama zayıflatıcı (Bi_2O_3, $BaSO_4$ vb.)
- **Dış katman**: Mekanik koruma (sert polimer, çelik örgü vb.)

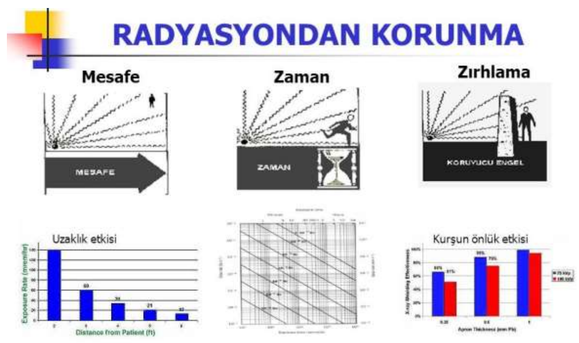

SONUÇ

Yeni nesil radyasyon zırhlayıcı malzemeler, geleneksel kurşunlu sistemlerin toksisite, ağırlık ve esneklik gibi sınırlamalarını aşarak daha güvenli, hafif ve çevre dostu çözümler sunmaktadır. Bi_2O_3, barit, bor bileşikleri gibi katkılarla zenginleştirilen polimer matrisli kompozitler, tıp, nükleer enerji, savunma ve uzay gibi birçok kritik alanda etkili koruma sağlamaktadır.

Bu malzemelerin çok yönlü yapısı sayesinde; Farklı radyasyon türlerine karşı eşzamanlı koruma sağlanabilir ve taşınabilir, modüler ve şekillendirilebilir zırh sistemleri geliştirilebilir. Yeni nesil radyasyon zırhlamada kurşunsuz, sürdürülebilir ve biyo-uyumlu tasarımlar ön plana çıkmaktadır.

KAYNAKÇA

[1] Li, R., Gu, Y., Wang, Y., & Chen, L. (2022). "Graphene-based nanocomposites for radiation shielding: A review". Materials Today Physics,28,100865,

[2] Yaşar, K. (2021). Yeni nesil radyasyon zırhlayıcılar: epoksi temelli metal oksit mikro ve nano yapılı kompozitler

[3] Aslı, A. (2018). Radyasyon zırhlama için yeni, hafif, kompozit malzemeler

YTÜ FEN EDEBİYAT FAKÜLTESİ

2024-2025 SPRING SEMESTER PHYSICS

DEPARTMENT

APPLICATIONS IN SENSOR TECHNOLOGY

ELIF NAZ YIGIT- 19022076

Supervisor : Prof. Dr. Tuncer Kaya

ABSTRACT

This research articulates the physical principles underlying sensor technologies and highlights how material-level modifications particularly via ZnO doping can drive innovation in sensor functionality, precision, and adaptability. The conclusions are substantiated through a synthesis of theoretical insights and extensive empirical data, emphasizing the interdependence of fundamental physics and applied material science in the evolution of advanced sensing systems

The Foundational Role and Operational Principles of Sensors

In the age of automation, intelligent systems, and real-time data environments, sensors constitute the essential link between the physical world and digital infrastructures. Functioning as transducers, sensors detect a wide range of physical, chemical, or biological phenomena and convert them into electrical signals that can be measured, processed, and interpreted by computational systems. This transformation is structured into three fundamental stages: (1) **physical interaction and energy conversion**, (2) **signal transduction and conditioning**, and (3) **output and data transmission**. Each stage is underpinned by specific physical mechanisms such as the **Seebeck effect** in thermal sensors, the **photoelectric effect** in optical sensors, **piezoelectricity** in mechanical sensors, and **capacitive or Hall effects** in electronic sensors. The diversity of sensor types thermal, optical, mechanical, magnetic, chemical, and capacitive is rooted in classical physics, thermodynamics, quantum mechanics, and solid-state principles. For instance, thermal sensors exploit temperature-dependent electrical resistance, while chemical sensors utilize redox reactions and surface adsorption processes to detect gaseous or liquid analytes. Magnetic sensors employ the Hall effect to detect field variations, and capacitive sensors detect changes in permittivity due to physical displacement or dielectric variation.

Modern sensors go beyond mere measurement tools; they are embedded within both open-loop and closed-loop systems, actively contributing to automation, fault detection, and adaptive feedback mechanisms. They are central to the operation of cyber-physical systems, IoT frameworks, autonomous machines, and wearable health technologies. Recent advancements in nanotechnology, MEMS/NEMS integration, and materials science have significantly improved sensor performance in terms of **miniaturization, sensitivity, selectivity, and response speed**.

In this context, the physical principles behind sensors are not abstract scientific constructs but practical engineering tools that enable the continuous and accurate monitoring of complex environments. As societal reliance on data-driven solutions increases, the development of high-performance sensors becomes increasingly dependent on the **material properties and engineering innovations** integrated into their structure a field in which **ZnO** has shown remarkable promise. [1]

Table 1: Sensor Applications of Underlying Physics

Sensor Type	Underlying Physics	Typical Application
Thermal	Seebeck effect, resistance-temperature relationship (RTD, thermistor)	Temperature sensing
Optical	Photoelectric effect, light absorption, interference	Automotive Technologies, optical communication [4]
Mechanical	Hooke's law, piezoelectric effect [6], strain-resistance correlation	Industrial Automation and Robotics
Magnetic	Lorentz force, Hall effect, flux density variation	Proximity detection, current sensing
Chemical	Redox reactions, conductivity change, adsorption	Gas sensing, PH measurement [3]
Capacitive	Permittivity-based capacitance variation	Touch sensing, pressure detection

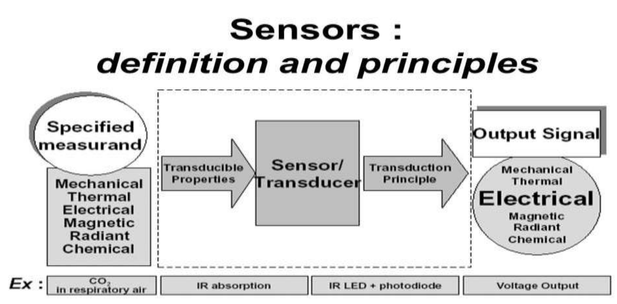

Figure 1: Working princible of sensor

Zinc Oxide (ZnO) as and Advanced Sensing Applications:

Zinc oxide (ZnO) stands out among functional materials for sensing technologies due to its versatile physical, chemical, and structural characteristics. As a wide-bandgap (~3.37 eV), intrinsically n-type semiconductor with high exciton binding energy (~60 meV) and a non-centrosymmetric wurtzite structure, ZnO supports diverse sensing platforms, including chemiresistive gas sensors, UV photodetectors, piezoelectric pressure sensors, and biosensors.

Its piezoelectric and pyroelectric properties enable self-powered sensor designs, while oxygen vacancies and zinc interstitials on the surface serve as active sites for gas adsorption. Reducing gases (e.g., CO, H_2) interact with adsorbed oxygen species, altering electrical resistance via electron transfer, which underpins ZnO's gas-sensing mechanism. Doping ZnO with elements like Al, Ga, Cu, Pt, or Pd further enhances sensitivity, selectivity, and stability by tuning conductivity, surface energy, and catalytic activity. For instance, Pd enhances ethanol detection, Pt enables low-temperature hydrogen sensing, and Sn improves NO_2 response.

Nanostructuring into rods, wires, or hierarchical forms boosts surface-to-volume ratio, optimizing analyte interaction crucial for environmental and biomedical applications. However, excessive doping may induce lattice distortion and reduce performance, highlighting the need for precise synthesis control to ensure reproducibility.[2]

Table 2: Application of specific doping strategies in ZnO-based sensors: Dopant roles, Band gap modulation and Sensing mechanisms

Sensor type	Dopant used	Why this dopant?	Application domain	Operating band gap (Ev)	Sensor mechanism
Ethanol gas sensor [4]	Pd	Pd catalyzes ethanol oxidation	Industrial Safety	3.25	Chemiresistive
Hydrogen gas sensor [5]	Pt	Pt lowers the activation barrier for H2. Dissociation, enabling fast hydrogen sensing.	Clean energy	3.1	Chemiresistive
Ammonia gas sensor [6]	Cr	Cr enhances charge separation and selectivity toward ammonia molecules	Agricultural sensing	3.15	Chemiresistive
PH sensor [7]	Ni	Ni modifies surface redox potential and improves PH response linearity.	Biomedical clinical	3.2	Potentiometric
Pressure sensor [8]	Undoped	Undoped ZnO provides strong piezoelectric output due to wurtzite	Wearable electronics	3.37	Piezoelectric
NO2 gas sensor [9]	Sn	Sn increases oxygen vacancy sites and improves electron withdrawal by NO2	Environmental monitoring	3.1	Chemiresistive
CO gas sensor [10]	Cu	Cu provides catalytic centers and enhances CO sensitivity at lower temperature	Automotive safety	3.2	Chemiresistive

The table illustrates how doping ZnO with noble (Pd, Pt) or transition metals (Cr, Ni, Cu) effectively tunes its surface reactivity, electronic conductivity, and bandgap to suit specific sensing needs. For example, Pd enhances ethanol detection via surface catalysis, while Pt enables low-energy hydrogen dissociation. Cr and Ni improve ammonia and pH sensitivity through modulation of charge separation and redox potential.

These doped systems find applications in industrial safety, environmental monitoring, renewable energy, and biomedical diagnostics. Undoped ZnO, meanwhile, remains effective as a piezoelectric material for pressure sensing, underscoring its intrinsic multifunctionality.

The underlying sensing mechanisms chemiresistive, potentiometric, or photoconductive depend on the dopant and the target analyte [3]

REFERENCES

[1] Fraden, J. (2016). Handbook of Modern Sensors: Physics, Designs, and Applications (5th ed.). Springer.
[2] Janotti, A., & Van de Walle, C. G. (2009). Fundamentals of zinc oxide as a semiconductor. Reports on Progress in Physics, 72(12), 126501.
[3] Huang, J., et al. (2007). Sens. Actuators B, 128(1), 418–423.
[4] Korotcenkov, G. (2008). *Mater. Sci. Eng. R*, 61(1), 1–39.
[5] Comini, E., et al. (2002). *Sens. Actuators B*, 84(2-3), 160–168
[6] Djurisić, A. B., & Leung, Y. H. (2006). *Small*, 2(8-9), 944–961
[7] Macwan, D. P., et al. (2011). *J. Mater. Chem.*, 21(39), 15132–15140.
[8] Wang, Z. L., & Song, J. (2006). *Science*, 312(5771), 242–246
[9] Janotti, A., & Van de Walle, C. G. (2009). Fundamentals of zinc oxide as a semiconductor. *Reports on Progress in Physics*,
[10] Zhang, S. B., Wei, S. H., & Zunger, A. (2001). Intrinsic n-type versus p-type doping asymmetry and the defect physics of ZnO. *Physical Review B*, 63(7

2024-2025 Bahar Yarıyılı FİZİK BÖLÜMÜ

TRANSPARENT SOLAR CELLS

Şeymanur BAŞAR 19022015

Danışman: Doc.Dr. Fatma Pınar CHOI

ÖZET

In the thesis, we explained how we produced transparent solar cells in a laboratory environment. In our work, we focused on the cost-effectiveness, environmental friendliness and wide energy bandwidth of metal oxides.

TRANSPARENT SOLAR CELLS

Photovoltaic Effect and Solar Cell Working Principles

The scene of the first emergence of the solar energy began in 1839, when Bequerel discovered in his experiments that photovoltage was generated from the light on the electrode in an electrolyte solution. Later, Adams and Day made a similar observation in solid-state selenium after Smith's discovery of photoconductivitiy in selenium . Subsequently, the development of photocells based on these materials and copper oxide was explored. R.Ohl discovered the first silicon solar cell in 1940. He shone a torch on it. He was able to measure a large electrical voltage from the silicon rod . However, the first efficient silicon cell was announced in 1954. These cells were originally designed in 1958 and initially started to be used as a power source in spacecraft . Between 1960 and 1970, satellites using solar cells were launched. In the mid-1970s, terrestrial solar cells for applications were started and the main reason was the shortage of oil. In the 1980s, as a result of technological developments, it was determined that the cells were more affordable and thus a new year was opened. In 1914, the effiency of the selenium cell was only 1%. With the developing technology, silicon cell efficiency reached 15 per cent in 1980.Of course, these are terrestrial cell batterials. The copper sulpher cadmium sulphide heterojunction was the first thin film photovoltaic system to attract great interest. This cell was registered in 1954 by Reynolds et al. with an efficiency of %6 . Nowadays, there are quite a lot of studies on thin film solar cells. Cell efficiency has increased and the cost is decreasing. Briefly, Photovoltaics (PV) is the direct conversion of photons into electricity using thin layers of materials known as semiconductors. When the photon reaches the cell surface, photons in the semiconductor structure displace electrons and form electrone-hole pairs. The electric field inside the cell seperates these charge and the electrons move in a certain direction. As a result of this movement, a current flows through the external circuit. Thus, light energy is directly converted into electrical energy. This photovoltaics effect forms the basis of solar cell technology.

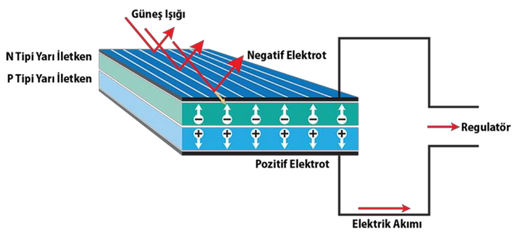

Metal Oxide Used in Transparent Solar Cells

In transparent solar cells, it transmits some of the light due to its structure. For this, conductive and transparent layers are required. Metal oxides meet this requirement.The most widely used indium tin oxide (ITO) layer has high conductivity .It can be used as anode and cathode electrode.The disadvantage is that indium is expensive.Fluorine alloyed tin oxide(FTO), which is more durable than ITO, is cheaper and more transparent.Aluminium alloyed zinc oxide (AZO) is used in large area applications.Titanium dioxide (TiO_2) used as electron carrier layer is used in organic solar cells with perovskite.Nickel Oxide (NiO) is used as a vacancy carrier layer

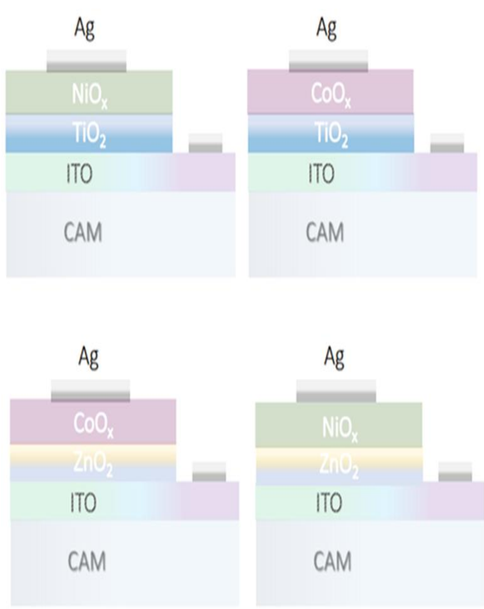

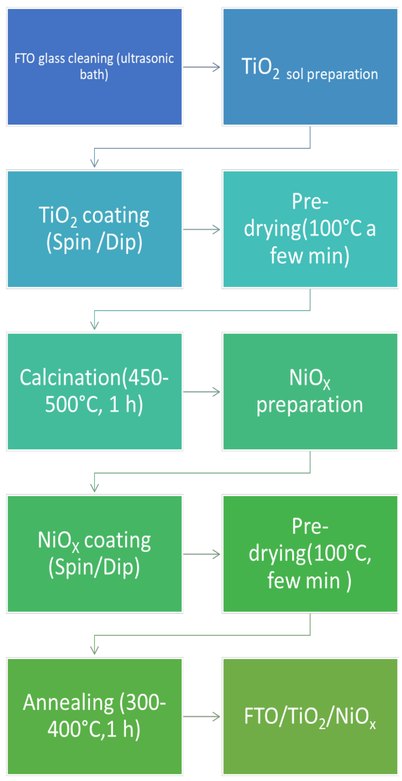

Preparation of titanium dioxide solution

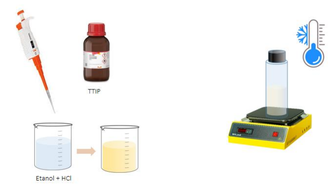

Preparation of titanium oxide films

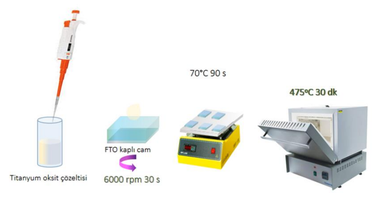

Preparation of nickel oxide solution

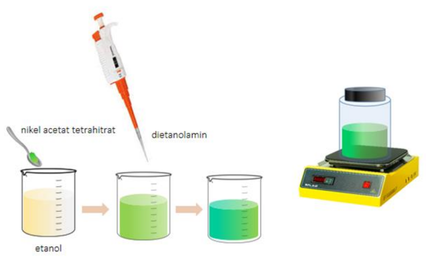

Growth of nickel oxide on TiO_2 films

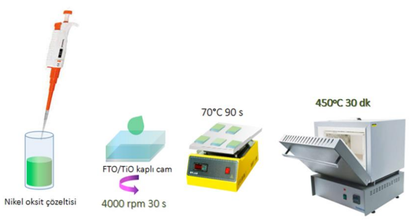

	VOC/mV	JSC/mAcm^-2
ZnO : NiOx	0.0125V	0.0002519947
ZnO : CoOx	0.0125V	0.0008959579
TiO_2 :NiOx	0.0125	0.0001128205
TiO_2 : CoOx	0.0125	0.0002688180

$$FF = \frac{Pm}{Isc\ x\ Voc}$$

$$\eta = \frac{Pm}{Pin} x100$$

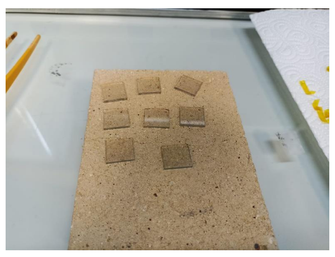

Nature offers its naturel riches. If we succeed in utilizing natural resources with maximum efficiency and minimum environmental pollution, we will leave a livable world for future generation. Due to fact that fossil fuels and non-renewable energy sources used as energy sources create human health and environmental pollution, interest in sustainable energy is increasing worldwide. In addition, the low cost of renewable energy and the fact that it is an environmentally clean source increases efforts in this direction.

The sun is a key energy that is unlimited and when used correctly, we can achieve high yields. Generally, solar energy panels are used for water heating. In fact, with the right investment and sanction, we can reach a position to meet all the energy needs of the house. In recent years, caravan and prefabricated house systems have been developed for this purpose. We aim to install this method in the entire city layout and make solar energy a part of our daily lives.

KAYNAKÇA

[1]https://polen.itu.edu.tr:8443/server/api/core/bitstreams/7e6f88a1-371c-42d8-87f5-c50b48bee8fd/content

[2] https://www.sciencedirect.com/science/article/abs/pii/S092702482030307X

[3] https://webrazzi.com/2021/11/29/seffaf-gunes-panelleri-isigin-gecirgenligini-engellemeden-enerji-elde-etmeyi-mumkun-hale-getiriyor/

2024-2025 Spring Semester Department of Physics

Fundamental Physics of TOKAMAK

Yusuf Tuğrul YİĞİT 18022602

ADVISOR: Orhan ÖZDEMİR

Abstract: This presentation mainly focus on an explanatory overview of how Plasma, charged particles—such as electrons and ions—behave in the presence of electric and magnetic fields. By focusing on single-particle motion, it lays the groundwork for understanding more complex plasma behavior described by fluid and kinetic theories.

Overview of Plasma Under Magnetic Field and Confinement

Field-Particle Coupling, Gyromotion:

When a charged particle (like an electron or an ion) enters a magnetic field, it experiences the **Lorentz force**. This force is always perpendicular to both the particle's velocity and the magnetic field direction. As a result, the magnetic force does no work on the particle (because work is done only by a force component parallel to displacement), meaning it doesn't change the particle's kinetic energy. Instead, it continuously deflects the particle's path, causing it to move in a circular or helical trajectory.
This circular motion perpendicular to the magnetic field is called **gyromotion** or **cyclotron motion**.

Lorentz Force:

$$m\frac{d\vec{v}}{dt} = q(\vec{E} + \vec{v} \times \vec{B})$$

Respect to time and substitute the second equation and then Rearranging this gives the equation for a simple harmonic oscillator:

$$m\frac{d^2v_x}{dt^2} = qB\frac{dv_y}{dt} = qB\left(-\frac{qB}{m}v_x\right) = -\frac{q^2B^2}{m}v_x \qquad \frac{d^2v_x}{dt^2} + \left(\frac{qB}{m}\right)^2 v_x = 0$$

A similar equation can be derived for y- axis. The solutions describe a circular motion in the plane perpendicular to B. The characteristic angular frequency of this oscillation is the **cyclotron frequency** (or **gyrofrequency**) Also The radius of this circular orbit, known as the **Larmor radius**, is found by balancing the magnetic force with the centrifugal force:

$$\omega_c = \frac{|q|B}{m} \qquad r_L = \frac{v_\perp}{\omega_c} = \frac{mv_\perp}{|q|B}$$

This equations determines the movement of shape of the plasma under magnetism.

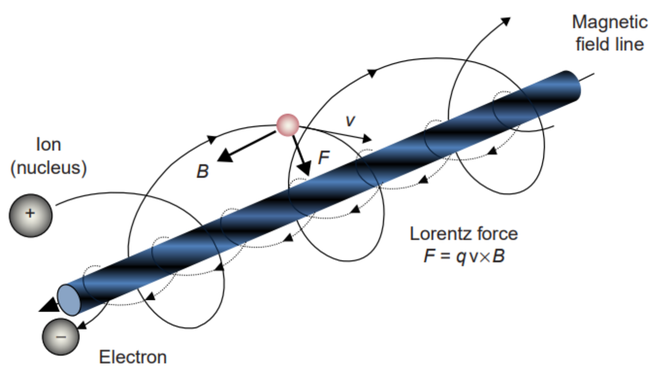

Fig. 8 Schematic of the orbit of charged particles in a magnetic field line. Reproduced from Yamada H. Fusion energy. In: Chen WY, Seiner J, Suzuki T, Lackner M, editors. Handbook of climate change mitigation. New York, NY: Springer; 2012. p. 1195–7.

Confinement with Magnetic Mirrors:

A magnetic mirror confines plasma using a magnetic field that is strong at the ends and weaker in the center of a solenoidal device.
Charged particles moving along magnetic field lines reflect at the strong-field ends due to conservation of energy and magnetic moment, creating a mirror effect.
Electrons and ions with high axial velocity can escape, but many particles become trapped in the central region.

Quantity	Equation	Meaning
Total Energy	$W = \frac{1}{2}m(v_\parallel^2 + v_\perp^2)$	Conserved
Magnetic Moment	$\mu = \frac{1}{2}\frac{mv_\perp^2}{B}$	Adiabatic invariant
Mirror Ratio	$R_m = \frac{B_m}{B_0}$	Magnetic field strength ratio
Loss Cone Condition	$\sin^2\theta_0 > \frac{1}{R_m}$	Trapping condition
Mirror Force	$F_\parallel = -\mu\frac{dB}{ds}$	Acts against particle escape

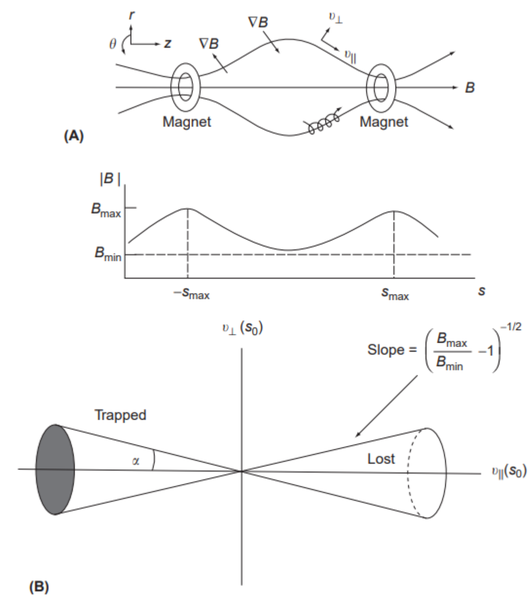

Fig. 19 (A) Simple mirror configuration and (B) loss cone. Reproduced from Stacey WM. Fusion: an introduction to the physics and technology of magnetic confinement. 2nd ed. Weinheim: Wiley-VCH; 2010. p. 38–9.

Result is The TOKAMAK

The idea of the tokamak—a toroidal magnetic confinement device for plasma—originated in the **Soviet Union in the 1950s** during the early days of controlled thermonuclear fusion research. The concept was proposed by two Soviet physicists, **Andrei Sakharov** and **Igor Tamm**, in **1950** as a solution to the problem of plasma confinement using magnetic fields. They theorized that a toroidal (doughnut-shaped) magnetic field, augmented by a poloidal magnetic component generated by a plasma current, could confine plasma more effectively than previous linear or simple toroidal configurations.
.

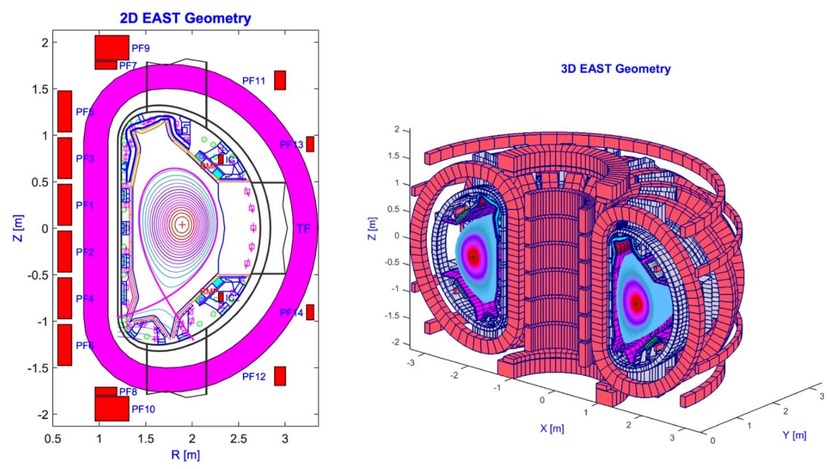

How It Works?

A large toroidal magnetic field is generated by external coils.

A plasma current, induced by a central solenoid, creates a poloidal magnetic field.
Together, these fields produce helical magnetic field lines that twist around the torus and confine the plasma in a stable configuration.

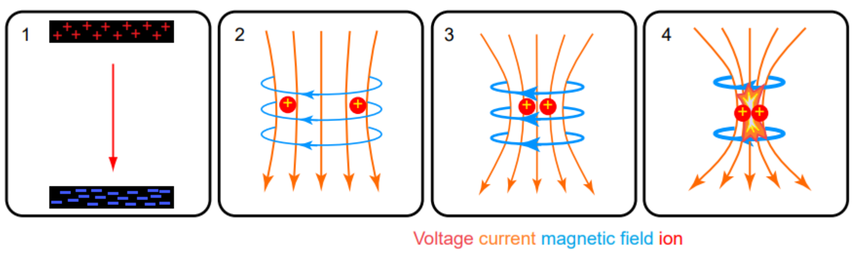

Fig. 24 Schematic of the basic principle of Z-pinch. Courtesy of WikiHelper2134 at en.wikipedia.

Energy Extraction

The high-energy **neutrons**, being uncharged, escape the magnetic field and strike a **blanket** surrounding the plasma chamber.
The blanket **absorbs neutron energy** and converts it into **heat**, which can then be used to produce **steam** and drive **turbines**—just like in conventional power plants.

KAYNAKÇA

[1] https://doi.org/10.1016/B978-0-12-809597-3.00330-8
[2] Bittencourt, J. A. (2004). Fundamentals of Plasma Physics (3rd ed.). Springer.
[3] Chen, F. F. (2016). Introduction to Plasma Physics and Controlled Fusion (3rd ed.). Springer.

YTÜ FEN EDEBİYAT FAKÜLTESİ

2024-2025 Bahar Yarıyılı FİZİK BÖLÜMÜ

Tavlama Sıcaklığının Hidrotermal Yöntem ile Sentezlenen Magnezyum Ferritlerin Yapısal ve Dielektrik Özelliklerine Etkisi

Selen ÇAMLI 19022060

Danışman: Doç. Dr. Banu SÜNGÜ MISIRLIOĞLU

ÖZET

Bu çalışmada, magnezyum ferrit ($MgFe_2O_4$) nanoparçacıklar hidrotermal yöntemle sentezlenmiş ve farklı tavlama sıcaklıklarının (700 °C ve 900 °C) bu yapıların kristal fazı ve dielektrik özellikleri üzerindeki etkileri araştırılmıştır.Sentez sonrası karakterizasyon için XRD, FTIR ve empedans spektroskopisi teknikleri kullanılmıştır. XRD analizleri her iki sıcaklıkta da kübik spinel yapının oluştuğunu doğrulamış, ancak 900 °C'de tavlanan örneklerin daha yüksek kristal saflığı ve daha düşük tanecik boyutu gösterdiği belirlenmiştir. FTIR analizleri ile metal-oksijen bağlarının tavlama sıcaklığına bağlı frekans kaymaları gösterdiği gözlemlenmiştir.Dielektrik ölçümler sonucunda, 700 °C'de tavlanan örneklerin daha yüksek ε' ve ε" değerlerine sahip olduğu; buna karşın 900 °C'de daha belirgin bir Debye gevşeme davranışı gösterdiği saptanmıştır.Sonuçlar, 900 °C tavlama sıcaklığının yapısal saflık açısından optimum değer olduğunu; 700 °C'nin ise yüksek dielektrik performans için avantaj sunduğunu göstermektedir. Bu bulgular, $MgFe_2O_4$ nanoparçacıkların enerji depolama ve elektronik uygulamalarda kullanılabilirliğini desteklemektedir.

GİRİŞ

Spinel ferritler, genel formülleri MFe_2O_4 (M = Mg^{2+}, Ni^{2+}, Zn^{2+}, Co^{2+} vb.) olan, manyetik seramik malzemelerdir. Kristal yapılarındaki esneklik ve iyonik dağılım sayesinde hem elektriksel hem de manyetik özellikleri sentez ve işlem koşullarına oldukça duyarlıdır. Bu özellikleri nedeniyle ferritler; sensörler, mikrodalga aygıtları, enerji depolama sistemleri ve biyomedikal cihazlar gibi birçok alanda yaygın olarak kullanılmaktadır.

Magnezyum ferrit ($MgFe_2O_4$), düşük toksisite, yüksek termal kararlılık ve kimyasal inertlik özellikleriyle ön plana çıkan karışık spinel yapılı ferritlerdendir. Mg^{2+} iyonunun manyetik olmayan doğası, Fe^{3+} iyonlarının ferrimanyetik katkısını kontrol etme olanağı sağlayarak, optimize edilebilen bir elektriksel ve manyetik yanıt oluşturur. Ayrıca yarı iletken karakteri sayesinde eddy current (girdap akımı) oluşumunu baskılayarak yüksek frekanslı uygulamalarda avantaj sunar. Ferritlerin fiziksel ve elektriksel özellikleri üzerinde en belirleyici parametrelerden biri tavlama sıcaklığıdır. Tavlama, kristal yapı kusurlarını azaltarak faz saflığını artırmakta; tanecik boyutu, porozite ve mikro gerilmeler gibi yapısal özellikleri doğrudan etkilemektedir. Bu bağlamda, literatürde magnezyum ferritlerin sentezinde hidrotermal yöntem gibi çevre dostu, düşük sıcaklıkta çalışan ve homojen yapı sağlayan teknikler ön plana çıkmaktadır.

Bu çalışmada, $MgFe_2O_4$ nanoparçacıkları hidrotermal yöntemle sentezlenmiş; ardından 700 °C ve 900 °C'de tavlanarak yapısal ve dielektrik özellikleri karşılaştırmalı olarak incelenmiştir. Elde edilen sonuçlar, tavlama sıcaklığının hem kristal düzen hem de dielektrik performans üzerinde belirgin etkileri olduğunu ortaya koymaktadır.

DENEYSEL YÖNTEM

Sentez İçin Kullanılan Kimyasallar

Çalışmada, analitik saflıkta magnezyum nitrat hekzahidrat [$Mg(NO_3)_2{\cdot}6H_2O$], demir(III) nitrat nonahidrat [$Fe(NO_3)_3{\cdot}9H_2O$], sodyum hidroksit (NaOH), distile su ve etanol kullanılmıştır. Kimyasallar hiçbir ek saflaştırma işlemine tabi tutulmamıştır.

Hidrotermal Sentez Prosedürü

$MgFe_2O_4$ nanoparçacıklarının sentezi için Mg^{2+} ve Fe^{3+} iyonları arasındaki molar oran 1:2 olacak şekilde çözeltiler hazırlanmıştır. $Mg(NO_3)_2{\cdot}6H_2O$ ve $Fe(NO_3)_3{\cdot}9H_2O$, distile su içerisinde ayrı ayrı çözüldükten sonra manyetik karıştırıcı ile yaklaşık 30 dakika boyunca homojen bir karışım elde edilene kadar karıştırılmıştır. Daha sonra çözeltiye damla damla NaOH ilavesi yapılmış ve pH değeri 10–11 arasında sabit tutulmuştur. Bu bazik ortam, iyonların hidroksit formuna dönüşerek spinel yapının oluşumunu sağlamaktadır.

Hazırlanan çözelti, PTFE kaplamalı paslanmaz çelik hidrotermal otoklav reaktörüne aktarılmıştır. Reaktör, 180°C'de 16 saat süreyle reaksiyona tabi tutulmuştur. Bu kapalı sistemdeki yüksek sıcaklık ve basınç koşulları, kristal büyümesini ve istenilen spinel yapı oluşumunu teşvik etmiştir. Reaksiyon tamamlandıktan sonra otoklav oda sıcaklığına soğutulmuş ve elde edilen çökelti santrifüjle ayrılarak distile su ve etanol ile yıkanmıştır. Yıkama işlemi, iyonik kalıntıların giderilmesi ve aglomerasyonun önlenmesi amacıyla gerçekleştirilmiştir. Sonrasında ürün 80°C'de 12 saat süreyle kurutulmuş ve havanda toz haline getirilmiştir.

Tavlama İşlemi

Sentezlenen magnezyum ferrit nanoparçacıkların kristal yapısını geliştirmek, safsızlıkları azaltmak ve dielektrik özellikleri optimize etmek amacıyla ısıl işlem uygulanmıştır. Örnekler, iki farklı sıcaklıkta tavlanmıştır: Bir grup 700° C'de, diğer grup 900°C'de olmak üzere her iki gruba 6 saat tavlama işlemi uygulanmıştır. Tavlama sonrası örnekler yapısal ve dielektrik karakterizasyon için hazırlanmıştır.

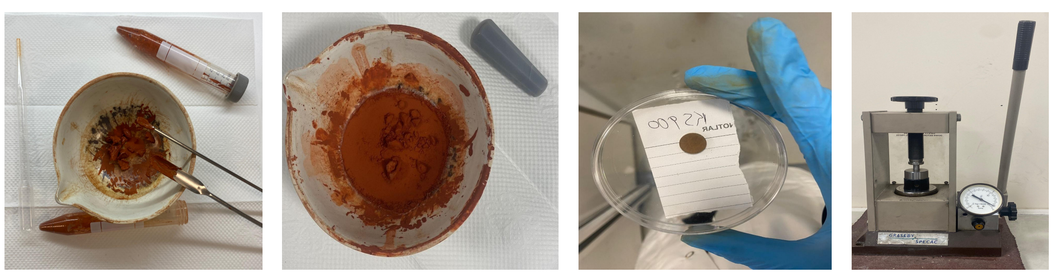

Yapısal ve Dielektrik Özelliklerin Karakterizasyonu

Magnezyum ferrit örneklerinin yapısal ve dielektrik özellikleri XRD, FTIR ve empedans spektroskopisi yöntemleriyle incelenmiştir.

XRD analizleri, kristal yapı ve faz bilgisi için 20°–80° 2θ aralığında, PANalytical EMPYREAN cihazı ile yapılmıştır. Elde edilen pikler, spinel yapıyı doğrulamış; Debye-Scherrer denklemi ile kristalit boyutları hesaplanmıştır.

FTIR analizleri, 4000–400 cm^{-1} aralığında Perkin Elmer Spectrum 100 cihazı ile gerçekleştirilmiştir. 500–700 cm^{-1}'de gözlemlenen Mg–O ve Fe–O titreşimleri, spinel yapının varlığını desteklemiştir. Pik kaymaları, tavlama sıcaklığına bağlı yapısal değişimleri göstermiştir.

Empedans spektroskopisi ile örneklerin frekansa bağlı dielektrik özellikleri (ε', ε", Z', Z") ölçülmüştür. Ölçümler, 10 Hz–10 MHz aralığında Novocontrol Alpha-AN cihazı ile yapılmıştır. Veriler, elektriksel davranışın tavlama sıcaklığına bağlı olarak değiştiğini göstermiştir.

BULGULAR ve TARTIŞMA

Bu çalışmada, hidrotermal yöntemle sentezlenen $MgFe_2O_4$ nanoparçacıkların 700 °C ve 900 °C tavlama sıcaklıklarında yapısal ve dielektrik özellikleri karşılaştırılmıştır. XRD analizleri her iki örnekte de karakteristik kübik spinel yapının başarıyla oluştuğunu göstermiştir. Ancak 700 °C'de tavlanan örnekte yaklaşık 33° civarında Fe–O safsızlık pikine rastlanmış, buna karşılık 900 °C'de tavlanan örneklerde bu pik ortadan kalkmış ve daha saf bir kristal yapı elde edilmiştir. Ayrıca, 900 °C tavlama sıcaklığında kristalit boyutunun 46.6 nm'ye düştüğü, 700 °C örneğinde ise 65.3 nm olduğu hesaplanmıştır. Piklerin daralması ve şiddetlerinin artması, kristalitenin yükseldiğine işaret etmektedir.

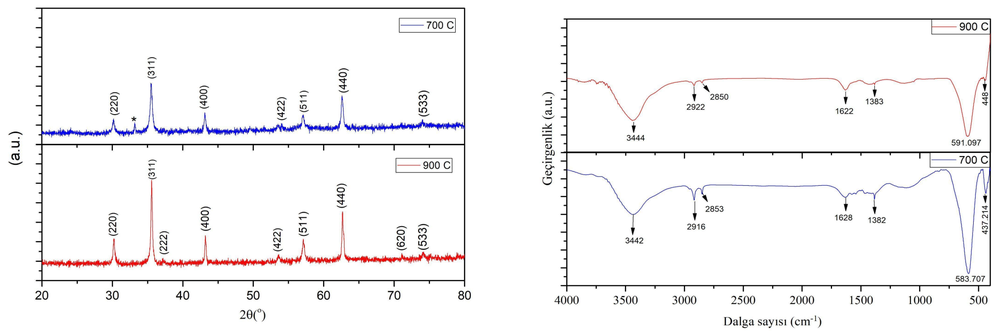

FTIR analizinde, her iki örnekte de 400–700 cm^{-1} aralığında Fe–O ve Mg–O bağlarına ait titreşim modları gözlemlenmiştir. 900 °C tavlama sonrası bu piklerde frekans kaymaları meydana gelmiş, bu da sıcaklığa bağlı olarak metal–oksijen bağ uzunluklarında değişimler yaşandığını göstermektedir. Ayrıca –OH gruplarına, nitrat kalıntılarına ve C–H gerilme titreşimlerine ait ek bantlar da tespit edilmiştir.

Empedans spektroskopisi ile elde edilen dielektrik veriler, her iki örnekte de düşük frekanslarda ε' ve ε" değerlerinin yüksek olduğunu, frekans arttıkça bu değerlerin azaldığını ortaya koymuştur. Bu durum, tipik bir Maxwell–Wagner tipi arayüzey polarizasyonuna işaret etmektedir. 700 °C'de tavlanan örneklerin dielektrik sabitleri daha yüksek çıkarken, 900 °C'de daha belirgin bir Debye tipi gevşeme davranışı gözlenmiştir.

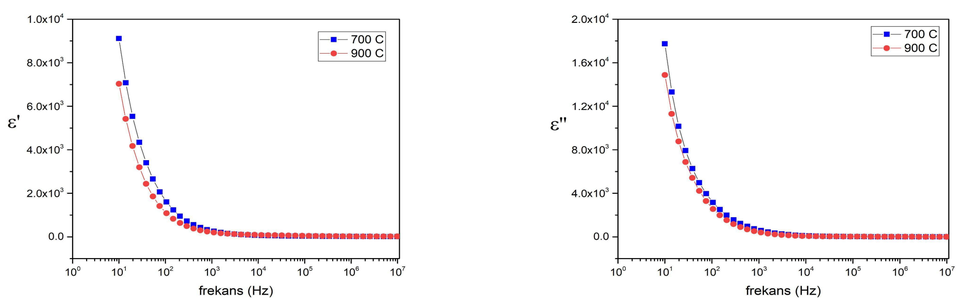

Z' ve Z" parametrelerinin frekansa bağlı değişimi incelendiğinde ise, düşük frekanslarda yüksek direnç ve reaktans değerleri elde edilmiş, bu değerlerin frekansla birlikte azaldığı belirlenmiştir. 900 °C tavlama sıcaklığında bu parametrelerin maksimum yaptığı frekans bölgesi daha net şekilde belirlenmiştir.

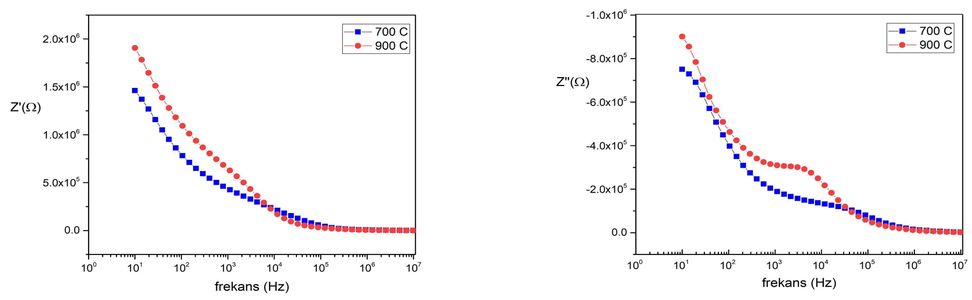

Tüm veriler bir arada değerlendirildiğinde, 900 °C tavlama sıcaklığının kristal yapı saflığını artırdığı, ancak parçacık boyutundaki azalma ile birlikte dielektrik parametrelerde hafif düşüşlere yol açtığı anlaşılmıştır. Buna karşılık, 700 °C'de tavlanan örnekler daha yüksek dielektrik sabit değerleri ile enerji depolama uygulamaları açısından daha avantajlı bir performans sergilemiştir.

SONUÇ

Bu çalışmada, $MgFe_2O_4$ nanoparçacıkları hidrotermal yöntemle sentezlenmiş ve 700 °C ile 900 °C tavlama sıcaklıklarında elde edilen örneklerin yapısal ve dielektrik özellikleri karşılaştırılmıştır. XRD analizleri, her iki sıcaklıkta da kübik spinel yapının başarıyla oluştuğunu; ancak 900 °C'de safsızlık piklerinin ortadan kalktığını ve kristalitenin arttığını göstermiştir. Buna karşılık parçacık boyutunda küçülme gözlenmiştir.

FTIR analizlerinde, metal–oksijen bağlarının titreşim frekanslarında sıcaklığa bağlı kaymalar saptanmış, bu durum bağ uzunluklarının ve iyonik dağılımın sıcaklıktan etkilendiğini göstermiştir. Dielektrik ölçümler, 700 °C'de tavlanan örneklerin daha yüksek ε' ve ε" değerlerine sahip olduğunu; 900 °C'de ise daha belirgin bir Debye gevşeme piki gözlemlendiğini ortaya koymuştur.

Genel değerlendirmede, 900 °C tavlama sıcaklığının daha saf ve düzenli kristal yapı sağladığı, 700 °C'nin ise daha yüksek dielektrik sabitleri sunduğu belirlenmiştir. Bu sonuçlar, $MgFe_2O_4$ nanoparçacıkların enerji depolama sistemleri gibi uygulamalarda sentez ve işlem parametrelerine bağlı olarak özelleştirilebileceğini göstermektedir.

KAYNAKÇA

[1] Süngü Mısırlıoğlu, B., Kahya, N. D., & Öztürk, Z. (2024). Enhanced dielectric properties of copper substituted nickel ferrite nanoparticles for energy storage applications. *Journal of Physics and Chemistry of Solids, 193*, 112195.
[2] Mahmood, M. et al., *Materials Chemistry and Physics*, 2021
[3] Öztürk, A., & Demir, S., *Ceramics International*, 2020

Video izlemek için tarayın

2024-2025 Bahar Yarıyılı FİZİK BÖLÜMÜ

GREEN'S FUNCTION METHOD IN SUPERCONDUCTIVITY

Yasin YILANCIOĞLU 20022006

Supervisor: Prof. Dr. Kutsal BOZKURT

ABSTRACT

The study begins by introducing Green's functions and demonstrating how they are used to solve differential equations. Then, the fundamental properties of superconductors are introduced, and delves into Green's functions in many-body systems, and then we see approximation and construction for a theory for the superconductivity.

GREEN'S FUNCTION METHOD

The Green's function is a powerful mathematical tool for solving inhomogeneous linear differential equations, and it is used in many areas in physics. It represents the response of a physical system to a point source or impulse. The application of Green's functions is widespread across many areas of physics. In quantum mechanics and quantum field theory, the Green's function or propagator describes the probability amplitude for a particle which moves from one point to another. This powerful tool is also used to describe the phenomena of superconductivity.

GREEN'S FUNCTION .

Green's functions can be defined as solutions of inhomogeneous differential equations of the type [1]

$$[z - L(r)]G(r, r'; z) = \delta(r - r')$$

subject to certain boundary conditions (BCs) for r or r' lying on the surface S of the domain Ω of r and r' . Here we assume that z is a complex variable and that L(r) is a time-independent, linear, hermitian differential operator that possesses a complete set of eigenfunctions $\{\phi_n(r)\}$. Equation can be written more explicitly as

$$G(z) = \sum_n \frac{|\phi_n\rangle\langle\phi_n|}{z - \lambda_n} + \int dc \frac{|\phi_c\rangle\langle\phi_c|}{z - \lambda_c}$$

Knowledge of the Green's function G (r, r' ; z) permits us to obtain immediately the solution of the general inhomogeneous equation

$$[z - L(r)]u(r) = f(r)$$

u(r) satisfies the same BCs as G(r, r' ; z). the solution of the equations is

$$u(r) = \int G(r, r'; z) f(r') dr' \quad , z \neq \{\lambda_n\}$$

u(r) describes the response of a system to a source f(r), then G(r, r') describes the response to a unit point source at r ' in the same system. The response at r from a source at r ' is the same as the response at r ' from a source at r. The response to the general source f(r) can be expressed as the sum of the responses to point sources distributed according to f(r)[1].

SUPERCONDUCTIVITY

Superconductivity is a macroscopic quantum phenomenon characterized by zero electrical resistance and the expulsion of magnetic fields (the Meissner effect) below a critical temperature T_c. The phenomenon originates from the formation of bound electron pairs, known as Cooper pairs, and is described microscopically by the Bardeen–Cooper–Schrieffer (BCS) theory.

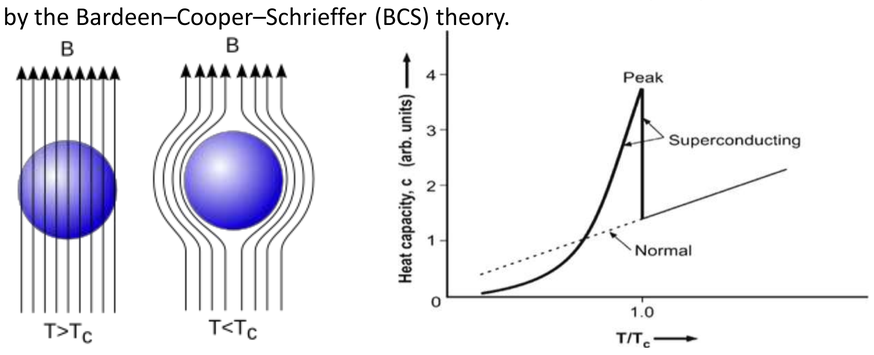

GREEN'S FUNCTION IN MANY-BODY SYSTEMS

The single particle Green's function is defined by the equation [2]

$$iG_{\alpha,\beta}(xt, x't') = \frac{\langle\Psi_0|T[\hat{\psi}_{H,\alpha}(xt)\,\hat{\psi}^{\dagger}{}_{H,\beta}(x't')]|\Psi_0\rangle}{\langle\Psi_0|\Psi_0\rangle}$$

Ψ_0 is the Heisenberg ground state, and $\hat{\psi}$, $\hat{\psi}^{\dagger}$ are Heisenberg destruction and creation field operators. α, β indices for spin-1/2 fermions, (α = 1/2 or α = −1/2).

BCS THEORY AND COOPER PAIRS

BCS theory explains superconductivity with Cooper pairs. When an electron moves in a lattice, it distorts the positively charged ions, the electron pulls surrounding positive ions into itself. This distortion creates positive charge density then the second electron that is attracted by a positive charge density creates the formation of the Cooper pair. Cooper pairs can move freely and overlap within the material. Because each pair consists of two electrons with opposite spins, their total spin is an integer, causing them to behave like bosons. When electrons form Cooper pairs, they settle into the lowest energy state. Unpaired individual electrons are more energetic compared to the paired state, which leads to creation of an energy gap (Δ) between the paired and unpaired states

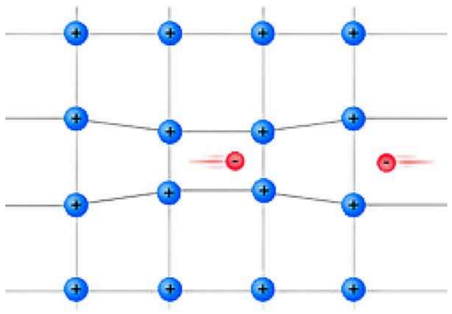

GENERAL FORMULATION OF THE BCS THEORY

Grand canonical hamiltonian for an electron gas in a magnetic field is given by [2]

$$\hat{K} = \hat{K}_0 + \hat{V} = \int d^3x\, \hat{\psi}^{\dagger}_{\alpha}(x) \left\{ \frac{1}{2m} \left[-i\hbar\boldsymbol{\nabla} + \frac{e\boldsymbol{A}(\boldsymbol{x})}{c} \right]^2 - \mu \right\} \hat{\psi}_{\alpha}(x) - \frac{1}{2} g \int d^3x \hat{\psi}^{\dagger}_{\alpha}(x) \hat{\psi}^{\dagger}_{\beta}(x) \hat{\psi}_{\beta}(x) \hat{\psi}_{\alpha}(x)$$

We are going to solve this using the Hartree-Fock approximation ($\hat{V} \approx \hat{V}_{HF}$).The single-particle Green's function satisfies the equation of motion. Key aspect of the superconductivity is Cooper pair. BCS theory models this phenomenon by adding two terms representing the pairing amplitude.

$$\hat{V} \approx \hat{V}_{HF} - \frac{1}{2} g \int d^3x \left[\left\langle \hat{\psi}^{\dagger}_{\alpha}(x) \hat{\psi}^{\dagger}_{\beta}(x) \right\rangle \hat{\psi}_{\beta}(x) \hat{\psi}_{\alpha}(x) + \hat{\psi}^{\dagger}_{\alpha}(x) \hat{\psi}^{\dagger}_{\beta}(x) \langle \hat{\psi}_{\beta}(x) \hat{\psi}_{\alpha}(x) \rangle \right]$$

Since the formation of the superconducting state is about the energy gap and the condensation energy, any term that does not affect this difference can often be ignored for simplicity[2]. Using this approach our potential only consists of Cooper pairs potential. And total hamiltonian becomes

$$\hat{K}_{eff} = \hat{K}_0 - g \int d^3x \left[\langle \hat{\psi}^{\dagger}_{\downarrow}(x) \hat{\psi}^{\dagger}_{\uparrow}(x) \rangle \hat{\psi}_{\uparrow}(x) \hat{\psi}_{\downarrow}(x) + \hat{\psi}^{\dagger}_{\downarrow}(x) \hat{\psi}^{\dagger}_{\uparrow}(x) \langle \hat{\psi}_{\uparrow}(x) \hat{\psi}_{\downarrow}(x) \rangle \right]$$

Using Green's function, we are going to find the evolution of the propagation of the electron at x respect to τ

$$\hbar \frac{\partial \mathcal{G}(x\tau, x'\tau')}{\partial \tau} = -\hbar\delta(x - x')\delta(\tau - \tau') - \left[\frac{1}{2m} \left(-i\hbar\boldsymbol{\nabla} + \frac{e\boldsymbol{A}(x)}{c} \right)^2 - \mu \right] \times \mathcal{G}(x\tau, x'\tau') + g \langle \hat{\psi}_{\uparrow} \hat{\psi}_{\downarrow} \rangle \langle T_{\tau} [\hat{\psi}^{\dagger}_{K\downarrow}(xt) \hat{\psi}^{\dagger}_{K\uparrow}(x't')] \rangle$$

Now, we introduce two new functions. They are called anomalous Green's functions

$$\mathcal{F}(x\tau, x'\tau') \equiv -\langle T_{\tau} [\hat{\psi}_{K\uparrow}(xt) \hat{\psi}_{K\downarrow}(x't')] \rangle$$

$$\mathcal{F}^{\dagger}(x\tau, x'\tau') \equiv -\langle T_{\tau} [\hat{\psi}^{\dagger}_{K\downarrow}(xt) \hat{\psi}^{\dagger}_{K\uparrow}(x't')] \rangle$$

The gap function $\Delta(x)$ is defined by

$$\Delta(x) \equiv g\mathcal{F}(x\tau, x'\tau') \equiv \langle \hat{\psi}_{K\downarrow}(xt) \hat{\psi}_{K\uparrow}(x't') \rangle$$

and equation becomes

$$\left[-\hbar \frac{\partial}{\partial \tau} - \frac{1}{2m} \left(-i\hbar\boldsymbol{\nabla} + \frac{e\boldsymbol{A}(\boldsymbol{x})}{c} \right)^2 + \mu \right] \mathcal{G}(x\tau, x'\tau') - \Delta(x) \mathcal{F}^{\dagger}(x\tau, x'\tau') = \hbar\delta(x - x')\delta(\tau - \tau')$$

The functions F and F† also obey the equations of the motion. We obtain

$$\left[-\hbar \frac{\partial}{\partial \tau} - \frac{1}{2m} \left(-i\hbar\boldsymbol{\nabla} + \frac{eA(x)}{c} \right)^2 + \mu \right] \mathcal{F}^{\dagger}(x\tau, x'\tau') - \Delta^*(x) \mathcal{G}(x\tau, x'\tau') = 0$$

Fourier Transform of Superconductivity Green's Function

In the usual case, the hamiltonian is time independent, and Green's functions depend only on τ − τ ' .Therefore, it is useful to switch from time and position space to frequency and momentum space. Fourier representations of the normal Green's function and the anomalous Green's function

$$\mathcal{G}(x\tau, x'\tau') = (\beta\hbar)^{-1} \sum_n e^{-i\omega_n(\tau - \tau')}\, \mathcal{G}(x, x', \omega_n)$$

$$\mathcal{F}^{\dagger}(x\tau, x'\tau') = (\beta\hbar)^{-1} \sum_n e^{-i\omega_n(\tau - \tau')}\, \mathcal{F}^{\dagger}(x, x', \omega_n)$$

In this initial analysis, we choose to ignore the magnetic field in order to simplify the problem. It is impossible to solve both the microscopic Gor'kov equations for electrons and Maxwell's equations for the electromagnetic field at the same time. By setting the magnetic field to zero, we can focus on the fundamental mechanism of superconductivity itself.

$$\mathcal{G}(\boldsymbol{x}, \omega_n) = (2\pi)^{-3} \int d^3k\, e^{i\boldsymbol{k}\cdot\boldsymbol{x}}\, \mathcal{G}(\boldsymbol{k}, \omega_n)$$

$$\mathcal{F}^{\dagger}(\boldsymbol{x}, \omega_n) = (2\pi)^{-3} \int d^3k\, e^{i\boldsymbol{k}\cdot\boldsymbol{x}}\, \mathcal{F}^{\dagger}(\boldsymbol{k}, \omega_n)$$

When these pair of equations are solved, our normal and anomalous Green's function becomes

$$\mathcal{G}(\boldsymbol{k}, \omega_n) = \frac{-\hbar(i\hbar\omega_n + \xi_k)}{\hbar^2\omega_n^2 + \xi_k^2 + |\Delta|^2}$$

$$\mathcal{F}^{\dagger}(\boldsymbol{k}, \omega_n) = \frac{\hbar\Delta^*}{\hbar^2\omega_n^2 + \xi_k^2 + |\Delta|^2}$$

The poles of these equations tell us the energies of the elementary excitations of the system. To find these energies, we switch from the imaginary Matsubara frequency $i\hbar\omega_n$ to a real energy E. The condition for an excitation is then

$$-E^2 + \xi_k^2 + |\Delta|^2 = 0$$

$$E_k = \sqrt{\xi_k^2 + |\Delta|^2}$$

This is the BCS quasiparticle dispersion relation.

REFERENCES

[1] E. N. Economou, Green's functions in quantum physics. Springer Science & Business Media, 2006, vol. 7.
[2] A. L. Fetter, J. D. Walecka, Quantum theory of many-particle systems. Courier Corporation, 2012.
[3] A. A. Abrikosov, L. P. Gorkov, I. E. Dzyaloshinski, Methods of quantum field theory in statistical physics. Courier Corporation, 2012.

2024-2025 Spring Semester DEPARTMENT OF PHYSICS

Neuromorphic Photonic Networks and Neurophox: Functionality, Usefulness, and Future Prospects

Ahmet Cemil TOPRAK (123456789)

Prof. Dr. Bora Işıldak

Abstract

While the increasing computational demands of artificial intelligence are challenging traditional architectures due to physical limitations such as the slowdown of Moore's Law, this study examines neuromorphic photonic networks (NPNs) as a revolutionary solution. This thesis investigates the potential and challenges of NPNs, which combine the speed and energy efficiency advantages of light with computation inspired by the structure of the brain, using the open source Neurophox simulation tool. In this context, an NPN model is created that performs the MNIST handwritten digit recognition task; its performance is evaluated comparatively with a traditional electronic neural network in terms of classification success and energy efficiency. Finally, this study aims to reveal the performance benefits and practical implementation challenges offered by NPNs and to show how simulation tools such as Neurophox accelerate the research-development cycle in this field.

Motivation: The Crises of Traditional Computing

Modern artificial intelligence (AI) is pushing traditional computing architectures to their breaking point, creating two fundamental and interconnected crises that necessitate a new paradigm.

•**The Power Wall:** The predictable, exponential growth described by Moore's Law has significantly slowed. As transistors shrink to nanometer scales, fundamental physical limits like quantum tunneling and extreme heat dissipation have become major obstacles. This "power wall" means we can no longer rely on smaller transistors for faster and more efficient processors.

•**The Data Wall:** Compounding this issue is the "von Neumann bottleneck," an architectural flaw inherent in most computers where the processor and memory are physically separate. In the age of AI, with models containing billions of parameters, the constant shuttling of data between memory and processing units has become the dominant source of energy consumption. This "data wall" means more energy is spent on moving data than on the computation itself, creating an unsustainable energy crisis for scaling AI.

Proposed Solution: Neuromorphic Photonic Networks (NPNs)

Neuromorphic Photonic Networks (NPNs) offer a revolutionary approach that simultaneously addresses both the power and data walls by merging two powerful concepts.

•**The Neuromorphic Principle:** Inspired by the human brain's efficiency, neuromorphic computing co-locates memory and processing (in-memory computing), which fundamentally eliminates the von Neumann bottleneck and its associated data movement costs. By emulating the brain's massive parallelism and event-driven, asynchronous communication, these architectures promise extraordinary gains in energy efficiency.

•**The Photonic Advantage:** Using photons (light) instead of electrons for computation provides a leap in performance. Photons travel at the speed of light, offer enormous bandwidth, and can be transmitted through waveguides with minimal energy loss and heat generation. This allows for computation that is orders of magnitude faster and more energy-efficient than electronics, directly tackling the power wall's thermal constraints.

This thesis investigates the potential of NPNs, which leverage photonics to perform the core mathematical operation of AI—matrix-vector multiplication—at the speed of light, creating a powerful synergy that promises to redefine high-performance computing.

Methodology

Our research employs a systematic framework to compare electronic and photonic neural networks, combining simulation-based performance evaluation with a theoretical, component-level energy analysis.

•**Simulation Tools:** We utilize **Neurophox**, an open-source Python framework designed for simulating optical neural networks based on unitary mesh architectures. Its seamless integration with **TensorFlow** allows us to use standard machine learning workflows, like backpropagation, to directly train the physical parameters of the photonic hardware, such as the phase shifts in a Mach-Zehnder Interferometer (MZI) network.

•**Network Architecture and Task:** To ensure a fair comparison, we use a Multilayer Perceptron (MLP) architecture for both the electronic and photonic models. The classic model consists of two 64-neuron hidden layers with ReLU activations. In the photonic model, these linear layers are replaced with Neurophox's MZI-based RMTorch layers for matrix multiplication and the activations are replaced with ElectroopticNonlinearity layers. The models are trained and evaluated on the standard MNIST handwritten digit classification task, a benchmark widely used for validating the fundamental functionality of new hardware paradigms.

- **Comparative Analysis:** The two models are compared based on two key criteria:
  - **1.Performance:** Functional accuracy is evaluated through classification success on the test dataset.
  - **2.Energy Efficiency:** A theoretical energy analysis is conducted, breaking down consumption into its dynamic components (computation) and static components (maintaining the hardware state).

Results: Simulation and Performance

Under idealized simulation conditions, which exclude real-world hardware noise and defects, the photonic model demonstrated functional equivalence to its traditional electronic counterpart.

•**Learning Performance:** Both the electronic and photonic models showed a rapid and comparable decrease in error rate and test loss during the 60 training epochs, indicating that both architectures learned the classification task effectively.

•**Classification Accuracy:** The confusion matrices generated from the test set results are identical for both models. This visually confirms that the simulated NPN, under ideal conditions, successfully replicated the high-accuracy classification performance of the conventional electronic network, achieving results consistent with the >97% accuracy reported in similar simulation-based studies.

Classic Model Learning Performance

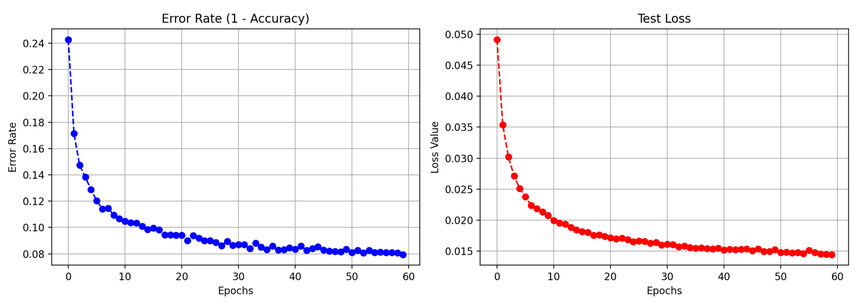

Photonic Model Learning Performance

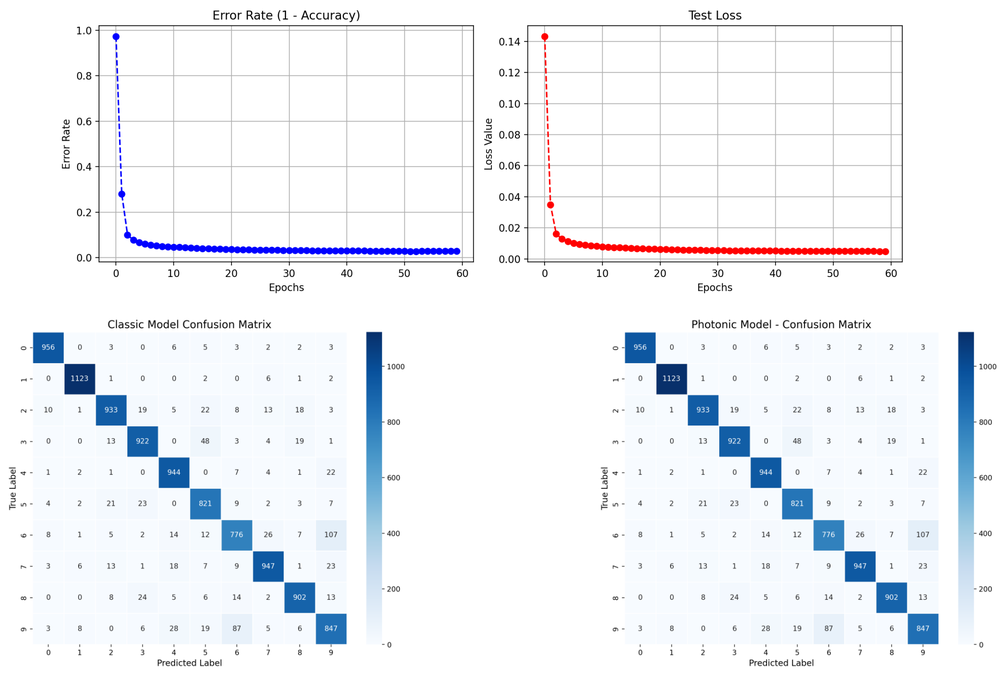

Analysis and Discussion

While the simulation results are promising, a deeper analysis reveals a significant gap between theoretical potential and practical reality, highlighting the key challenges facing NPN technology.

•**The Performance Gap:** Real-world photonic circuits are subject to imperfections like optical loss, thermal crosstalk between components, and manufacturing defects. As networks scale in size, these small errors accumulate and can cause a catastrophic degradation in performance, with some studies reporting accuracy drops of up to 84%. This underscores the need for noise-robust architectures and advanced training methods.

•**The Energy Paradox:** A simple "energy per operation" metric is misleading. While the dynamic energy for a single photonic computation (a MAC operation) is incredibly low (in the femtojoule range) compared to electronics (picojoule range), the total system energy is dominated by other factors. The primary energy cost comes from the high *static* power required by the thermo-optic phase shifters used to hold the network's weights (around 5–20 mW per shifter) and the energy for opto-electronic conversions in hybrid systems.

- **Fundamental Challenges:** The primary obstacles for current NPN technology are:
  - **1.High Static Power Consumption:** This makes NPNs inefficient for tasks with idle time and drives research toward non-volatile memory solutions.
  - **2.Efficient Optical Nonlinearity:** The lack of a practical, all-optical nonlinear activation function necessitates hybrid opto-electronic solutions, which reintroduce electronic bottlenecks.
  - **3.Hardware Imperfections and Scalability:** Overcoming the effects of physical noise and defects is critical for building reliable, large-scale systems.

Conclusion and Future Perspective

This thesis concludes that Neuromorphic Photonic Networks are poised to become a powerful complementary technology, augmenting rather than replacing traditional electronics, especially in hybrid systems designed for specific, high-throughput tasks.

•**Contributions:** This work provides a holistic methodological framework for evaluating NPNs by combining simulation with a realistic, component-level energy analysis. It clearly defines the application domains where current NPNs can provide the most benefit (e.g., continuous data stream processing) and analyzes the critical role of simulation tools like Neurophox in bridging the gap between theory and hardware.

•**Future Directions:** The future of NPNs depends on overcoming the key challenges identified. The most critical research directions are:

- **Non-Volatile Photonic Memories:** Developing technologies like Phase-Change Materials (PCMs) is essential to eliminate the high static power consumption of current weight-storage mechanisms.
- **Hardware-Aware Training:** Creating advanced training algorithms, such as Physics-Aware Training (PAT) and Sharpness-Aware Training (SAT), that can make models robust to the inherent noise and imperfections of physical hardware is crucial for closing the simulation-to-reality gap and unlocking the true potential of photonic computing.

KAYNAKÇA

[1] B. J. Shastri, A. N. Tait, T. F. de Lima, W. H. Pernice, H. Bhaskaran, C. D. Wright, and P. R. Prucnal, “Neuromorphic photonics,” Nature Photonics, vol. 15, no. 2, pp. 102–114, 2021.

[2] J. Spall, S. Pai, et al., “Neurophox: An open source machine learning and pho-tonic simulation framework.” https://github.com/solgaardlab/neurophox, 2021.

[3] J. Feldmann, N. Youngblood, M. Karpov, H. Gehring, X. Li, M. Stappers, M. Le Gallo, X. Fu, A. Lukashchuk, A. Raja, et al., “Parallel convolutional processing using an integrated photonic tensor core,” Nature, vol. 589, no. 7840, pp. 52–58, 2021.

FİZİK BÖLÜMÜ

DETERMİNATION OF JET ENERGY CORRECTION FACTORS IN PARTICLE PHYSICS BASED ON JET IMAGES USING DEEP LEARNİNG

Baha KONUKOĞULLARI 20022022

Danışman: Prof. Dr. Bora IŞILDAK

ÖZET

This project investigates the application of deep learning techniques for calibrating quark jets in particle physics experiments, particularly in the context of high-energy experiments like the Large Hadron Collider (LHC). Traditional quark jet calibration viii methods are complex and prone to error, while deep learning algorithms offer a more precise and efficient approach. By training artificial neural networks on jet images, this study aims to improve the accuracy of energy measurements of quark jets. The project uses convolutional neural networks (CNNs) to extract meaningful features from jet images, thus providing better energy corrections. The results show that the proposed deep learning model can accurately predict jet energy corrections, demonstrating promise for future applications in particle physics.

PARTICLE PHYSICS

This section outlines the basics of particle physics with a focus on **jet formation and calibration** in high-energy collisions.
Matter consists of atoms, which are made of electrons and a nucleus containing protons and neutrons. Protons and neutrons are composed of quarks—elementary particles that come in six types (flavors) and interact via the strong nuclear force. These quarks are key elements of the **Standard Model**, which also includes leptons and force-carrying bosons (e.g., photons, gluons, W/Z bosons).

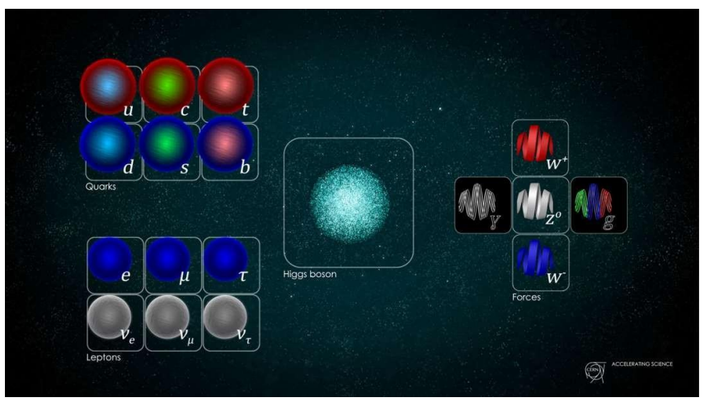

In proton-proton collisions at the LHC, quarks and gluons cannot be observed directly. Instead, they form **jets**, which are sprays of particles detected by systems like the **CMS detector**. Since the measured jet energy can differ from the true value, **jet energy corrections (JECs)** are necessary.

There are different types of jets:
RawJet: Uncorrected detector-level jet data
GenJet: Simulation-based jets representing true energy values
Jet images are created by simulating collisions and detector responses, then projecting energy deposits in η-ϕ space as 2D heatmaps. These images are used for training **deep learning models**, particularly **convolutional neural networks (CNNs)**, to improve energy correction accuracy.
The **LHC** is a 27 km circular accelerator at CERN that collides protons at near light-speed. The **CMS experiment**, a massive and highly precise detector, helps analyze the resulting particle interactions for insights into fundamental physics.

The Application Areas of Artificial Intelligence in Physics

This section explores how **Artificial Intelligence (AI)**—particularly **Machine Learning (ML)** and **Deep Learning (DL)**—is transforming physics research, especially in **high-energy experiments like those at CERN**.
ML allows systems to learn from data by optimizing predictions using loss functions and feedback loops. At **CERN**, ML is used to manage enormous datasets from the LHC, select relevant collision events, predict equipment failures, and enable autonomous robots to operate in high-radiation zones. Collaborative platforms like **CERN openlab** foster innovation in AI applications.
Several ML algorithms are used in physics, such as **neural networks, regression, clustering, decision trees, and random forests**, each suited to different problem types.
Deep learning extends ML with multi-layered neural networks capable of learning complex patterns. It powers tools like **CNNs**, which are highly effective for analyzing **jet images** by mimicking the human visual system's layered processing. Though often seen as "black boxes," DL models offer unmatched accuracy and scalability.

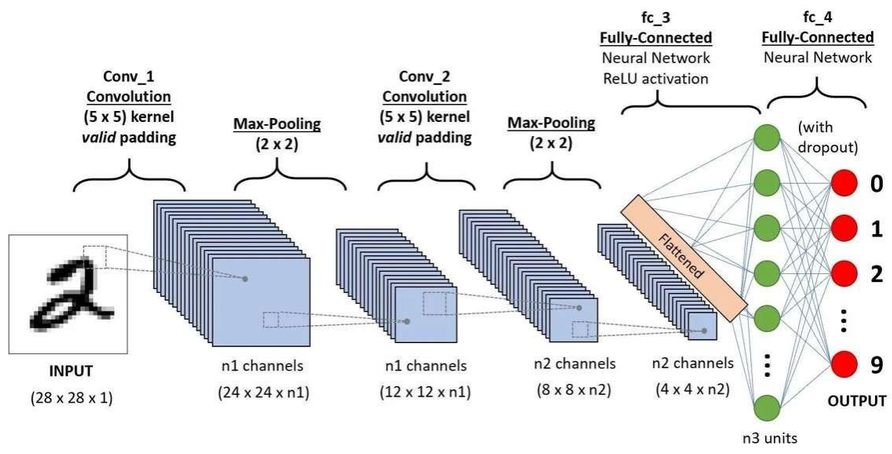

DATASET AND PROCESS

Dataset
The dataset used in this study, *JetNTuple_QCD_RunII_13TeV_MC*, originates from CERN's open data repository. It contains **1,000,000 jets** simulated from proton-proton collisions at 13 TeV using Pythia 8 and reconstructed with the **Particle Flow (PF)** algorithm and **anti-kt jet clustering**.
The following key parameters were selected from each jet:
JetPt: Transverse momentum of the jet
GenJetPt: True generator-level transverse momentum (reference)
JetRawPt: Raw transverse momentum before energy correction
PF: Particle Flow candidates
Flav: The flavor of the originating particle (e.g., quark or gluon)
These parameters were chosen because they are essential for comparing the reconstructed and true energies of the jets and for training the deep learning model to predict correction factors. The **jet flavor**, in particular, helps the model distinguish between different jet types (e.g., quark vs. gluon jets).

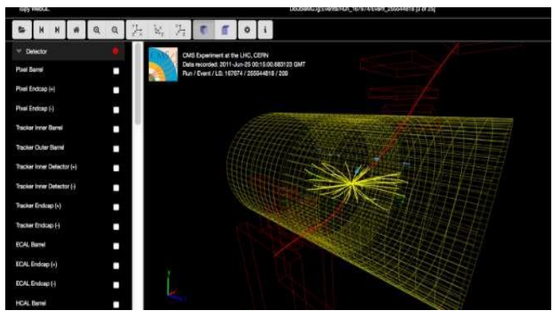

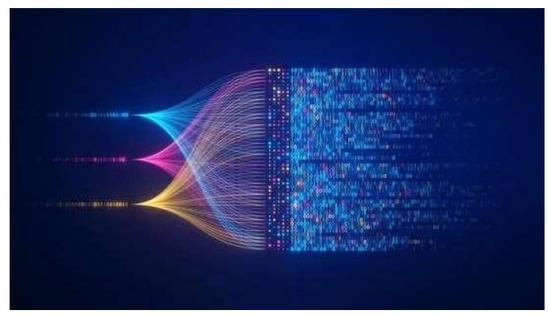

Process
The processing pipeline consists of several Python scripts designed to transform raw ROOT files into usable training data:
1. **Reading and Filtering Data**: ROOT files are parsed using the uproot library. Only branches containing the necessary parameters (JetPt, GenJetPt, etc.) are selected.
2. **Jet Image Generation**: For each jet, a 2D histogram is created in the η-φ space using PF object coordinates and pT values. These serve as input images for CNN models.
3. **Data Serialization**: The generated jet images and corresponding metadata are saved in **pickle format** for efficient loading and reuse.
4. **Model Training**: A **Convolutional Neural Network (CNN)** is constructed and trained using PyTorch to predict GenJetPt from image-based features. Techniques like **early stopping** and **CUDA acceleration** are used to improve performance.
5. **Evaluation**: The model's predictions are compared against GenJetPt values to calculate error metrics and validate its effectiveness.

RESULTS

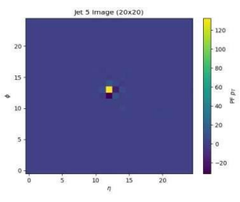

Jet 5 Parameters:
jetPt: 742.5511474609375
jetRawPt: 695.25830078125
genJetPt: 783.4083251953125
Flav: 1

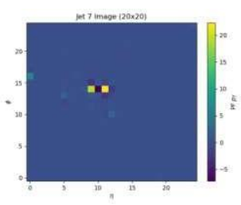

Jet 7 Parameters:
jetPt: 170.45286560058594
jetRawPt: 160.9000244140625
genJetPt: 148.7221221923828
Flav: 1

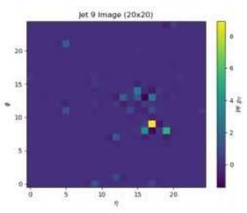

Jet 9 Parameters:
jetPt: 100.1641845703125
jetRawPt: 98.26861572265625
genJetPt: 104.32552337646484
Flav: 21

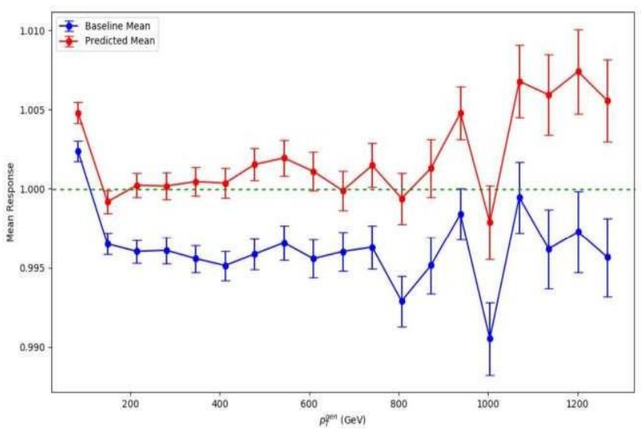

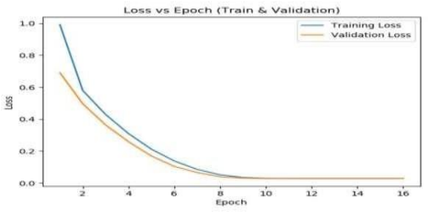

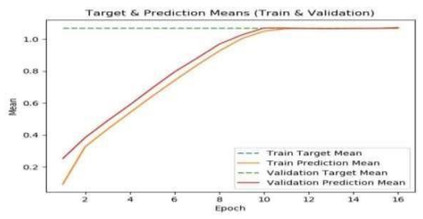

KAYNAKÇA

[1] https://cms.cern/news/jets-cms-and-determination-their-energy-scale
[2] https://home.cern/science/accelerators/large-hadron-collider
[3] https://iopscience.iop.org/article/10.1088/1742-6596/1085/2/022008/pdf

2024.-2025. Bahar Yarıyılı

FİZİK BÖLÜMÜ

4 Ocak 2011 ve 25 Ekim 2022 Kısmi Güneş Tutulmalarının İyonosferik Yanıtlar Açısından Karşılaştırmalı Analizi

Eslem Nur AKTAŞ 19022009

Danışman: Doç. Dr. Zehra CAN

ÖZET

Bu çalışma, Güneş tutulmalarının orta enlem iyonosferik yapısı üzerindeki etkilerini, güncel bilimsel ve teknolojik yaklaşımlar doğrultusunda değerlendirmeyi amaçlamaktadır. Literatürdeki pek çok araştırma, genellikle tek bir tutulma olayına ve sınırlı bir enlem aralığına odaklanmışken, bu çalışmada 4 Ocak 2011 ve 25 Ekim 2022 tarihlerinde meydana gelen iki farklı kısmi Güneş tutulması örneği üzerinden enlemsel farklılıklar sistematik olarak analiz edilmektedir. Tutulma öncesi ve sonrasındaki zaman dilimlerinde elde edilen iyonosferik parametrelerin ortalama değerleri kullanılarak, gözlenen anomalilerin jeomanyetik fırtınalar, atmosferik dalgalar ya da Güneş tutulmasının doğrudan etkisiyle mi ilişkili olduğu ayrıntılı şekilde değerlendirilecektir.

Giriş

Güneş tutulmaları, yalnızca görsel bir astronomik olay olmanın ötesinde, Güneş-Dünya sisteminin etkileşimlerini anlamak açısından eşsiz doğal laboratuvarlar sunar [1]. Güneş'ten gelen ultraviyole (UV) ve X-ışını radyasyonunun tutulma sırasında aniden kesintiye uğraması, iyonosferin iyonlaşma-denge süreçlerinde geçici ancak önemli bozulmalara yol açar [2,3].

Yöntem ve Veriler

İyonosferik veriler Global Ionosphere Radio Observatory (GIRO) ağına ait iyonosonda istasyonlarından, uzay havası verileri (Kp, Dst, AE, Ap, F10.7 cm) ise NASA OMNIWeb veritabanından temin edilmiştir.

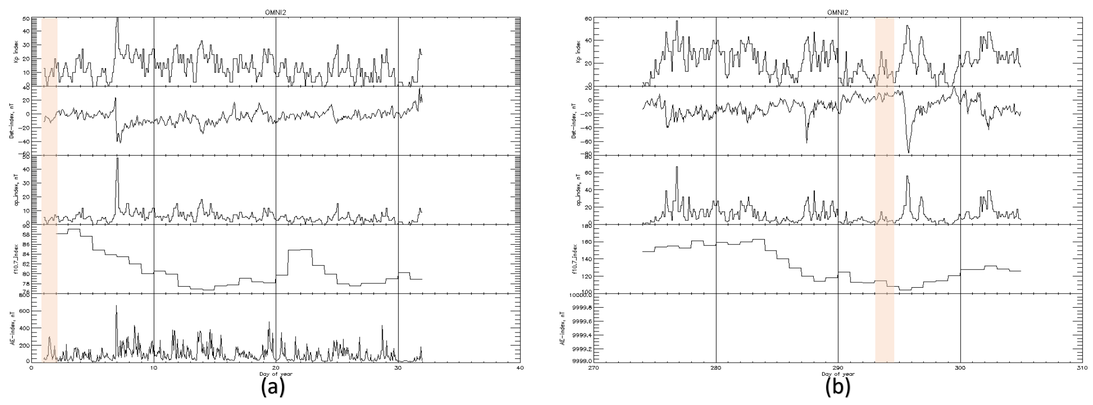

(a) (b)

Şekil 1. 4 Ocak 2011(a) ve 25 Ekim 2022(b) tarihlerinde gerçekleşen Güneş tutulmalarının jeomanyetik indislerinin değişim grafikleridir.

İstasyon Seçimi:

Tüm istasyonlar 35°–55° enlem bandı içinde ve tutulma hattı ile uyumlu konumda seçilmiştir.

- **2011 tutulması için:** Athens, Dourbes, Chilton, Roquetes, Elektrougli
- **2022 tutulması için:** Athens, Fairford, San Vito, Rome

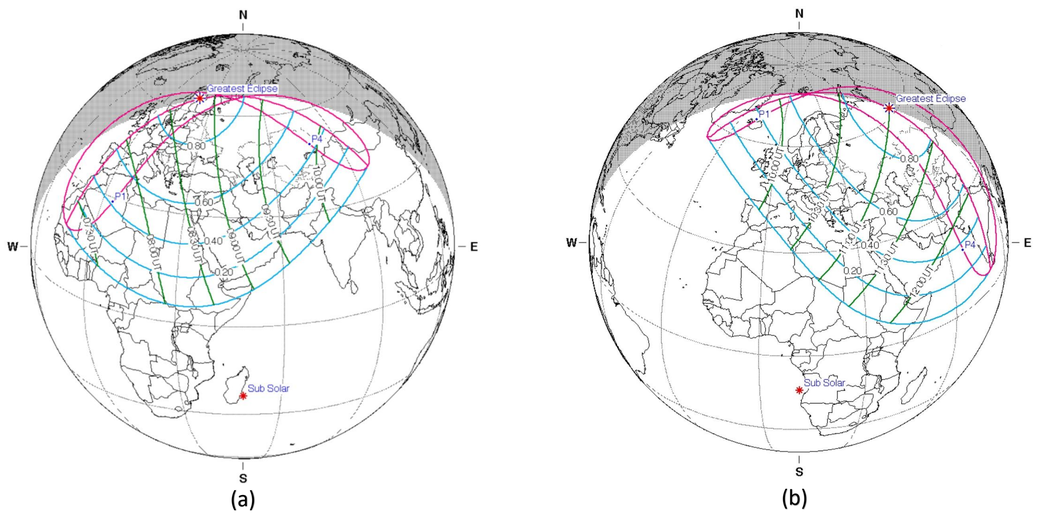

(a) (b)

Şekil 2. 4 Ocak 2011(a) ve 25 Ekim 2022(b) tarihlerinde gerçekleşen Güneş tutulmalarının https://eclipse.gsfc.nasa.gov/ sitesinden alınan haritalarıdır.

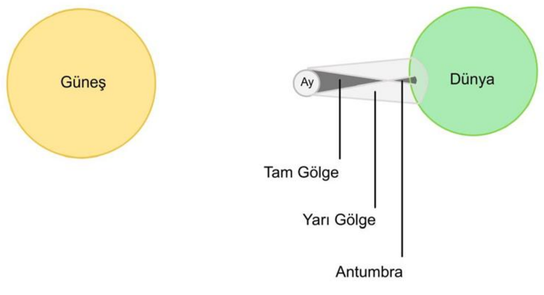

Şekil 3. Güneş Tutulmalarının gölge büyüklüğüne göre sınıflandırılmasının temsili bir görselidir.

İyonosferin foF2 (Kritik Frekans), hmF2 (Maksimum Yükseklik), TEC (Toplam Elektron İçeriği)

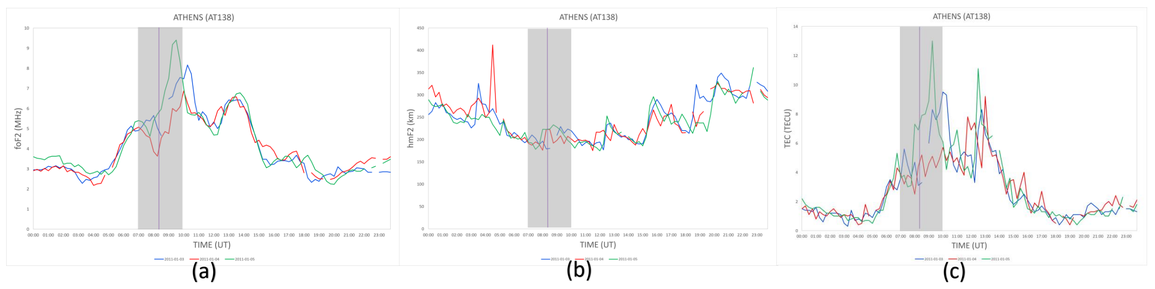

(a) (b) (c)

Şekil 4. 4 Ocak 2011 tarihli AT138 istasyonuna ait foF2 (a), hmF2 (b) ve TEC (c) değişimleri gösterilmektedir.

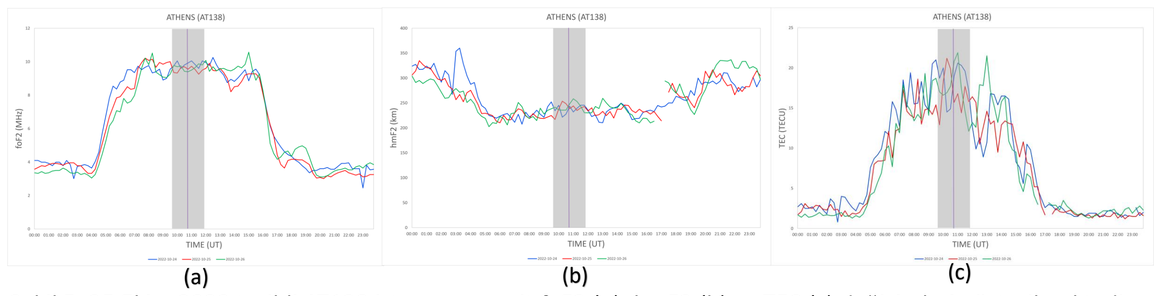

(a) (b) (c)

Şekil 5. 25 Ekim 2022 tarihli AT138 istasyonuna ait foF2 (a), hmF2 (b) ve TEC (c) değişimleri gösterilmektedir.

Tablo1. Seçilen iki istasyon için iyonosferik parametrelerin davranış bilgileridir.

İstasyon	Ülke	Tarih	Tutulma Büyüklüğü	Maksimum Evre (LT)	foF2 Değişimi		hmF2 Değişimi		TEC Değişimi	
ATHENS	Yunanistan	04.01.2011	0,6747	10:23:33	↓	↓	↓	↓	↓	↓
DOURBES	Belçika	04.01.2011	0,7627	09:14:35	↓	↓	↑	↑	↓	↓
CHILTON	Birleşik Krallık	04.01.2011	0,748	08:11:45	↓	↓	↓	↑	↓	↑
ROQUETES	İspanya	04.01.2011	0,6331	08:57:48	↓	↓	↑	↑	↓	↓
ELEKTROUGLI	Rusya	04.01.2011	0,8124	10:03:48	↓	↓	↑	↑	↓	↓
ATHENS	Yunanistan	25.10.2022	0,3778	12:43:58	↓	↓	↓	↓	↓	↓
FAIRFORD	Birleşik Krallık	25.10.2022	0,2593	09:59:12	↓	↓	↓	↓	↓	↓
SAN VITO	Arnavutluk	25.10.2022	0,3673	12:33:06	↓	↓	↑	↓	↓	↓
ROME	İtalya	25.10.2022	0,265	12:21:44	↓	↑	↓	↓	↓	↓

Mavi Oklar (↓↑): Tutulma gününde, bir gün öncesine göre meydana gelen değişimi göstermektedir.
Yeşil Oklar (↓↑): Tutulma gününde, bir gün sonrasına kıyasla gözlemlenen değişimi temsil etmektedir.

Sonuç ve Tartışma

Elde edilen bulgular, Güneş tutulmalarının iyonosfer üzerindeki etkilerinin yalnızca geometrik örtülme oranı ile değil; aynı zamanda gözlem konumunun enlemi, yerel saat, güneş aktivite döngüsünün fazı ve uzay havası durumu gibi faktörlere de yüksek duyarlılık gösterdiğini ortaya koymaktadır.

KAYNAKÇA

[1] Chen, G., Qi, H., Ning, B., Zhao, Z., Yao, M., Deng, Z., ... & Wu, C. (2013). Nighttime ionospheric enhancements induced by the occurrence of an evening solar eclipse. Journal of Geophysical Research: Space Physics, 118(10), 6588-6596.

[2] Verhulst, T. G., Sapundjiev, D., & Stankov, S. M. (2016). High-resolution ionospheric observations and modeling over Belgium during the solar eclipse of 20 March 2015 including first results of ionospheric tilt and plasma drift measurements. Advances in Space Research, 57(11), 2407-2419.

[3] Jakowski, N., Wehrenpfennig, A., Heise, S., Schlueter, S., & Noack, T. (2001, December). Space weather effects in the ionosphere and their impact on positioning. In ESA workshop paper

2024-2025 Spring Semester Department of Physics

Investigating Strangeness Enhancement with Multiplicity in pp Collision Using Angular Correlation

Barış GÜLŞEN 19022002

Advisor: Prof. Dr. Ayben KARASU UYSAL

Abstract

This study investigates the production of strange hadrons in pp collisions at $\sqrt{s}$ = 5.02 and 13 TeV using angular correlations in ALICE at the LHC. Correlations between high-momentum trigger particles and both K_S^0 and $\Xi^{\pm}$ show that strange particle yields, especially $\Xi^{\pm}$, increase with event multiplicity. The enhanced transverse-to-leading yields suggest notable underlying event contributions and possible collective effects in high-multiplicity pp collisions [1].

Introduction

Strangeness enhancement, long viewed as a hallmark of quark-gluon plasma (QGP) in heavy-ion collisions, has also emerged in high-multiplicity pp collisions, raising questions about its origin [2, 3]. This study investigates the angular distribution of strange hadrons K_S^0, $\Xi^{\pm}$ relative to high-p_T trigger particles to explore possible collective effects and disentangle soft and hard quantum chromodynamics (QCD) contributions.

Methodology

The study utilizes ALICE pp collision data at center-of-mass energies of $\sqrt{s}$ = 5.02 and 13 TeV. Strange hadrons, such as K_S^0 and $\Xi^{\pm}$, are identified through their characteristic decay topologies and correlated with high-momentum trigger particles (p_T > 3 GeV/c). The analysis focuses on two distinct regions defined by the azimuthal angle difference ($\Delta\phi$) between the trigger and associated particles:

- **Toward-leading region**: Aligned with the trigger particle, primarily reflecting jet fragmentation processes.
- **Transverse-to-leading region**: Perpendicular to the trigger, dominated by contributions from the underlying event.

Detector effects, including efficiency and acceptance, are systematically corrected, and particle yields are examined across various multiplicity classes. Figure 1 demonstrates the angular correlation analysis steps for K_S^0, while Figure 2 presents the corresponding procedure for $\Xi^{\pm}$ baryons.

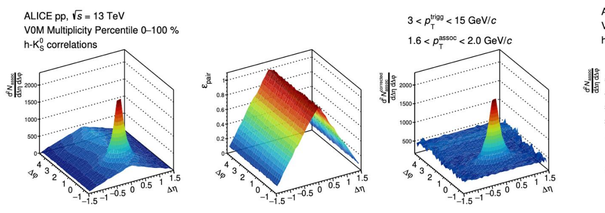

Figure 1. (left) Example of angular correlation distribution. (center) Acceptance correction of trigger- K_S^0 pairs. (right) Angular correlation distribution divided by the pair acceptance.

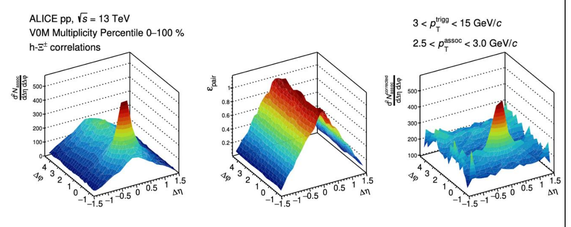

Figure 2. (left) Example of angular correlation distribution. (center) Acceptance correction of trigger- $\Xi^{\pm}$ pairs. (right) Angular correlation distribution divided by the pair acceptance

Results

The transverse-to-leading region shows stronger multiplicity-dependent enhancement than toward-leading, particularly for multi-strange $\Xi^{\pm}$. The increasing $\Xi^{\pm}$ / K_S^0 ratio with multiplicity suggests soft processes dominate multi-strange baryon production [1]. Notably, collision energy ($\sqrt{s}$ = 5.02 vs 13 TeV) shows negligible effect compared to event multiplicity.

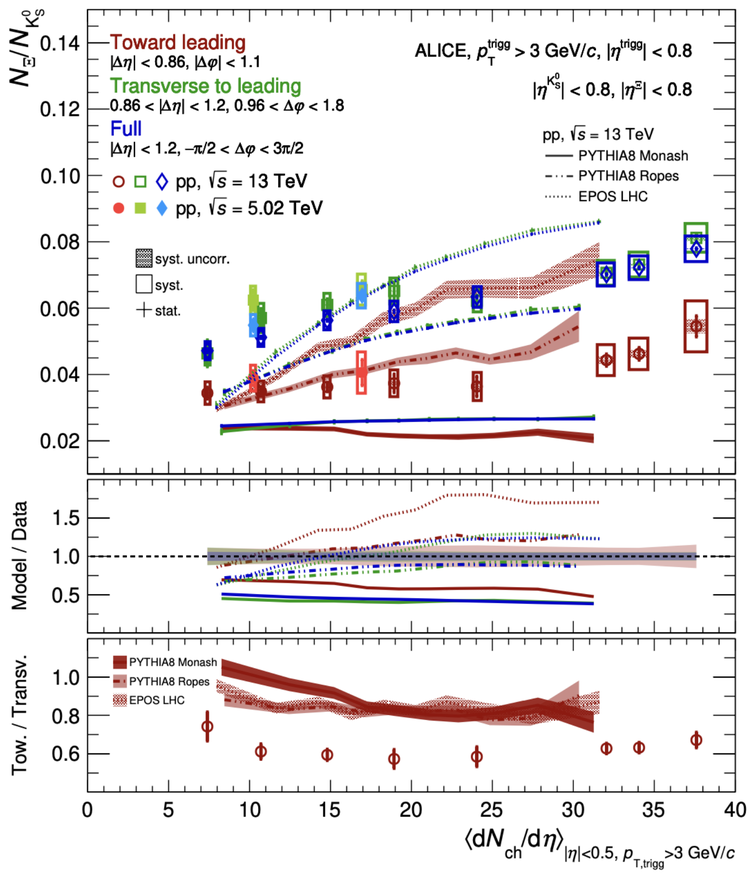

Figure 3. Top panel: full (blue), transverse-to-leading (green), and toward-leading (red) $\Xi^{\pm}$ / K_S^0 yield ratios as a function of the charged-particle multiplicity measured at midrapidity in events with a trigger particle. Central panel: ratio between the model predictions. Bottom panel: double ratio between the toward-leading and the transverse-to-leading $\Xi^{\pm}$ / K_S^0 ratios.

Model Comparison

This study compared strangeness enhancement in high-multiplicity pp collisions across three theoretical models: PYTHIA8 Monash tune, PYTHIA8 color ropes, and EPOS LHC. The standard PYTHIA8 Monash tune underestimated K_S^0 and $\Xi^{\pm}$ yields by up to 70% across all multiplicity ranges, while the color rope variant improved predictions but still showed 50% deviation at low multiplicity and 20% at high multiplicity. EPOS LHC underestimated yields at low multiplicity but overestimated by 20% at high multiplicities. Crucially, none of the models could explain the observed 40% higher $\Xi^{\pm}$ / K_S^0 ratio in transverse regions compared to toward-leading directions [1].

These discrepancies highlight gaps in current theoretical descriptions of strangeness production, particularly regarding collective effects and multi-parton interactions in small collision systems. Future models should better incorporate these dynamics to explain the observed enhancement patterns, which may signal QGP-like behavior even in pp collisions. The comparison between the theoretical models is presented in Figure 4.

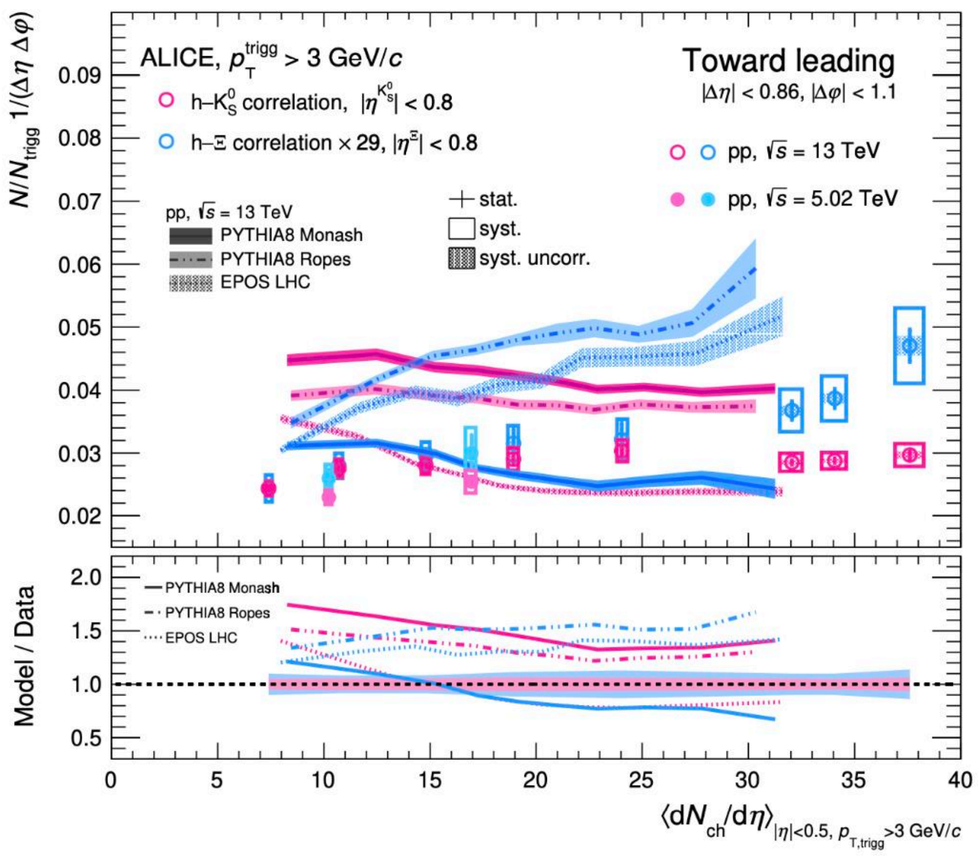

Figure 4. Upper panel: toward-leading K_S^0 (magenta) and $\Xi^{\pm}$ (light blue) yields per unit $\Delta\eta\Delta\phi$ area as a function of the charged-particle multiplicity measured in events with a trigger particle. Bottom panel: ratio between the model predictions.

Conclusion

This analysis demonstrates a clear multiplicity-dependent enhancement in strange hadron production, with stronger effects observed in regions sensitive to the underlying event. The results imply that not only hard scattering but also soft QCD processes play a crucial role in strangeness enhancement. The similarities with phenomena seen in heavy-ion collisions raise the possibility of collective behavior in pp collisions, challenging the traditional understanding of QGP formation. These findings underscore the need for precision measurements in small systems to disentangle the contributions of various QCD mechanisms. High-statistics data, especially with improved particle identification and differential analyses, will be critical in constraining theoretical models. Moreover, future studies involving correlations and flow observables could provide deeper insight into potential collective effects. Cross-comparisons with p–Pb and Pb–Pb systems may also help clarify the onset of QGP-like behavior. Overall, this analysis highlights the evolving landscape of high-energy physics, where even the smallest systems reveal unexpectedly rich dynamics [1].

References

[1] Shreyasi Acharya et al. Investigating strangeness enhancement with multiplicity in pp collisions using angular correlations. JHEP, 09:204, 2024.

[2] Jaroslav Adam et al. Enhanced production of multi-strange hadrons in high-multiplicity proton-proton collisions. Nature Phys., 13:535–539, 2017.

[3] Shreyasi Acharya et al. Multiplicity dependence of π, K, and p production in pp collisions at $\sqrt{s}$ =13 TeV. Eur. Phys. J. C, 80(8):693, 2020.

YTÜ FEN EDEBİYAT FAKÜLTESİ

2024-2025 Spring Semester PHYSICS DEPARTMANT

Numerical Analysis of the MRK348 Spektrum by Extracting Data from a Visual Image Using Python

Eylül Deniz DURMAZ 20022038

Res. Asst. Dr.Muhammed Kıyami ERDİM

ABSTRACT

This study proposes a Python-based method to digitize and analyze the spectrum image of galaxy MRK348. It focuses on color models, data extraction using loops, Gaussian modeling, and the importance of FWHM in spectral analysis. The study also outlines challenges and solutions during the process.

STATEMENT OF THE PROBLEM

The galaxy examined in this study lacks spectral data; only image of the data is available. The inaccessibility of spectroscopic information significantly limits the scope of research that can be conducted on this galaxy.

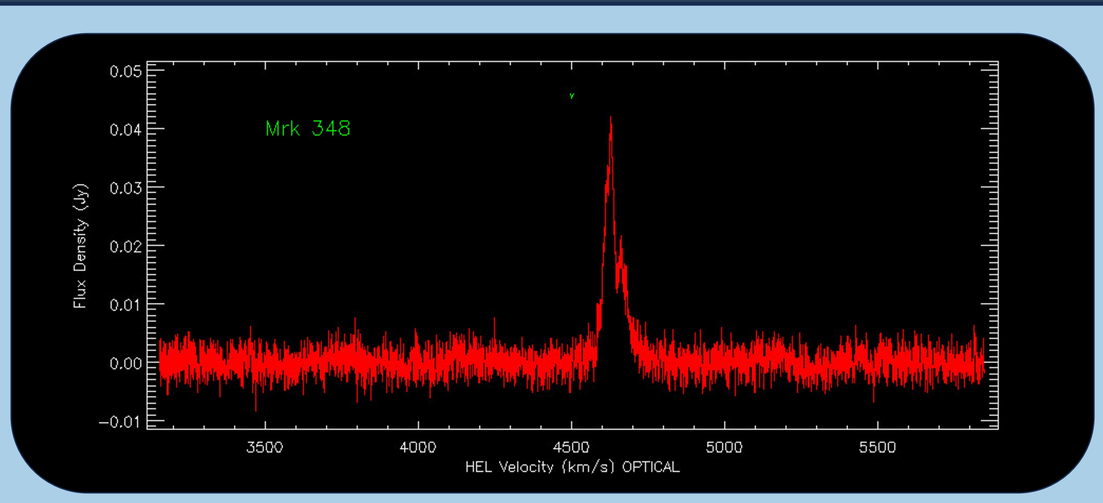

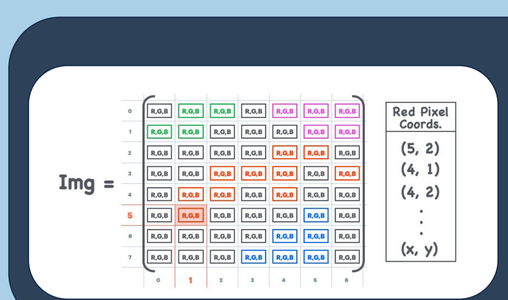

A study was conducted to understand through a matrix structure. the concept of pixels, which is essential for applying image processing methods. It was examined how all colors are composed of color codes and how an image is essentially formed

We focus on red pixels, defined in HSV as having hue between 0–10 or 350–360, with high saturation and brightness. A for loop checks all pixels, and red ones are saved in data_x and data_y.

Image coordinates start at the top-left, while graphical coordinates start at the bottom-left. To match the mathematical system, we store height - y instead of y.

This ensures the data is accurate for analysis.

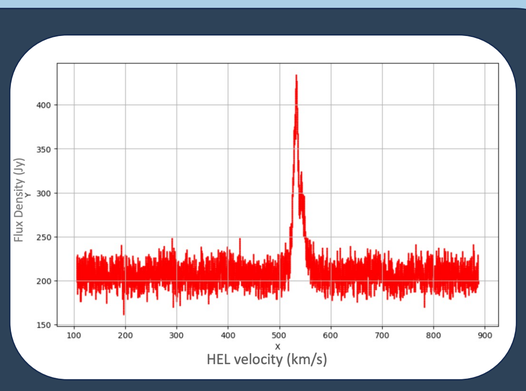

The Gaussian equation is defined using the parameters x, mu, and sigma. By applying this known equation together with the spectrum model, a consistent FWHM value can be obtained. Here, mu represents the peak position, while sigma is the standard deviation. The relationship between FWHM and sigma is well-established for the Gaussian distribution:

The known Gaussian equation and the FWHM formula involving sigma were implemented in Python. The code automatically executes all the described steps, processes the function, and calculates the FWHM value.

$$f(x,\mu,\sigma) = \frac{1}{\sigma\sqrt{2\pi}} e^{\frac{-(x-\mu)^2}{2\sigma^2}}$$

$$FWHM = 2\sqrt{2ln2}.\,\sigma \approx 2.35482.\,\sigma$$

Digital images are composed of pixels, each containing numerical values for red, green, and blue (RGB) components, typically ranging from 0 to 255. Understanding this pixel-based structure is essential for accurate image data extraction, as each pixel encodes color information through RGB intensity values. This numerical representation allows modern technology to interpret and process colors effectively.

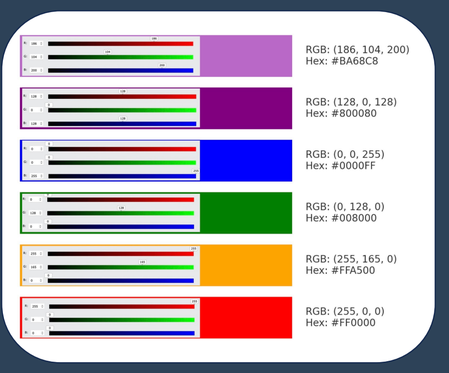

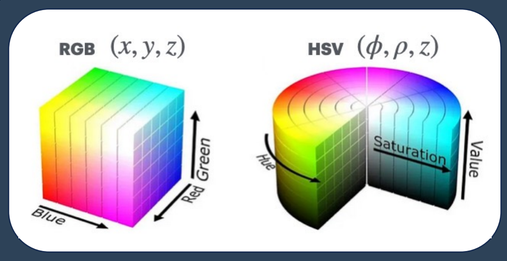

The HSV (Hue, Saturation, Value) model offers a more intuitive approach to color representation, as it aligns more closely with human color perception. Compared to RGB, HSV simplifies color selection and object extraction in images. The transformation involves normalizing RGB values and converting them to HSV components. This model enables more precise data extraction by allowing easier identification of desired colors and objects.

The (x, y) data is used to create a scatter plot, and a suitable model is selected. The MRK348 spectrum includes both a Gaussian-shaped peak and a linear background. Therefore, the data contains two separate physical components:

- **Linear model:** Represents background and environmental effects
- **Gaussian model:** Represents the actual signal (such as light or energy)

Explaining both with a single model leads to incorrect results. For accurate analysis, **these two components must be modeled separately**. This allows for a clearer understanding of the data.

In this way, a system was formed in which the known Gaussian equation can be used to determine the unknowns, mu and sigma. Sigma will directly help in calculating the FWHM value.

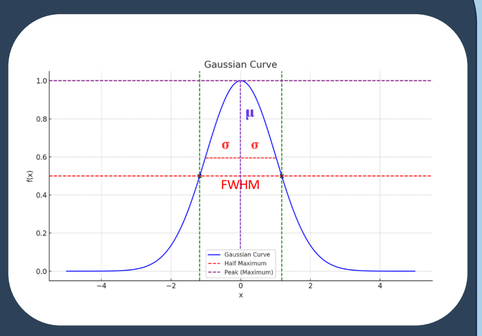

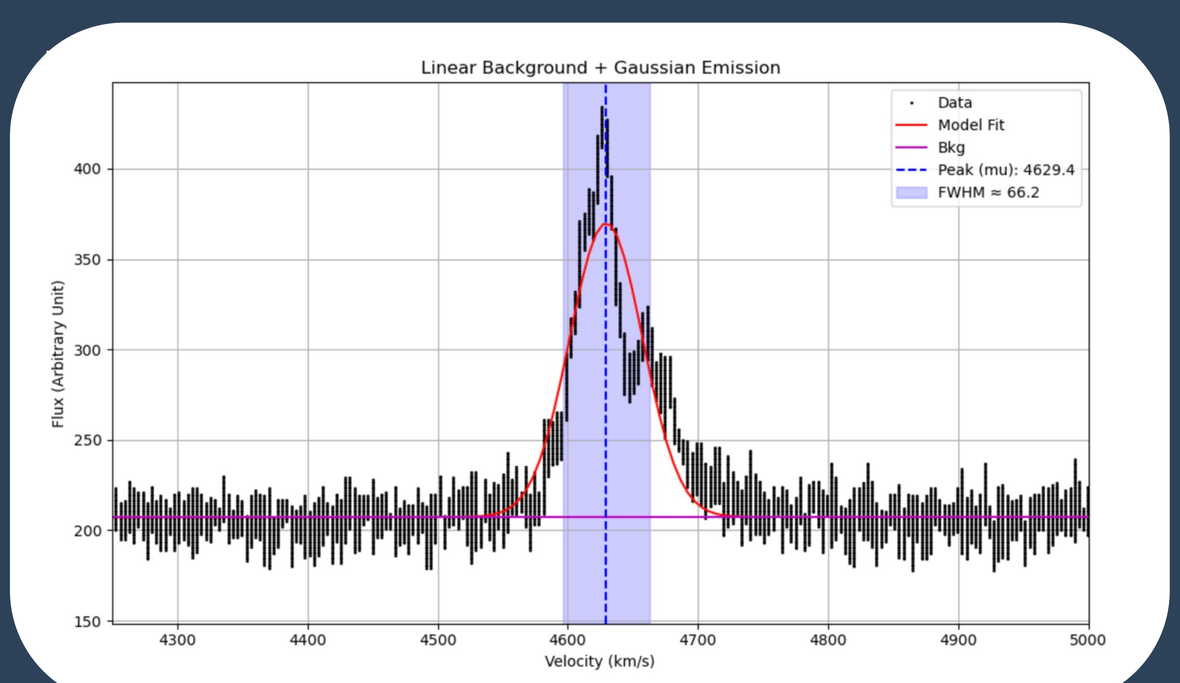

In this project, image processing, data modeling, and finally astrophysics were carried out step by step. First, precise analyses were performed on images received from space to identify the coordinates of red pixels and convert them into numerical data. Then, meaningful results were obtained by applying appropriate mathematical models to this data. This entire process represents the fundamental steps to extract knowledge that reveals the secrets of the universe from complex data sets.

Astrophysics is the fascinating final stage of this process. Thanks to the given equations, the outputs obtained from the image processing and modeling steps were connected into a consistent conclusion in this study. It means deciphering the language of light coming from the depths of space and understanding the mysteries of galaxies, stars, and cosmic events. Each peak in a spectrum reflects physical phenomena in the universe; through this, temperatures, motions, chemical compositions, and much more can be discovered. Astrophysics is not only about interpreting data; it is also about satisfying humanity's curiosity about how the universe works, illuminating the unknown, and embarking on an awe-inspiring journey. This project has thus become a bridge that opens the doors to that very wonder.

[1] Pauli Virtanen, Ralf Gommers, Travis E. Oliphant, Matt Haberland, Tyler Reddy, David Cournapeau, Evgeni Burovski, Pearu Peterson, Warren Weckesser, Jonathan Bright, Stéfan J. van der Walt, Matthew Brett, Joshua Wilson, K. Jarrod Millman, Nikolay Mayorov, Andrew R. J. Nelson, Eric Jones, Robert Kern, Eric Larson, CJ Carey, İlhan Polat, Yu Feng, Eric W. Moore, Jake VanderPlas, Denis Laxalde, Josef Perktold, Robert Cimrman, Ian Henriksen, E.A. Quintero, Charles R Harris, Anne M. Archibald, Antônio H. Ribeiro, Fabian Pedregosa, Paul van Mulbregt, and SciPy 1.0 Contributors. (2020) SciPy 1.0: Fundamental Algorithms for Scientific Computing in Python. Nature Methods, 17(3), 261-272. DOI: 10.1038/s41592-019-0686-2.

[2] **Montgomery, D. C., Peck, E. A., & Vining, G. G.** (2012). *Introduction to linear regression analysis* (5th ed.). John Wiley & Sons.

[3] **Cantrell, C. A.** (2008). *Technical note: Review of methods for linear least-squares fitting of data and application to atmospheric chemistry problems. Atmospheric Chemistry and Physics*, 8, 5477–5487. https://doi.org/10.5194/acp-8-5477-2008

[4] **Riffel, R. A., Dors, O. L., Armah, M., Storchi-Bergmann, T., Feltre, A., Hägele, G. F., Cardaci, M. V., Ruschel-Dutra, D., Krabbe, A. C., Pérez-Montero, E., Zakamska, N. L., & Freitas, I. C.** (2020, December 3). Chemical abundances in Seyfert galaxies – V. The discovery of shocked emission outside the AGN ionization axis. *arXiv preprint 2012.02013*.

[5] **Falcke, H., Henkel, C., Peck, A. B., Hagiwara, Y., Prieto, M. A., & Gallimore, J. F.** (2000, April 27). Discovery of a very luminous megamaser during a radio flare in the Seyfert 2 galaxy Mrk 348. *arXiv preprint astro-ph/0004368*.

[6] **Kutner, M. H., Nachtsheim, C. J., Neter, J., & Li, W.**
Applied Linear Statistical Models
McGraw-Hill, 5th Edition, 2004.

2024-2025 SPRING SEMESTER

PHYSICS DEPARTMENT

EXPLORING THE SHOCKLEY-QUEISSER EFFICIENCY LIMIT FOR SOLAR CELLS

İclal Buse DURMUŞ 20022047

Supervisor: Assoc. Prof. Fatma Pınar CHOI

ABSTRACT

The working principles of solar cells, efficiency parameters and physical mechanisms limiting this efficiency have been examined in detail. Theoretical limits based on the Shockley–Queisser limit have been evaluated, and current approaches such as tandem structures, quantum dots and perovskite materials to overcome this limit have been discussed. The analyses reveal the potential of new generation photovoltaic technologies that can go beyond classical limits.

RENEWABLE ENERGY SOURCES AND SOLAR ENERGY

The increasing energy demand and environmental damage of fossil fuels have increased the tendency towards renewable resources. Solar energy reaches the Earth with the radiation generated by nuclear fusion and is a clean, sustainable energy source. The Sun acts like a black body and the radiation it emits is absorbed, scattered and reflected in the atmosphere. This energy can be converted into electricity with photovoltaic cells and into heat with thermal systems. Using solar energy effectively plays an important role in combating climate change by reducing greenhouse gas emissions.

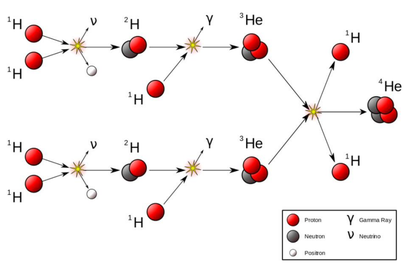

Figure 1: Nuclear Fusion [4]

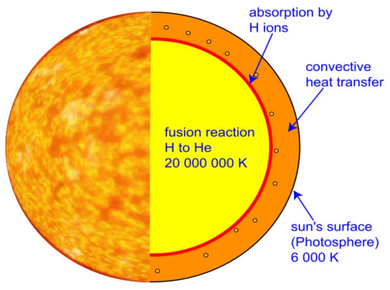

Figure 2: Fusion Reaction in Sun [5]

HISTORY AND FUNDAMENTALS OF SOLAR CELLS

In 1839, Becquerel discovered that electric current was produced by metal plates illuminated with light, laying the foundation for the photovoltaic effect. Advances that began with the silicon solar cell developed in 1954 enabled solar energy to become widespread in daily life from the 1980s onwards.

Working Principle of Solar Cells and Solar Cell Parameters

Solar cells, also known as photovoltaic (PV) cells, convert sunlight directly into electricity through the photovoltaic effect. When photons from sunlight strike the surface of a solar cell, they transfer their energy to electrons in the semiconductor material (typically silicon). This energy excites electrons, freeing them from their atomic bonds and allowing them to flow through the material. This flow of electrons constitutes an electric current.

A typical solar cell is composed of a p-n junction diode. The p-type (positive) side contains an excess of holes (missing electrons), while the n-type (negative) side contains an excess of free electrons. When sunlight hits the junction, electron-hole pairs are generated. The built-in electric field at the junction drives electrons to the n-side and holes to the p-side, creating a voltage difference. When the cell is connected to an external load, this voltage causes a current to flow, generating electrical power.

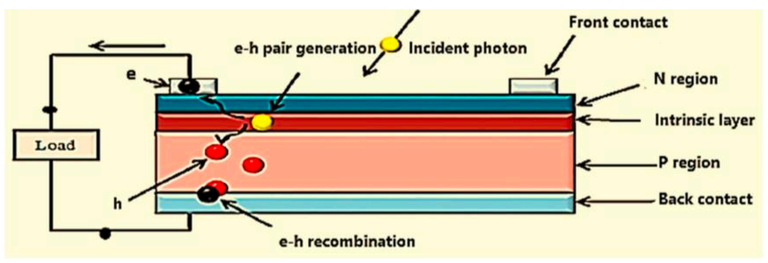

Figure 3: Solar Cells Structure [1]

Solar Cell Parameters

Short Circuit Current (J_{SC})

It is the maximum current measured when the terminals of the solar cell are short-circuited (V = 0). It depends on the amount of incident light and the surface area. Current density in generalized form:

$$J_{SC} = \frac{I_{SC}}{A}$$

Open Circuit Current (V_{OC})

The maximum voltage measured when the circuit is open (I = 0). It depends on the type of material and temperature. It is usually between 0.5-0.6 V.

Fill Factor (FF)

Indicates the ability of the solar cell to generate maximum power. It is calculated as follows:

$$FF = \frac{I_{max} \cdot V_{max}}{I_{SC} \cdot V_{OC}}$$

SHOCKLEY-QUEISSER LIMIT

The Shockley-Queisser limit defines the maximum theoretical efficiency that single-pass p-n junction solar cells can achieve. This limit is based on an ideal case where there is only radiative recombination and the incident light is modeled as a blackbody. The calculations include fundamental losses such as thermalization, spectral losses and electron-hole recombinations. According to this approach, the maximum efficiency of a 1.1 eV bandgap solar cell is about 33%. In real cells, the efficiency remains below this value, mainly due to non-radiative losses.

Shockley-Queisser theory is based on the detailed balance principle and determines the maximum efficiency of a single p-n junction solar cell under ideal conditions. Basic parameters:

Sun temperature:

$$kT_s = qV_s$$

Temperature of the solar cell:

$$kT_c = qV_c$$

Band gap:

$$E_g = h\nu_g = qV_g$$

Total photon flux from the sun (according to Planck's law):

$$Q_s = \int_{\nu_g}^{\infty} \frac{2\pi}{c^2} \cdot \frac{\nu^2}{e^{h\nu/kT_s - 1}} d\nu$$

Converted to dimensionless form:

$$Q_s = \left(\frac{2\pi(kT_s)^3}{h^3 c^2}\right) \int_{x_g}^{\infty} \frac{x^2}{e^{x-1}} dx$$

The total energy of all photons coming from the sun is given by the formula:

$$P_{in} = \left(\frac{2\pi(kT_s)^4}{h^3.c^2}\right) \int_0^{\infty} \frac{x^3}{e^{x-1}} dx$$

here the result of the integral is a known constant. Therefore:

$$P_{in} = \frac{2\pi^5(kT_s)^4}{15h^3c^2}$$

it can be defined as.

Each absorbed photon contributes only as much energy as $E_g = hV_g$. Therefore, we can calculate the electrical output power as follows:

$$P_{out} = E_g . Q_s = h\nu_g . Q_s$$

Ultimate efficiency is found by comparing these two power equations (P_{in} and P_{out}) to each other.

$$u(x_g) = \frac{P_{out}}{P_{in}} = \frac{h\nu_g . Q_s}{P_{in}}$$

Converting to dimensionless form:

$$u(x_g) = \frac{x_g . \int_{x_g}^{\infty} \frac{x^2}{e^{x-1}} dx}{\int_0^{\infty} \frac{x^3}{e^{x-1}} dx} = \frac{15 x_g}{\pi^4} \int_{x_g}^{\infty} \frac{x^2}{e^{x-1}} dx$$

it is expressed as.

As a result of all these calculations, it was seen that the maximum efficiency could be approximately *44%*, as in Figure 3.2. This requires the x_g parameter to be approximately *2.2* and the band gap of the semiconductor to be *1.1 eV.*

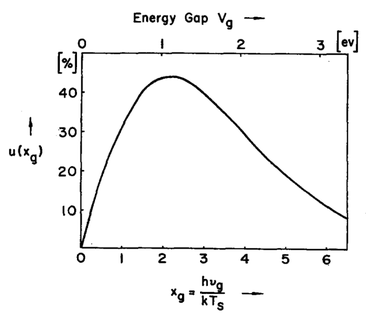

Figure 4: Ultimate Efficiency [2]

Photon emission as the single-pass Cell operates at ambient temperature. The limited solid angle of the sun is also taken into account.

Solid angle of the sun:

$$\omega_s = \frac{\pi\left(\frac{D}{L}\right)^2}{4} = \frac{\pi\left(\frac{1.39}{149}\right)^2}{4} = 6.85 \times 10^{-5} sr$$

Geometric factor for planar cells:

$$f_w = \frac{\omega_s}{\pi} = 2.18 \times 10^{-5}$$

it is associated with.

Recombination rate increases with applied voltage, net current becomes:

$$I = q\left(F_s - F_c(V)\right) = I_{ph} - I_0 e^{\frac{qV}{kT}}$$

Open circuit voltage (V_{OC}):

$$V_{OC} = \frac{kT_c}{q} \ln\left(\frac{J_{SC}}{J_0} + 1\right)$$

is given in the form.

The limit is reached at Eg = 1.34 eV. Crystalline Si cells achieve ~80–85% of the limit (~26%), while GaAs cells reach ~90% (~29%). This limit applies only to single-junction solar cells; multi-junction devices can surpass it.

RECENT STUDIES TO OVERCOME THE SHOCKLEY-QUEISSER LIMIT

The Shockley–Queisser limit sets the maximum efficiency of single-junction solar cells at 33.7%. To surpass this, tandem cells combining materials with different band gaps have been developed for better spectral utilization. Recent studies also explore quantum dot and perovskite integrations.

Tandem cells stack sub-cells with different band gaps to absorb a broader spectrum and reduce losses.

2-Terminal (2T – Monolithic): Cells are connected in series, sharing the same current. Current matching is mandatory; the lowest current limits the entire system. Electrical contact is provided by the tunnel junction layer. Efficiency is ~42–45%. In 2024, LONGi achieved 34.6% efficiency with a perovskite–Si 2T cell.

3-Terminal (3T): One of the three terminals is common. Cells cannot operate independently but have separate IV characteristics. No current matching is required. Efficiency is ~38–42%. 27.1% efficiency was achieved with perovskite–Si–perovskite structure in Singapore in 2024.

4-Terminal (4T - Mechanically Stacked): Each cell operates separately, has two independent circuits. No current and voltage matching is required. The highest theoretical efficiency (~44-46%) is achieved in this structure. Solliance reported 30.1% efficiency in 2022 and 29.36% efficiency in China in 2025.

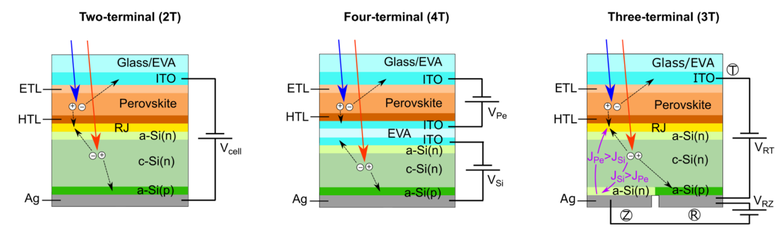

Figure 5: Tandem Cells Structure [8]

Quantum Dots and Perovskites

Quantum dots (QDs) are nanoscale semiconductors with size-dependent band gaps, enabling broad light absorption. They offer advantages like flexible design, easy processing, and multiple exciton generation (MEG). However, stability issues and toxic materials (Cd, Pb) are major drawbacks. QDs are used in sensitized, all-QD, and tandem solar cells, reaching up to 18% efficiency with perovskite combinations.

Quantum Dot Sensitized Solar Cells: QDs replace organic dyes and transfer electrons to materials like TiO_2. MEG allows more than one exciton per photon, improving efficiency.

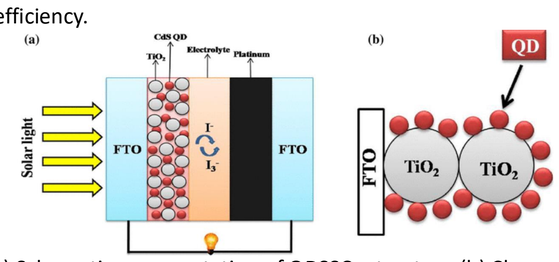

Figure 6: (a) Schematic representation of QDSSCs structure (b) Close up of the TiO_2 structured semiconductor skeleton [9]

All Quantum Dot Solar Cells (All QD SCs): In All-QD solar cells, both light absorption and charge transport rely entirely on QDs like PbS or PbSe, which absorb well in the near-IR region.

Quantum Dot-Based Tandem Cells: Quantum dots (QDs) are integrated into tandem cells—especially with perovskites—to absorb a broader light spectrum. Materials like PbS, CdSe, and InP are commonly used. QDs improve efficiency by enhancing charge transport (ETL/HTL layers), broadening absorption in active layers, and enabling vertical stacking (visible light by perovskites, NIR by QDs). They also serve as buffer layers and protective coatings, boosting stability by up to 40%.

RESULTS AND DISCUSSION

This study examines the ~33.7% efficiency limit of single-junction solar cells (Shockley–Queisser limit) and ways to overcome it. Key losses include radiative recombination, thermalization, and spectral losses.

Tandem cells, quantum dots, and perovskites offer promising solutions, reaching up to 42–46% efficiency. Yet, issues like material stability, current matching, and scalability remain. The Shockley–Queisser limit still serves as a key reference for future innovations in nanostructured and quantum-enhanced solar technologies.

REFERENCES

[1] Al-Ezzi et all. (2022). Photovoltaic solar cells: a review. *Applied System Innovation*, *5*(4), 67.
[2] Shockley, W. & Queisser (2018). Detailed balance limit of efficiency of p–n junction solar cells. In *Renewable energy* (35,54).
[3] Ekimov, A. I. (2023). Quantum size effect in three-dimensional microscopic semiconductor crystals. *JETP Letters*, *118*, p.15-S17.
[4] https://euro-fusion.org/fusion/fusion-on-the-sun/
[5] https://www.pveducation.org/pvcdrom/properties-of-sunlight/the-sun
[6] Al-Ezzi et all. (2022). Photovoltaic solar cells: a review. *Applied System Innovation*, *5*(4), 67.
[7] Shockley, W. (2018). Detailed balance limit of efficiency of p–n junction solar cells. In *Renewable energy* (35,54).
[8] https://www.lti.kit.edu/english/9048.php
[9] Veerathangam, K., Muthu Senthil Pandian, and P. Ramasamy. "Influence of SILAR deposition cycles in CdS quantum dot-sensitized solar cells." Journal of Materials Science: Materials in Electronics 29 (2018): 7318-7324.

FİZİK BÖLÜMÜ

PYTHON DESTEKLİ BİR ELEKTRİK ALAN SİMÜLASYONUNUN HTML/JavaScript ORTAMINDA GELİŞTİRİLMESİ VE EĞİTİMDE UYGULANABİLİRLİĞİNİN İNCELENMESİ

Sinem DURSUNKAYA - 19022082

Danışman: Prof.Dr.Önder YARGI

ÖZET

Bu bitirme projesi, elektrik alan kavramını daha anlaşılır ve etkileşimli şekilde öğretmeyi amaçlayan bir web tabanlı simülasyon geliştirmektedir. Elektrik alanın yönü ve şiddeti, kullanıcı tarafından belirlenen yük değerleri ve konumlara göre gerçek zamanlı olarak hesaplanmakta ve görsel olarak gösterilmektedir. Python ile oluşturulan teorik altyapı, HTML, CSS ve JavaScript ile etkileşimli bir arayüze dönüştürülmüştür. Kullanıcılar yükleri sürükleyip parametrelerini değiştirebilir; simülasyon buna anlık olarak yanıt verir. Açık kaynaklı ve kurulum gerektirmeyen bu araç, öğrencilere kavramsal öğrenme desteği sunarken öğretmenler için de derslerde kullanılabilecek esnek bir eğitim materyalidir.

1. GİRİŞ

Elektrik Alan Kavramı ve Amaç

Elektrik alan, yüklerin birbirine uyguladığı kuvvetleri alan düzeyinde ifade eden, ancak doğrudan gözlemlenemediği için öğrenciler açısından kavranması güç bir kavramdır (Griffiths, 2017). Bu alanın büyüklüğü ve yönü, yük miktarı ve mesafeye bağlı olarak değişir. Temel olarak, birim pozitif test yüküne etki eden kuvvet şu şekilde tanımlanır:

$$\vec{E} = \frac{\vec{F}}{q} \quad \dots (1.1)$$

Tek bir noktasal yükün elektrik alanı ise **Coulomb yasası** kullanılarak hesaplanır:

$$\vec{F} = \frac{1}{4\pi\epsilon_0} \cdot \frac{q_1 q_2}{r^2} \cdot \hat{r} \dots (1.2)$$

Bu proje kapsamında, Python ile teorik modeller oluşturulmuş, ardından HTML ve JavaScript ile etkileşimli bir simülasyona dönüştürülmüştür. Kullanıcı, yükleri sahnede sürükleyebilir, büyüklüklerini değiştirebilir ve anlık olarak elektrik alan çizgilerini gözlemleyebilir. Simülasyon, kavramsal öğrenmeyi destekleyen etkili bir öğretim aracıdır.

2. GENEL BİLGİ
Simülasyonların Eğitimdeki Yeri

Simülasyonlar, özellikle fizik gibi soyut ve deneysel olarak erişimi zor kavramların öğreniminde etkili araçlardır. Öğrenciler, bu sayede farklı senaryoları düşük riskli bir ortamda deneyimleme ve neden-sonuç ilişkilerini aktif şekilde keşfetme imkânı bulurlar (Rutten, van Joolingen & van der Veen, 2012)[2]. Etkileşimli öğrenme ortamları, öğrencilerin bilgiyi pasif şekilde almak yerine, kendi kararlarıyla öğrenme sürecine katılımını teşvik eder (Jonassen, 1999)[3]. Bu projede geliştirilen simülasyon, diğer örneklerden farklı olarak kullanıcıya yük türü, büyüklüğü ve konumunu özgürce belirleme olanağı sunmakta; alan çizgilerini gerçek zamanlı ve yönlü olarak çizmektedir. Türkçe dil desteği sayesinde yerel eğitime daha uygun hâle gelmiş, erişilebilir ve özelleştirilebilir bir kaynak ortaya çıkmıştır; bu da simülasyonun farklı öğretim senaryolarına kolaylıkla uyarlanmasını mümkün kılmaktadır.

3. Yöntem
Araştırmanın Yöntemi ve Deseni

Bu çalışma, tasarım temelli araştırma yaklaşımıyla yapılandırılmıştır. Amacı, fizik eğitimi bağlamında kavramsal öğrenmeyi destekleyen etkileşimli bir öğretim materyali geliştirmektir. Tasarım sürecinde:

- Kavramsal doğruluk,
- Kullanıcı etkileşimi,
- Görsel anlaşılırlık

ilkeleri temel alınmıştır. Simülasyon, nitel gözlemler ve kullanıcı deneyimleri doğrultusunda sürekli olarak geliştirilmiş ve öğretim ortamlarında uygulanabilirliği test edilmiştir.

Geliştirme Sürecinde Kullanılan Teknolojiler

Simülasyon iki aşamalı bir teknoloji mimarisiyle geliştirilmiştir:

🔹 **1. Aşama – Teorik Modelleme (Python):**

Elektrik alanın fiziksel modeli Python ile hesaplanmıştır.

- NumPy: Vektörel işlemler için
- Matplotlib: Alan çizgilerinin görselleştirilmesi için

🔹 **2. Aşama – Etkileşimli Web Arayüzü (HTML/CSS/JavaScript):**

Simülasyon, JavaScript'in Canvas API yapısı ile geliştirildi.

- Kullanıcı, yükleri fareyle sürükleyebilir
- Yük büyüklüğü ve işareti klavyeden değiştirilebilir
- Alan çizgileri anlık ve yönlü olarak görselleştirilebilir.

Python ile Pozitif Noktasal Yükün Elektrik Alanı

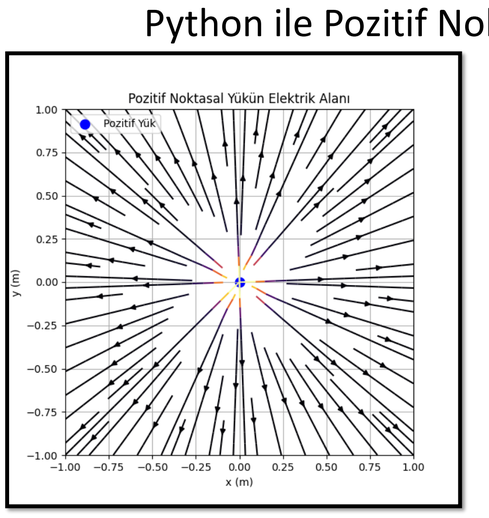

Şekil 1

Bu görselde, yalnızca bir pozitif yükün oluşturduğu elektrik alan çizgileri Python kullanılarak modellenmiştir. Yük, koordinat sisteminin merkezine yerleştirilmiş ve çevresindeki elektrik alan yönleri görselleştirilmiştir. Alan çizgileri yükten dışa doğru yönelmekte olup, şiddeti uzaklıkla birlikte azalmaktadır. Bu modelleme, simülasyonun fiziksel altyapısını oluşturan ilk adımdır ve elektrik alan kavramının sezgisel olarak anlaşılmasına katkı sağlar.

Geliştirilen Simülasyonlar

Şekil 2'de, öğrenci etkileşimine açık olarak geliştirilen ilk elektrik alan simülasyonunun bir negatif bir de pozitif iki yük eklenmiş halinin bir görüntüsü yer almaktadır. Kullanıcılar bu simülasyonda yük tipi ve büyüklüğünü seçerek sahneye yük ekleyebilmekte ve bu yüklerin konumları değiştikçe elektrik alan vektörlerinin yön ve şiddetleri anlık olarak yeniden hesaplanmaktadır. Hesaplanan bu şiddete bağlı olarak yüklerin etrafında ana kanvasın turkuaz renginden farklı olarak yoğunluklarına göre pembe renk değişimleri meydana gelmektedir. Bu yapı, öğrencilerin elektrik alan kavramını deneyimleyerek öğrenmesini desteklemektedir.

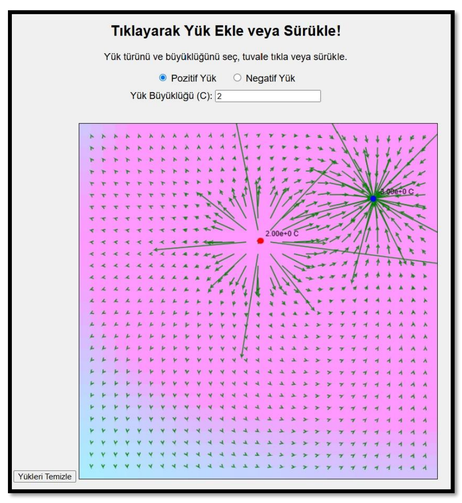

Şekil 2

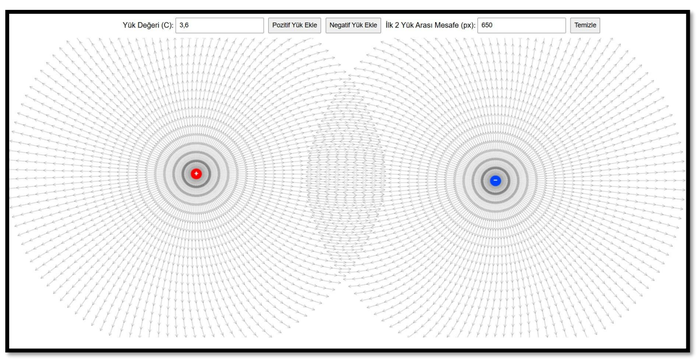

Şekil 3

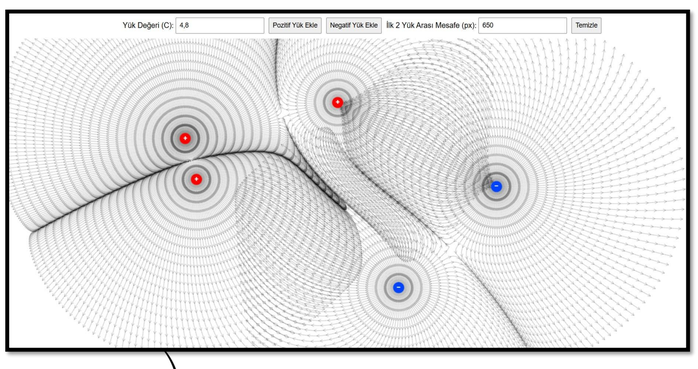

Şekil 4

Şekil 3 ise ikinci bir simülasyonun görselidir. Bu görsel simülasyona kullanıcı tarafından tuval üzerine yerleştirilen pozitif (kırmızı) ve negatif (mavi) yüklerin oluşturduğu elektrik alanı göstermektedir. Yüklerin büyüklüğü, kutupları ve konumları manuel olarak ayarlanabilmekte; her yük etrafındaki elektrik alan çizgileri Coulomb yasasına göre yönlü olarak hesaplanmakta ve görsel olarak temsil edilmektedir. Eklenen ilk iki yük sayfanın merkezlerine varsayılan olarak atanmaktadır. Bu iki yük arasındaki mesafe kullanıcının yükleri hareket ettirmesine bağlı olarak kutucuğun içinde anlık olarak gözlenebilmektedir. Eklenen diğer yükler ise –pozitif veya negatif fark etmeksizin kanvasa rastgele bir şekilde yerleştirilmektedir. Eklenen 'Temizle' butonu ile de eklenmiş tüm yükler sayfayı yenilemeye gerek kalmadan kanvası varsayılan haline getirmektedir. İkinci simülasyonun ayırt edici yönü, elektrik alan çizgilerinin eğrisel ('curve') biçimde çizilebilmesidir.

4. Sonuç ve Tartışma

Bu projede, fiziksel kavramların yalnızca teorik düzlemde değil; öğrencinin doğrudan müdahale edebileceği dijital ortamlarda da yapılandırılabileceği gösterilmiştir. Elektrik alan gibi soyut ve yönlü bir kavram, geliştirilen simülasyon sayesinde, sürüklenebilir yükler ve anlık görselleştirme yoluyla somut ve deneyimlenebilir hâle getirilmiştir. Öğrenciler, yüklerin etkilerini yalnızca sayısal değil, sezgisel olarak da gözlemleyebilmiş, böylece öğrenme süreci daha içsel ve kalıcı bir hâl almıştır.

Kullanılan Python hesaplama temeli ve web tabanlı arayüz, hem bilimsel doğruluk hem de erişim kolaylığı sunarak, dijital materyallerin eğitimdeki rolünü güçlendirmiştir. Geleneksel öğretimin sınırlarını aşan bu etkileşimli yapı, öğrencinin pasif alıcıdan aktif keşfedene dönüşmesine olanak tanımıştır. Sonuç olarak, bu çalışma yalnızca bir simülasyon değil, fizik eğitimi için düşünülmüş bütünsel bir öğrenme ortamı önerisi sunmaktadır.

Simülasyon temelli bu yaklaşım, elektrik potansiyeli, manyetik alan gibi diğer konulara da uyarlanabilir. Gelecekte, simülasyonun öğrenme üzerindeki etkisini değerlendiren deneysel çalışmalar yapılabilir. Ayrıca, ölçme-değerlendirme, sesli anlatım ve rehberlik sistemleriyle donatılarak öğretim süreci daha da zenginleştirilebilir. Farklı yaş gruplarına yönelik özelleştirmelerle, ortaöğretimden üniversiteye kadar yaygın kullanımı hedeflenmektedir.

KAYNAKÇA

[1] Griffiths, D. J. (2017). *Introduction to Electrodynamics* (4th ed.). Cambridge University Press.

[2] Rutten, N., van Joolingen, W. R., & van der Veen, J. T. (2012). The learning effects of computer simulations in science education. *Computers & Education*, 58(1), 136–153.

[3] Jonassen, D. H. (1999). Designing constructivist learning environments. In C. M. Reigeluth (Ed.), *Instructional-design theories and models: A new paradigm of instructional theory* (Vol. II, pp. 215–239). Lawrence Erlbaum Associates.

2024-2025 Bahar Yarıyılı Fizik BÖLÜMÜ

MARS İYONOSFERİNDE GÜNEŞ FIRTINASI VE KORONAL KÜTLE ATIMI KAYNAKLI BOZULMALAR:

17–18 MAYIS 2024 OLAYINA DAYALI BİR VAKA ÇALIŞMASI

Yasmina YEGE 20022072

Danışman: Doç. Dr. Zehra CAN

Bu çalışmada, 17–18 Mayıs 2024'te meydana gelen güneş rüzgârının Mars atmosferinde oluşturduğu etkiler incelenmiştir. İlk olarak WSA-ENLIL simülasyonlarıyla güneş rüzgârının Güneş'ten Mars'a kadar olan yolculuğu ve özellikleri belirlenmiştir. Daha sonra, MAVEN uzay aracından elde edilen elektron yoğunluğu, manyetik alan, sıcaklık ve rüzgâr hızı gibi veriler analiz edilerek Mars iyonosferinde meydana gelen değişimler ortaya konulmuştur. Sonuçlar, güneş rüzgârının Mars atmosferinde fiziksel ve kimyasal değişimlere neden olmuş ve bunun uzay hava koşullarının anlaşılmasına katkıda bulunacağını göstermiştir.

1. GÜNEŞ OLAYLARININ MARS İYONOSFERİNE ETKİSİ

Mars iyonosferi, yeryüzünden 80-400 km yükseklikleri arasında bulunan güneş ışınları tarafından iyonize olmuş doğal bir plazma tabakasıdır. Mars'ın Dünya'daki gibi küresel manyetik alanından ziyade yerel manyetik alanları vardır, dolayısıyla Mars iyonosferi doğrudan güneş aktivitelerine maruz kalır. Aşağıdaki Şekil 1.1'de güneş aktivitelerinin Mars'la etkileşimi, Şekil 1.2'de Mars iyonosferi gösterilmektedir.

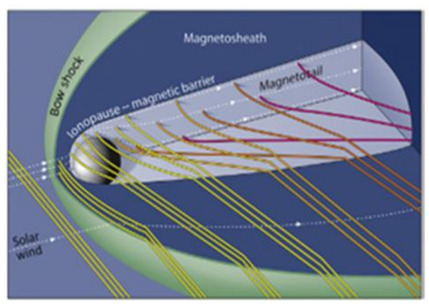

Şekil 1.1 Güneş aktivitelerinin Mars'la etkileşimi [1]

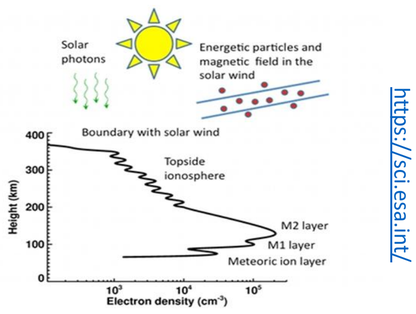

Şekil 1.2 Mars iyonosferi

2. MATERYAL VE METOD

Python Jupyter Notebook kullanarak 17-18 Mayıs 2024 tarihlerine ait güneş rüzgârı-iyonosfer etkileşmesini gözlemlemek için NASA'nın MAVEN uzay aracının MAG misyonuna ait manyetik alan verileri, LPW misyonundan elektron yoğunluğu ve sıcaklığı verileri, SWIA misyonundan toplam iyon basıncı ve hızı verileri ve SPICE misyonundan uzay aracının konum bilgilerine ait veriler alınmıştır. Bu veriler CSV formatında olup ilgili zaman damgaları ile birlikte işlenmiştir.

```
import pandas as pd
import numpy as np
import matplotlib.pyplot as plt
import seaborn as sns # Korelasyon matrisi görselleştirmesi için
import os

# --- 1. Dosya Yolları (Bu yolların doğru olduğundan eminsiniz) ---
lpw_file = r'C:\Users\90530\Desktop\bitirme tezi dosyası\mvn_kp_insitu_20240518_v22_r01.csv'
mag_file = r'C:\Users\90530\Desktop\bitirme tezi dosyası\mvn_mag_l2_2024139pc1s_20240518_v01_r01.csv'
swi_file = r'C:\Users\90530\Desktop\bitirme tezi dosyası\MVN_SWI_L2_ONBOARDSVYMOM_1040919.csv'
```

Şekil 2.1 İşlenen CSV verileri

```
# Zamanları yuvarla
df_mag['time_rounded'] = df_mag['SAMPLE UTC'].dt.floor('T')
df_lp['time_rounded'] = df_lp['Time (UTC/SCET)'].dt.floor('T')

# Birleştir
merged_df = pd.merge(df_mag, df_lp, on='time_rounded', how='inner')
```

Şekil 2.2 Verilerin uygun zaman formatında birleştirilmesi

```
# --- 7. Korelasyon Matrisini Hesapla ve Görselleştir ---
if not combined_df_final.empty:
    correlation_matrix = combined_df_final.corr()

    print("\n--- Korelasyon Matrisi ---")
    print(correlation_matrix)

    plt.figure(figsize=(12, 10)) # Boyut biraz artırıldı
    sns.heatmap(correlation_matrix, annot=True, cmap='coolwarm', fmt=".2f", linewidths=.5, cbar_kws={'label': 'Korelasyon Katsayı
    plt.title('MAVEN Veri Parametreleri Arası Korelasyon Matrisi')
    plt.show()
else:
    print("\nBirleştirilmiş ve temizlenmiş veri seti boş olduğundan korelasyon matrisi hesaplanamıyor.")
    print("Lütfen dosya yollarının ve sütun adlarının doğru olduğundan, ayrıca dosyalarınızda yeterli örtüşen veri olduğundan emi
```

Şekil 2.3 Korelasyon matrisinin elde edilmesi

3. VERİLERİN ANALİZ EDİLMESİ VE YORUMLANMASI

17 MAYIS 2024

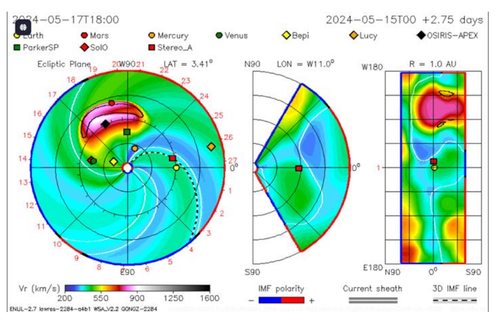

Şekil 3.1 17 Mayıs 2024 CME atılımı [2]

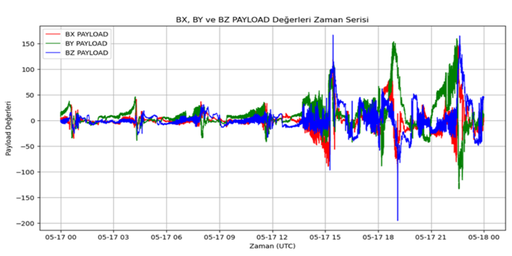

Şekil 3.3 17 Mayıs 2024 manyetik alan bileşenleri [3]

18 MAYIS 2024

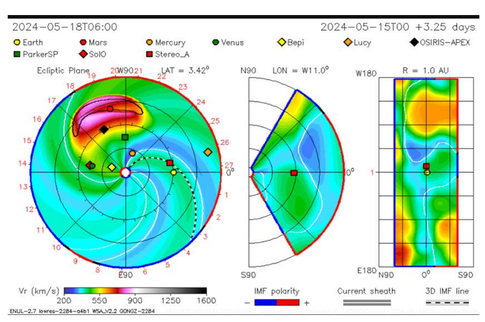

Şekil 3.2 18 Mayıs 2024 CME atılımı[2]

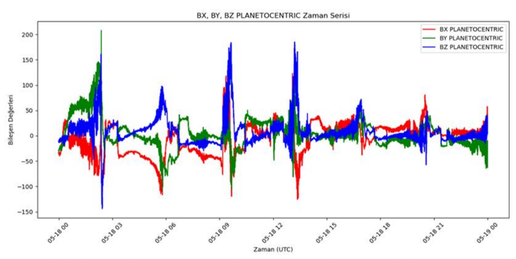

Şekil 3.4 18 Mayıs 2024 manyetik alan bileşenleri[3]

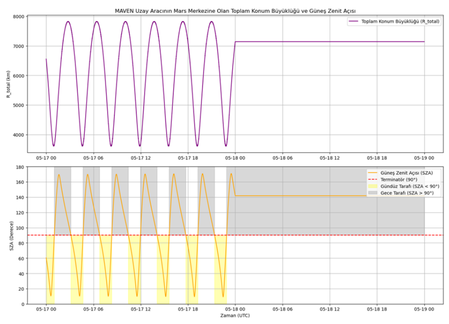

Şekil 3.5 17 Mayıs 2024 uydu konum bilgileri[3]

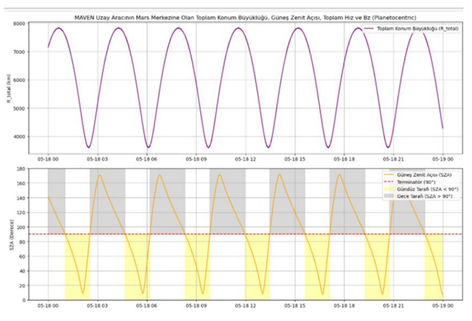

Şekil 3.6 18 Mayıs 2024 uydu konum bilgileri [3]

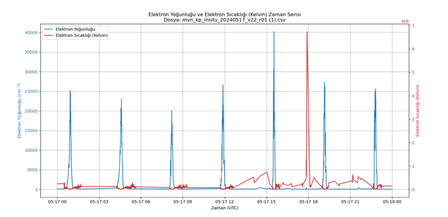

Şekil 3.7 17 Mayıs 2024 elektron sıcaklığı ve yoğunluğu [3]

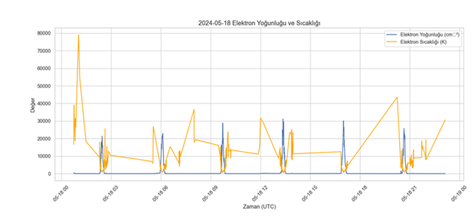

Şekil 3.8 18 Mayıs 2024 elektron sıcaklığı ve yoğunluğu [3]

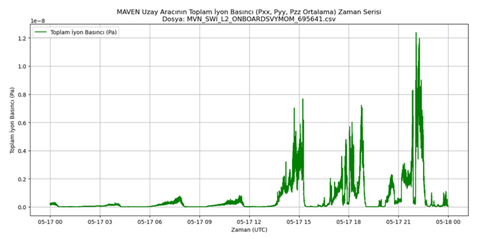

Şekil 3.9 17 Mayıs 2024 iyon basıncı [3]

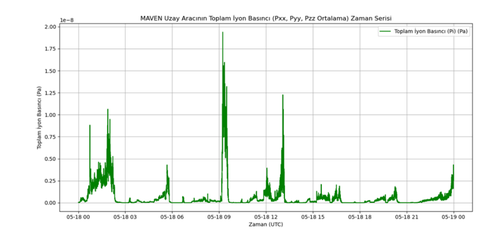

Şekil 3.10 18 Mayıs 2024 iyon basıncı [3]

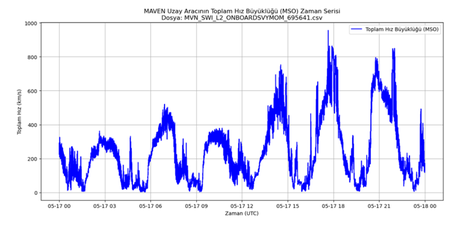

Şekil 3.11 17 Mayıs 2024 iyon hızı [3]

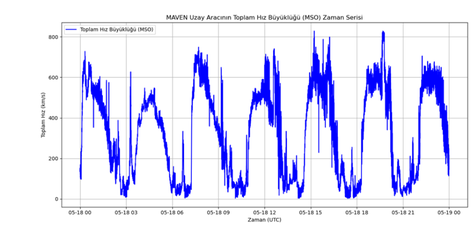

Şekil 3.12 18 Mayıs 2024 iyon hızı [3]

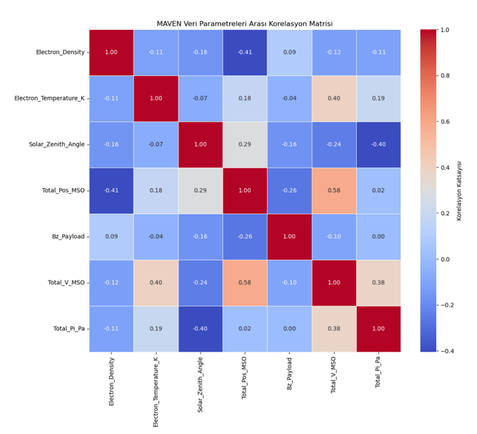

Şekil 3.13 17 Mayıs 2024 korelasyon matrisi [3]

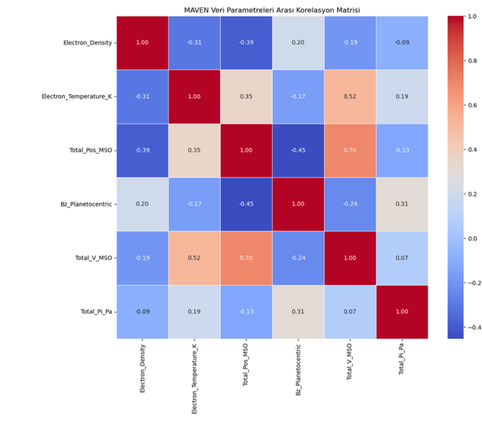

Şekil 3.14 18 Mayıs 2024 korelasyon matrisi[3]

4. SONUÇ VE TARTIŞMA

Bu çalışmada, 17–18 Mayıs 2024'te meydana gelen koronal kütle atılımının Mars atmosferinde oluşturduğu etkiler, simülasyonlar ve gözlemlerle incelenmiştir. WSA-ENLIL ve MAVEN verileriyle, güneş rüzgârının Mars'a ulaşma süreci ve iyonosferde neden olduğu değişimler ortaya konulmaya çalışılmıştır. Ancak, kısa zaman aralığı ve sınırlı veri sebebiyle belirgin korelasyonlar elde edilememiştir. Bu sonuçlar, daha kapsamlı çalışmalarla Mars atmosferinin uzay havasına tepkisinin daha iyi anlaşılabileceğine işaret etmektedir.

KAYNAKÇA

[1] M. G. Kivelson ve F. Bagenal, "Planetary Magnetospheres," Department of Earth & Space Sciences, University of California, Los Angeles ve Department of Astrophysical & Planetary Sciences, University of Colorado, Boulder, 2025.
[2] https://kauai.ccmc.gsfc.nasa.gov/DONKI/search/
[3] https://pds-ppi.igpp.ucla.edu/mission/MAVEN

2024-2025 Spring Semester-Department of Physics

ENERGY-BASED LEARNING: PHYSICAL MODELING OF COGNITIVE PROCESSES USING A BOLTZMANN MACHINE

Aleyna Nur EROĞLU 2002029

Advisor: Prof. Dr. Orhan ÖZDEMİR

ABSTRACT

“What is the mind?” is one of the most important and still unanswered questions in science. Researchers have discovered that the human brain contains about 100 billion neurons, which can form countless patterns through their connections. Today, studies suggest that the mind can be seen not only as a biological structure, but also as a physical and information-processing system.In this project, mental processes are modeled using Donald Hebb’s theory of learning, John Hopfield’s energy-based network, and Geoffrey Hinton’s Boltzmann Machine. The simulation shows that missing information can be completed through an energy-based network, just like how the brain remembers or fills in gaps.This idea is closely related to the 2024 Nobel Prize in Physics, which also focused on energy-based learning systems for understanding how thinking can emerge from physical processes.

The Significance of Physical Modeling in Understanding the Brain

Until the 2000s, the brain was mainly seen as a control center for bodily functions. This view shifted with the launch of the **Human Brain Project (HBP) in 2012,** a European initiative that aimed to simulate and understand the human brain through advanced computational models.With this Project today, the brain is increasingly seen not just as a biological organ, but as a physical and computational system capable of generating the mind. This perspective is supported by neuroscience, physics, and systems theory.

In this model, neural activity follows the principle of energy minimization, similar to how physical systems move toward stable, low-energy states. From a thermodynamic view, the brain is an open, far-from-equilibrium system that exchanges energy and information with its environment. Neural networks aim to reduce energy cost while preserving complexity—mirroring physical systems that locally reduce entropy under global constraints.

Foundational Concepts: Neural and Biological Bases

Donald Hebb(1949): Hebbian Rule

Canadian psychologist Donald Hebb proposed that learning happens when connections between neurons are strengthened. He summarized this with the phrase:

“Neurons that wire together, fire together”. *-Hebb’s Rule*

This idea formed the basis of **artificial neural networks**, suggesting that the **mind** emerges from **patterns** of neural activity. Hebb’s concept of a **cell assembly** explains how thoughts are represented by groups of co-activating neurons.[1]

Hopfield Network: Energy-Based Modeling of Mental States

Physicist **John Hopfield** combined Hebb’s connectionist ideas with physical modeling by developing a neural network based on **energy minimization**[2].The **Hopfield network** represents memory as **stable patterns** in an energy landscape.The system recognizes incomplete or noisy input by settling into a **low-energy state**, similar to how the brain retrieves memories**.** The behavior of the Hopfield network is governed by an energy function:

$$E = -\frac{1}{2}\sum_{i \neq j} w_i s_i s_j + \sum_j \theta_i s_i$$

From Hopfield to Hinton: The Expansion of Energy-Based Learning

In 1985, **Geoffrey Hinton** developed the **Boltzmann Machine**, defining learning in terms of **energy minimization** and **probability distributions**. This model showed that mental processes can be simulated using physical and computational systems. **Mental patterns** are represented as **stable, low-energy states**, and the system’s ability to complete missing information reflects a process similar to thinking. In this view, the mind operates like a **physical system** navigating an **energy landscape**, seeking the most probable and balanced state.[3]

$$E(v,h) = -\sum_i b_i v_i - \sum_j c_j h_j - \sum_{i,j} v_i w_{ij} h_j$$

What is Boltzmann Machines

Named after physicist **Ludwig Boltzmann** and developed by **Geoffrey Hinton**, Boltzmann Machines are neural network models that combine statistical physics with machine learning to simulate how systems learn and represent information through probabilistic energy-based processes. (Hinton & Sejnowski, 1986)

These networks represent a system in which different states emerge with different **probabilities**, depending on their **associated energy levels**. There are six main types of Boltzmann Machines in total, and in this project, a Restricted Boltzmann Machine (RBM) was modeled.

Restricted Boltzmann Machine (RBM)

An RBM is a neural network with two layers — visible and hidden — connected across but not within layers. This structure enables efficient learning by minimizing energy, allowing the system to store and reconstruct patterns from incomplete input.

1. Model Selection and Theoretical Foundations

We implemented a **Restricted Boltzmann Machine (RBM)** with 8×8 visible units and 32 hidden units. This architecture is inspired by **Donald Hebb’s concept of neuronal pattern representation**, where each 0/1 activation is viewed as the neural projection of a mental concept.

```
# --- 1. Veri Kümesini Hazırla ---
digits = load_digits()
X = digits.data
X = Binarizer(threshold=8).fit_transform(X)  # Piksel değerlerini 0-1'e çevir
X = torch.tensor(X, dtype=torch.float32)

# --- 2. RBM Model Sınıfı ---
class RBM(nn.Module):
    def __init__(self, n_visible, n_hidden):
        super(RBM, self).__init__()
        self.W = nn.Parameter(torch.randn(n_hidden, n_visible) * 0.01)
        self.v_bias = nn.Parameter(torch.zeros(n_visible))
        self.h_bias = nn.Parameter(torch.zeros(n_hidden))

    def sample_h(self, v):
        prob = torch.sigmoid(torch.matmul(v, self.W.t()) + self.h_bias)
        return prob, torch.bernoulli(prob)

    def sample_v(self, h):
        prob = torch.sigmoid(torch.matmul(h, self.W) + self.v_bias)
        return prob, torch.bernoulli(prob)

    def forward(self, v):
        _, h_sample = self.sample_h(v)
        _, v_sample = self.sample_v(h_sample)
        return v_sample

    def energy(self, v):
        h_prob, _ = self.sample_h(v)
        term1 = torch.matmul(h_prob, self.h_bias)
        term2 = torch.matmul(v, self.v_bias)
        term3 = torch.sum(torch.matmul(h_prob, self.W) * v, dim=1)
        return -torch.mean(term1 + term2 + term3)
```

```
# --- 3. RBM Öğrenme Fonksiyonu ---
def train_rbm(rbm, data, epochs=10, lr=0.01):
    energy_history = []
    for epoch in range(epochs):
        epoch_error = 0
        for v in data:
            v = v.view(1, -1)
            prob_h, h_sample = rbm.sample_h(v)
            prob_v, v_sample = rbm.sample_v(h_sample)
            prob_h_rec, _ = rbm.sample_h(v_sample)

            rbm.W.data += lr * (torch.matmul(prob_h.t(), v) - torch.matmul(prob_h_rec.
            rbm.v_bias.data += lr * (v - v_sample).sum(0)
            rbm.h_bias.data += lr * (prob_h - prob_h_rec).sum(0)

            epoch_error += torch.sum((v - v_sample) ** 2).item()
        mean_energy = rbm.energy(data).item()
        energy_history.append(mean_energy)
        print(f"Epoch {epoch+1}, Error: {epoch_error:.4f}, Energy: {mean_energy:.4f}")

    # Enerji grafiğini çiz
    plt.figure(figsize=(8,4))
    plt.plot(range(1, epochs+1), energy_history, marker='o')
    plt.title("Öğrenme Sürecinde Enerji Değişimi")
    plt.xlabel("Epoch")
    plt.ylabel("Ortalama Enerji")
    plt.grid(True)
    plt.tight_layout()
    plt.show()

# --- 4. Modeli Kur ve Eğit ---
rbm = RBM(n_visible=64, n_hidden=32)
train_rbm(rbm, X, epochs=10, lr=0.1)
```

2. Probabilistic Learning and Activation

The network uses **sigmoid activation and Bernoulli sampling** in its forward and backward passes. This reflects **Geoffrey Hinton’s probabilistic learning paradigm** in Boltzmann Machines—learning the data’s structure through energy-based probability distributions.

3. Energy Function and Stability Principle

The network’s energy function is given by:

$$E = -\sum_i b_i v_i - \sum_j c_j h_j - \sum_{i,j} v_i w_{ij} h_j$$

This formulation merges Hebb’s concept of pattern representation with **John Hopfield’s idea of stable patterns as energy minima**.

4. Training Process and Energy Monitoring

During training, we perform visible-to-hidden (v → h) and hidden-to-visible (h → v) passes to update weights. At the end of each epoch, we measure the average energy level and observe the system converging toward a **lower, more stable region in the energy landscape**.

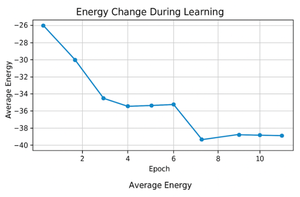

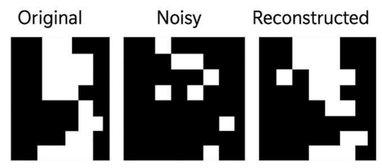

5. Pattern Completion and Cognitive Inference

When presented with incomplete input, the RBM reconstructs the missing parts. This mimics the mind’s ability to **infer a coherent whole from partial information**, demonstrating cognitive-like recall capabilities.

This simulation synthesizes the theoretical foundations of **Hebb, Hopfield, and Hinton** to successfully simulate **mental representation and retrieval** through an energy-based artificial neural network.

Conclusion and Contributions

This project demonstrates that mental processes can be explained through the principles of **energy minimization** and **probabilistic structuring** in physics by using Boltzmann Machines. The simulation shows that an artificial network can successfully complete missing patterns, mimicking functions like **memory** and **learning**. This supports the idea that the mind is not only a biological system, but also a system that can be understood through the **laws of physics**. This approach models mental processes and neurological disorders through energy imbalances in the brain, opening new possibilities for early diagnosis and treatment. It also helps decode brain signals more accurately using physical systems, supporting the development of advanced technologies like brain–computer interfaces.

Related Global Research

AlphaFold (2020)is an AI system developed by DeepMind that predicts the 3D structure of proteins based only on their amino acid sequence. It solves the long-standing “folding problem” by combining deep learning with physical principles, identifying the most stable structure as the one with the lowest energy.

Human Connectome Project (2009–2018), this project mapped the brain’s neural connections, showing that thoughts and memories arise from specific patterns of connectivity—supporting Hebb’s idea that mental functions emerge from structured neural networks.

REFERENCES

[1] Hebb, D. O. (1949). *The Organization of Behavior: A Neuropsychological Theory*. Wiley.

[2] Hopfield, J. J. (1982). Neural networks and physical systems with emergent collective computational abilities. *Proceedings of the National Academy of Sciences*, 79(8), 2554–2558.

[3] Hinton, G. E., & Sejnowski, T. J. (1986). Learning and Relearning in Boltzmann Machines. In D. E. Rumelhart & J. L. McClelland (Eds.), *Parallel Distributed Processing: Explorations in the Microstructure of Cognition* (Vol. 1, pp. 282–317). MIT Press.

2024-2025 Spring Semester

Physics Department

ASTEROID DATA AND ORBIT ANALYSIS

Onur AKDEMİR 20022017

Supervisor: Dr. Res. Asst. Muhammed Kıyami ERDİM

Abstarct

The primary objective of this study is to analyze and predict the orbital trajectories of asteroids using artificial intelligence techniques. The project specifically addresses the challenge of estimating the future orbit of newly discovered or recently observed asteroids by utilizing their initial position and velocity vectors. For this purpose, data were collected from NASA's JPL Horizons API, and a supervised machine learning model—Multi-Layer Perceptron Regressor (MLPRegressor)—was implemented. The model was trained to learn the nonlinear relationship between state vectors and Keplerian orbital elements, including semi-major axis, eccentricity, inclination, and angular parameters. After training, the system was used to predict the orbital elements of asteroids not included in the training set. The predicted trajectories were validated through numerical error analysis and 3D visualizations. This approach demonstrates the potential of AI-assisted modeling in orbital prediction tasks, especially for near-Earth objects where rapid and accurate forecasting is critical for planetary defense.

Data Collection and Preprocessing

Source of Data:
Orbital data were retrieved from the **Minor Planet Center (MPC) API**, which provides accurate and updated information for small Solar System bodies. Key orbital parameters collected include:

- **Semi-major axis (a)**
- **Eccentricity (e)**
- **Inclination (i)**
- **Longitude of ascending node (Ω)**
- **Argument of perihelion (ω)**
- **Mean anomaly (M)**

Additional Metadata:
To support classification and risk analysis, supplementary parameters were also obtained:

- **Observation arc duration**
- **Epoch** (converted to Julian dates)
- **Minimum Orbit Intersection Distance (MOID)**
- **Absolute magnitude (H)**

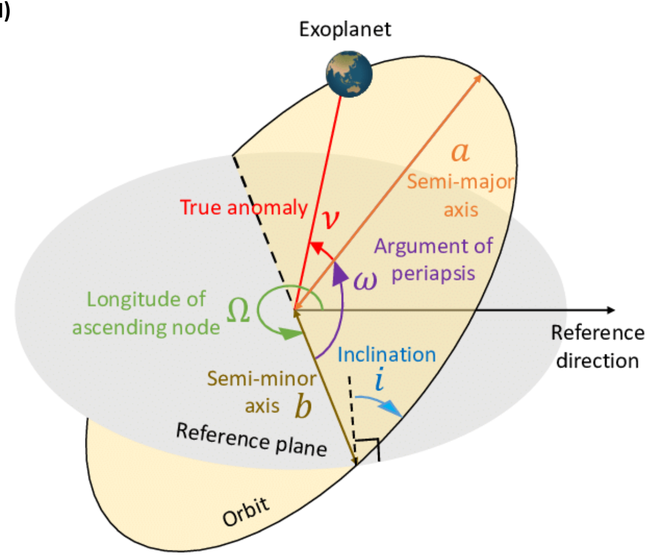

Figure 1: Diagram illustrating the primary Keplerian elements that define the size, shape, and orientation of an orbit in space.

AI Model Development and Implementation Logic

In this study, a supervised machine learning approach was employed to predict the orbital elements of asteroids based on their position and velocity vectors. The core algorithm used was **Multi-Layer Perceptron Regressor (MLPRegressor)**from the scikit-learn library. This model was selected for its ability to capture non-linear relationships between six-dimensional input vectors —**(x, y, z, vx, vy, vz)**— and five Keplerian output parameters: **semi-major axis (a), eccentricity (e), inclination (i), longitude of ascending node (Ω), and argument of perihelion (ω)**.

Model Training and Validation

- Data for asteroid Ceres was collected via the **NASA JPL Horizons API** over a 20-day interval, producing multiple (r, v) pairs.
- For each state vector, the corresponding Kepler elements were computed using the Orbit.from_vectors() method from the **Poliastro** library.
- Inputs and targets were scaled using StandardScaler to improve numerical stability during training.
- The dataset was split into **80% training** and **20% testing** sets using train_test_split().

Performance Evaluation

Model performance was assessed using:

- **Mean Squared Error (MSE)** between actual and predicted values,
- **Numerical comparison** of predicted orbital elements for unseen test samples,
- **Visual inspection** through 3D orbit plots, showing the spatial match between real and predicted orbits.

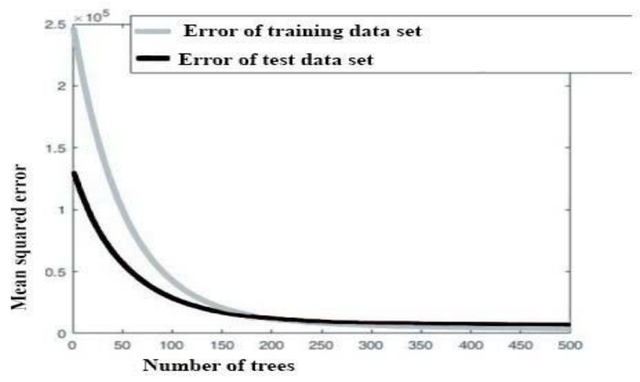

Figure 2: Convergence of training and test error as the number of trees increases, illustrating improved model performance and generalization.

3D Orbit Visualization

Using **matplotlib** and **poliastro**, the first predicted orbit was propagated and plotted in a 3D heliocentric frame. The Sun was fixed at the center, and orbital paths were displayed with annotations of the predicted parameters. This step validated the model not only numerically but also geometrically, offering intuitive insight into model accuracy.

Visualization in Python (matplotlib, poliastro, etc.)

The computed orbits were visualized in 2D and 3D using matplotlib and poliastro, highlighting orbital shape, orientation, and spatial dynamics in a heliocentric frame.

Identification of Earth-Approaching Asteroids

While Ceres was the focus, the system is adaptable for monitoring Near-Earth Objects (NEOs) by tracking parameters like MOID and eccentricity.

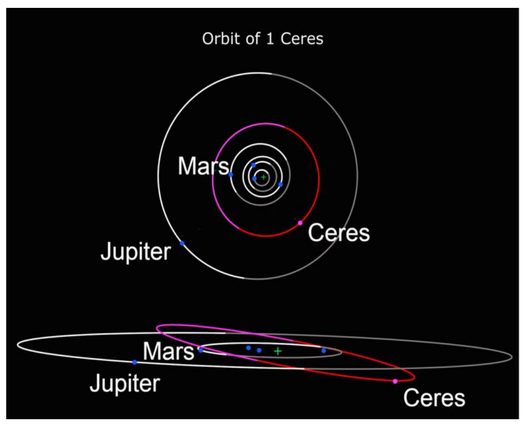

Figure 3

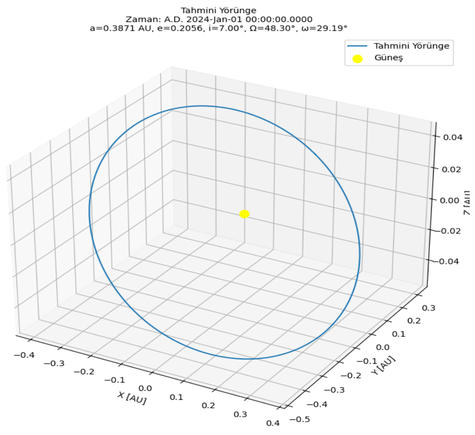

Figure 4

Orbit Simulation

Orbit propagation techniques were applied to simulate future asteroid positions over time, offering a dynamic understanding of their long-term behavior.

Concluson and Discussion

- **Aim:** Leverage machine-learning (ML) models—tested here with an MLP—to predict asteroid orbits faster and with less computational load than traditional N-body simulations.
- **Findings:** On a Ceres-only dataset, the ML approach reproduced Keplerian elements with good accuracy, confirming the feasibility of AI-aided orbit prediction for planetary-defense tasks.
- **Limitations:** Prediction quality hinges on input data; wider, more diverse asteroid datasets and sequential models (e.g., LSTM, Transformer) are needed for robust, long-term forecasting.
- **Future Work:**
  - Expand training data to multiple asteroid classes (Amor, Apollo, Aten).
  - Add physics-based features (Yarkovsky, planetary perturbations, solar radiation).
  - Integrate real-time observations for adaptive re-training.
  - Pair predictions with 3-D visualizations and impact-risk metrics to aid rapid decision-making.

Overall, combining ML with classical astrodynamics promises faster, scalable orbit prediction—an essential advance for space-situational awareness and Earth-impact prevention.

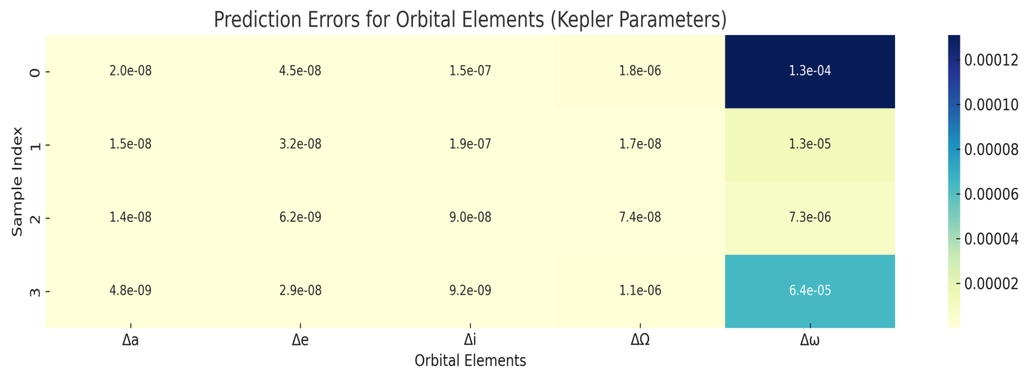

Figure 5: Table visualization of absolute error values (Δ) between predicted and true values for key Keplerian orbital elements.

KAYNAKÇA

[1] Cano, J. L. (2019). Poliastro: Astrodynamics in Python. *Journal of Open Source Software*, 4(38), 1404.
[2] NASA Jet Propulsion Laboratory. (2020). *NEO API: Open Access Data*. Retrieved from https://neo.jpl.nasa.gov/api
[3] Zhu, J., et al. (2018). *Orbital Mechanics and Its Applications in Predicting NEO Trajectories*. Space Science Reviews, 214(6), 75-90.
[4] Milani, A., & Gronchi, G. F. (2010). *Theory of orbit determination*. Cambridge University Press.

2024-2025 Bahar Yarıyılı

FİZİK BÖLÜMÜ

MUON DETECTORS

Murat SARIOSMANOĞLU 18022071

Danışman: Prof. Dr. Kutsal BOZKURT

Abstract

This thesis offers an in-depth analysis of muon detection systems, delving into the fundamental physics of muons as well as the diverse technologies developed to detect them. It begins by exploring the unique properties and production mechanisms of muons, followed by an extensive review of the different types of detectors employed to observe and measure these particles. The study particularly emphasizes the implementation of

WHAT IS MUON ?

The muon is a fundamental subatomic particle belonging to the lepton family, alongside the electron and the tau. It is symbolized by the Greek letter μ and classified as a second generation charged lepton. Like the electron, it carries an electric charge of –1 elementary charge (–1 e) and has an intrinsic spin of ½ ħ, making it a fermion under the Pauli exclusion principle.One of the muon's most distinctive properties is its mass, which is approximately 105.66 MeV/c², or about 206.77 times heavier than the electron.

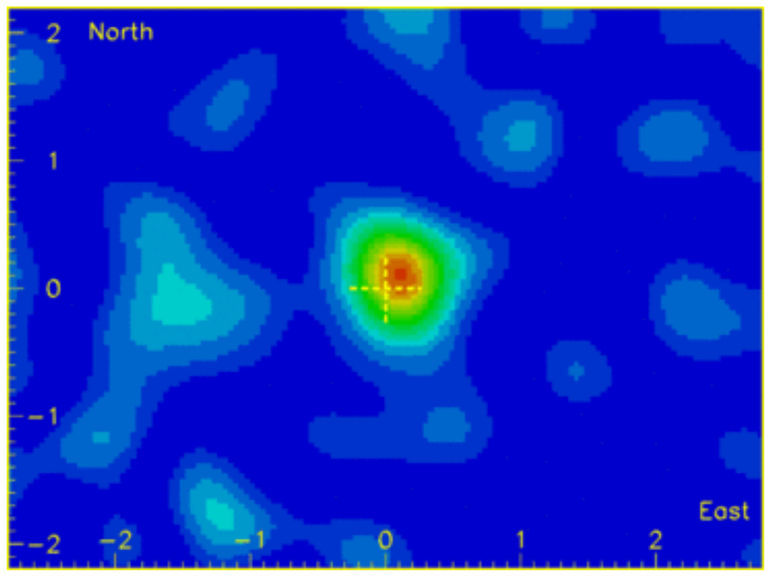

This image shows the "shadow" of the Moon in muons, as observed by the Soudan 2 detector, located 700 meters underground in the Soudan Mine, Minnesota.

DISCOVERY

The muon was first discovered in 1936 by Carl D. Anderson and Seth Neddermeyer at the California Institute of Technology while they were investigating cosmic radiation using cloud chambers. During their experiments, they observed particles that behaved differently from known particles like electrons or protons when passed through a magnetic field. These new particles were negatively charged, like electrons, but exhibited less curvature in the field—suggesting a greater mass than the electron, yet lighter than a proton at the same velocity.

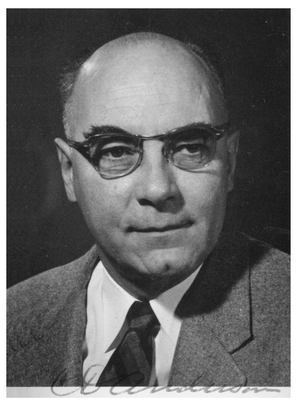

CARL DAVID ANDERSON

Why Detect Muons?

Detecting muons is essential across a wide range of scientific and practical applications due to their unique properties, such as high penetration power and predictable behavior. In high-energy particle physics, muon detection plays a critical role in collision experiments at particle accelerators like the Large Hadron Collider (LHC), where identifying muons helps reconstruct complex particle interactions and test predictions of the Standard Model. In cosmic ray research, muon detection provides insight into high-energy processes occurring in the upper atmosphere and space. Beyond fundamental physics, muons are increasingly valuable in non-invasive imaging techniques such asmuon tomography, which is used in volcanology to map internal magma chambers, and in archaeology to reveal hidden chambers in ancient structures like pyramids. Additionally, muon detectors are employed in nuclear reactor monitoring and security, as muons can penetrate shielding and help verify the presence or absence of fissile materials without intrusive measures.

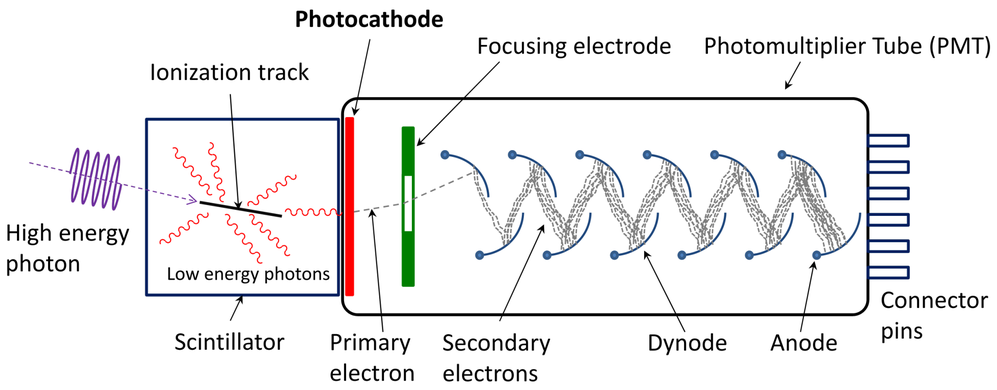

Muon Production Mechanisms

Muons are primarily produced through high-energy particle interactions, rather than typical radioactive decay, due to their relatively large mass. The most common natural source of muons is cosmic ray interactions in the Earth's upper atmosphere. When high- energy cosmic rays—mostly protons—collide with atmospheric nuclei, they produce pions (π mesons) and kaons (K mesons). These unstable mesons rapidly decay into muons and associated neutrinos.

Detector Technologies Overview

Muon detection relies on a variety of specialized detector technologies, each with distinct principles of operation tailored to muons' deep-penetrating and weakly interacting nature. The main categories of muon detectors include:

Scintillation Detectors: These detectors use materials that emit light (scintillate) when a charged particle like a muon passes through.

Gaseous Ionization Detectors: This category includes devices like drift tubes, multi-wire proportional chambers, and resistive plate chambers (RPCs).

Several types of gaseous ionization detectors are used in muon detection:

Drift Tubes: Cylindrical detectors where ionization electrons drift toward a central wire.

Multi-Wire Proportional Chambers (MWPCs): These use a grid of fine wires to collect ionization charges.

Resistive Plate Chambers (RPCs): Made of two resistive plates separated by a gas gap, RPCs produce fast signals and are commonly used in trigger systems due to their precise timing characteristics.

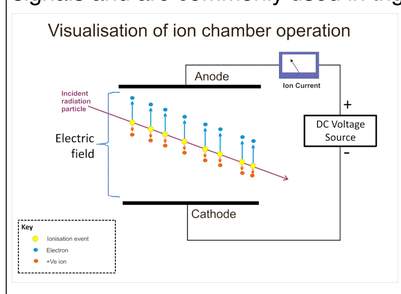

Ionization Chamber

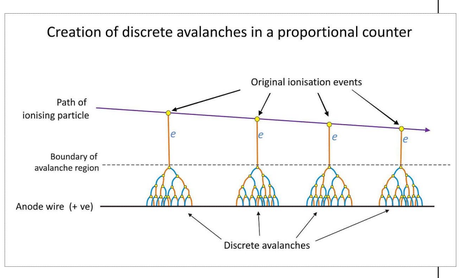

Proportional Counters

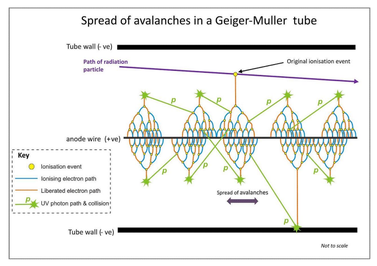

Geiger-Müller Tubes

Nuclear Emulsion Detectors: These detectors consist of photographic emulsions that record the tracks of charged particles

Cherenkov Detectors: These detectors exploit Cherenkov radiation, which occurs when a particle like a muon travels faster than the speed of light in a given medium (e.g., water or glass).

ATLAS Muon System at CERN

The ATLAS Muon System is a vital component of the ATLAS experiment at the Large Hadron Collider (LHC) at CERN, specifically designed to detect and measure muons, which often escape the dense inner detector layers due to their high penetration power. As muons are key signatures of many important physics processes—including Higgs boson decays, new particle searches, and Standard Model tests—precise muon detection is essential for accurate event reconstruction.

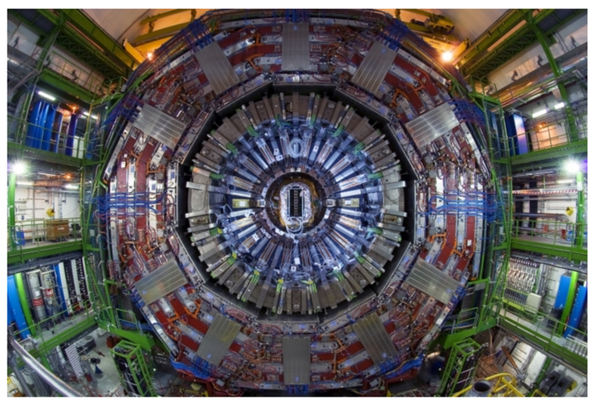

CERN - ATLAS

REFERENCES

-ATLAS Collaboration. (n.d.). ATLAS Experiment at CERN. Retrieved from https://atlas.cern

-CERN. (n.d.). Particle Physics and Detector Technologies. CERN. Retrieved from https://home.cern

- IAEA. (n.d.). Nuclear Applications of Particle Detection. International Atomic Energy Agency. Retrieved from https://www.iaea.or

YTÜ FEN EDEBİYAT FAKÜLTESİ

2024-2025 Bahar Yarıyılı FİZİK BÖLÜMÜ

Minimum Eylem İlkesi

Yağızhan DİNÇKURT 19022001

Danışman: Prof. Dr. Devrim YAZICI

ÖZET

Bu çalışmada minimum eylem ilkesinin tarihçesi ve ona öncülük eden teorilerin matematiksel altyapıları araştırılmıştır. Eylem ilkesi için önemli bir rol oynayan varyasyon analizi ile Euler – Lagrange denklemleri çıkartılmıştır. Eylem ilkelerinin skaler bir teori olmasının, modern uygulamalarında kazandırdığı kolaylıklar gösterilmiştir. Mevcut teoriler kapsamında problemler tartışılmıştır.

EYLEM İLKESİNİN TARİHÇESİ

Pierre De Fermat

Eylem ilkelerinin temellendirilmesinin Pierre De Fermat ile başladığı söylenebilir. Fermat, "Bir ışık ışını herhangi iki nokta arasında ilerlerken, izlediği yol en az zamanı gerektiren yoldur." şeklindeki ilkesiyle eylem yaklaşımının öncülerinden biri olmuştur [1].

Johann Bernoulli

Bernoulli 1696 yılında, bir cismin iki nokta arasında yerçekimi etkisi altında en kısa sürede alacağı yolu belirlemeyi amaçlayan brachistochrone problemi üzerinde çalışırken, Fermat ilkesinin yerçekimi etkisi altındaki cisimlerin hareketlerine de uygulanabileceğini göstermiştir. Bunu ortamın tek bir tabaka yerine çok sayıda tabakadan olduğunu varsayarak yapmıştır [2].

Pierre Louis Moreau de Maupertuis

Bernoulli'nin öğrencisi olan Pierre Louis Maupertuis 40 yıl sonra doğanın neden "en az" ilkelerine uygun hareket ettiğini anlamlandırmaya çalışırken eylem adını verdiği bir büyüklüğü

$$S = mvs$$

olacak şekilde tanımlamıştır [3]. Ancak, kendi eylem prensibini matematiksel olarak ispatlayamamıştır. Maupertuis'in eylem prensibi sadece hızın sabit olduğu sistemlerde kullanılabiliyordu. Ayrıca prensibine bir nedensellik katamamıştır.

Leonhard Euler

Leonhard Euler, eylem ilkesini ayrık sistemlerden sürekli sistemlere genelleştirmeyi başarmıştır. Euler, Maupertuis gibi çizgisel yol üzerinden aksiyon hesaplamak yerine, aksiyonu diferansiyel uzunluk elemanları üzerinden tanımlamıştır. Böylelikle aksiyonu

$$S = \int mv ds$$

şeklinde elde ederek yön değiştiren hareketlerin de eylemini hesaplayabilmiştir. Euler bu yöntemi kullanarak, kütleçekim alanında dönen cisimlerin hareketini incelemiş ve eylem ilkesinin sadece tüm yollar üzerinde toplam enerji sabit ise geçerli olacağını öne sürmüştür [4].

Joseph-Louis Lagrange

Joseph-Louis Lagrange minimum eylem ilkesine öncülük edecek sağlam bir matematiksel temel oluşturmayı başarmıştır. Ancak çoğunlukla bunu eylem ilkelerini kullanmadan veya üzerinde çalışmadan yapmıştır. 1788 yılında yayınladığı "Mécanique analytique" ile Newton mekaniği üzerine geliştirmeler hakkında yazmıştır [5].

$$\frac{d}{dt}\left(\frac{\partial L}{\partial \dot{q}_j}\right) - \frac{\partial L}{\partial q_j} = 0$$

şeklindeki Euler - Lagrange denklemleri ile mekaniğe skaler bir çözüm yönetmi geliştirmiştir.

William Rowan Hamilton

William Rowan Hamilton, 1834 yılında yazmış olduğu makalesinde "Belirli iki konfigürasyon arasında, belirli iki zamanda gerçekleşen bir mekanik sistemin gerçek hareketi, kinetik enerji ile potansiyel enerji farkının integralini en küçük yapan harekettir." ifadesini kullanmıştır ve bu şekilde kendi ismi ile anılan Hamilton ilkesini tanımlamıştır [6]. Hamilton ilkesi ile

$$\delta S = \delta \int (T - V) dt = 0$$

şeklinde minimum eylem ilkesinin modern tanımını elde etmiştir. Bu şekilde minimum eylem ilkesi günümüzde kullanılan halini almıştır ve modern fiziğin bir çok alanında, skaler bir teori olması nedeniyle kullanışlı bir matematiksel formülasyon haline gelmiştir [7].

NEDEN $\delta S = 0$ OLUR?

Bu durumu açıklamak için keyfi bir potansiyel alanda hareket eden, bir boyutlu bir sistem düşünülür. Böyle bir sistemin eylem integrali

$$S(x) = \int \left(\frac{1}{2}m\dot{x}^2 - V(x)\right) dt$$

ile tanımlanır. Sistemin eylemine küçük keyfi bir yol eklenerek varyasyona uğramış eylem

$$S(x+\eta) = \int \left(\frac{1}{2}m(\dot{x}+\dot{\eta})^2 - V(x+\eta)\right) dt$$

şeklinde bulunabilir. η çok küçük bir değişim olduğundan, kendisinin ve türevlerinin birinci dereceden olmayan terimleri ihmal edilir. Bu şartlar altında kinetik ve potansiyel enerji

$$\frac{1}{2}m(\dot{x}+\dot{\eta})^2 = \frac{1}{2}m(\dot{x}^2 + 2\dot{x}\dot{\eta}) \qquad V(x+\eta) = V(x) + \eta\frac{\partial V}{\partial x}$$

olacak şekilde elde edilir. Burada potansiyel enerji Taylor serisine açılmıştır. Enerjilerin açılmış hali eylem integraline yazılırsa

$$S(x+\eta) = \int \left(\frac{1}{2}m\dot{x}^2 - V(x)\right) dt + \int \left(m\dot{x}\dot{\eta} - \eta\frac{\partial V}{\partial x}\right) dt$$

ifadesine ulaşılır. Bu denklemde ilk integral orijinal eylem integralidir. Bu integral karşıya atılır ve eylemin varyasyonu olarak yazılırsa

$$S(x+\eta) - S(x) = \delta S = \int \left(m\dot{x}\dot{\eta} - \eta\frac{\partial V}{\partial x}\right) dt$$

denklemi elde edilir. İntegralin ilk terimine parçalı integrasyon kuralı uygulanırsa

$$\delta S = -\int \left(m\ddot{x} + \frac{\partial V}{\partial x}\right)\eta\, dt$$

şeklinde sonuç bulunur. Parantezin içine bakılırsa Newton'un ikinci yasasından ve potansiyel enerjinin kuvvet bağıntısından yani,

$$F = m\ddot{x} \qquad \frac{\partial V}{\partial x} = -F$$

ifadelerinden bu integralin sıfıra eşit olduğu açıkça görülebilmektedir. Bu şekilde eylemin varyasyonunun sıfır yaptığı gösterilir.

$$\boldsymbol{\delta S = 0}$$

SONUÇ

Çalışmada eylem ilkelerinin 200 seneyi aşkın tarihsel süreci açıklanmıştır. Lagrange'ın kendi mekanik denklemlerini bulurken D'Alembert prensibinden yola çıkmış olması, varyasyon analizine öncülük ederek matematiksel altyapı kazandırması gösterilmiştir. Hamilton'un, Lagrange'ın denklemleri üzerine eylem ilkesinin standart formunu ortaya çıkarması ve varyasyon analizi kullanarak Hamilton prensibinin genel formuna ulaştığı ortaya konmuştur. Bu süreçler matematiksel formülasyonların gösterilmesi ile detaylıca açıklanmıştır. Eylem ilkelerinin güçlü yanları kadar problemlerine de değinilmiş, doğrudan eylemin hesaplanamayacağı, sadece eylemin varyasyonunun hesaplanabileceğine değinilmiştir.

KAYNAKÇA

[1] P. de Fermat, "Ophthalmologicorum principia examinantur," S. P. Tannery and C. Henry, 1891.
[2] Johann Bernoulli, "Problema novum ad cujus solutionem Mathematici invitantur" 1696.
[3] P. L. M. de Maupertuis, "Accord de différentes lois de la nature qui avaient jusqu'ici paru incompatibles,", 1744.
[4] L. Euler, "Methodus inveniendi lineas curvas maximi minimive proprietate gaudentes", 1744.
[5] J.-L. Lagrange, "Mécanique Analytique", 1788.
[6] W. R. Hamilton, "On a General Method in Dynamics" , 1834.
[7] M. Henneaux and C. Teitelboim, Quantization of Gauge Systems, 1992.

YTÜ FEN EDEBİYAT FAKÜLTESİ

FİZİK BÖLÜMÜ

KESİRLİ TÜREV YAKLAŞIMLARININ NEWTON MEKANİĞİNE UYGULANMASI

İlayda ÇONA 19022022

Danışman: Prof. Dr. Devrim YAZICI

ÖZET

Bu çalışma, kesirli kalkülüsün tarihsel gelişimini aktararak başlar ve Leibniz dönemindeki fikirlerden Riemann–Liouville ile Caputo yaklaşımlarına uzanan kuramsal temelleri özetler; ardından klasik Newton mekaniğini tam sayı mertebeli türevlerin ötesine taşıyarak sabit kuvvet altında hareket denklemine kesirli türevler uygular ve bu sayede düzgün hız, ivme ve sarsıntı rejimleri arasında süreklilik sağlayan yeni davranışlar ortaya koyar. Çalışmanın ikinci ana bölümünde, Riesz potansiyeli kullanılarak kesirli kütle çekim modeli geliştirilir. Sonuçlar, potansiyelin uzak mesafelerde daha yavaş zayıfladığını ve galaktik ölçekte gözlenen düz dönüş eğrilerini ek karanlık madde varsayımına gerek kalmadan yeniden üretebileceğini gösterir. Çalışma, kesirli türevlerin bellek ve yayılma menzili gibi özgün özellikleri sayesinde yalnızca mekanik problemleri değil, aynı zamanda viskoelastisite, kaotik sistemler ve astrofizik uygulamalarını da kapsayan esnek ve kapsamlı bir fiziksel çerçeve sunduğu sonucuna varır.

Kesirli Türev Kavramının Doğuşu

Kesirli türev fikri ilk kez 1695 yılında Marquis de L'Hôpital ile Gottfried Wilhelm Leibniz arasındaki bir mektuplaşmada gündeme gelmiştir. Leibniz, türevlerin mertebelerinin kesirli olmasının ne anlama geldiğini soran L'Hôpital'e verdiği yanıtta, bu düşüncenin çelişkili görünmesine rağmen anlamlı olabileceğini belirtmiştir. Bu diyalog, kesirli analiz olarak bilinen alanın doğmasına öncülük etmiştir [1]. Farklı kesirli türev tanımlarının varlığı, her fiziksel sürecin belleği, yerel pürüzlülüğü ve sınır koşulları bakımından kendine özgü gereksinimler taşımasından kaynaklanır; dolayısıyla hangi yöntemin seçileceği, modellenen sistemin deneysel olarak hangi nicelikleri ölçülebilir kıldığı ve hangi ölçek aralığında etkili bir bellek yapısına ihtiyaç duyulduğuyla doğrudan ilişkilidir. 19. yüzyılda Riemann ve Liouville, tam sayı dışı türev için genel formu

$$ {}_{a}^{RL}D_{x}^{q} f(x) = \frac{d^n}{dx^n}\left(\frac{1}{\Gamma(n-q)}\int_a^x (x-t)^{n-q-1} f(t)\ dt\right) $$

denklemini ortaya koyarak tanımlarken Caputo, başlangıç koşullarının klasik türevlerle verilebilmesi amacıyla

$$ {}_{a}^{C}D_{x}^{q} f(x) = \frac{1}{\Gamma(n-q)}\int_a^x (x-t)^{n-q-1} f^{(n)}(t)\ dt $$

tanımını önerdi. Grünwald–Letnikov ise limit-fark serisi ile sayısal uygulamalar için güçlü bir çerçeve sağladı.

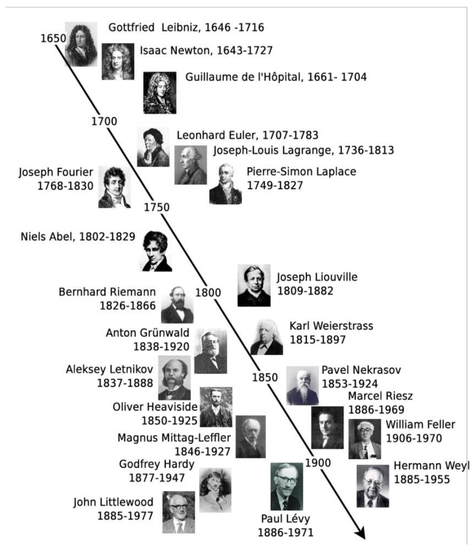

Gamma Fonksiyonu

Riemann-Liouville ve Caputo varyantı gibi neredeyse tüm kesirli türev operatörleri gamma fonksiyonunu içeren integral ifadeleriyle tanımlanır. Türev mertebesini q'ya genelleştirirken ortaya çıkan $\frac{1}{\Gamma(\ )}$ ifadesi sayesinde denklem fiziksel boyut tutarlılığını korur [2 − 3]. Bu katsayı, integral çekirdek fonksiyonunu alan altında "birim bellek" hâline getirir; yani geçmişe dair ağırlıklar $\Gamma()$ sayesinde düzgün ölçeklenir [1]. Gamma fonksiyonu, kompleks düzlemde ise $\Re(z) > 0$ koşuluyla şu şekilde tanımlanır:

$$ \Gamma(z) = \int_0^\infty t^{z-1}e^{-t}dt = \frac{e^{-\gamma z}}{z}\prod_{k=1}^{\infty}\left(1+\frac{z}{k}\right)^{-1} e^{z/k}, \gamma \approx 0.577216. $$

Kesirli Leibniz Çarpım Kuralı

Klasik diferansiyel analizde, çarpımın türevi

$$ \frac{d}{dx}(\psi\chi) = \frac{d\psi}{dx}\chi + \psi\frac{d\chi}{dx} $$

ile verilir. Ancak bu yapı, kesirli türevlerde

$$ \frac{d^{\,q}(\psi\chi)}{dx^{\,q}} = \sum_{j=0}^{\infty}\binom{q}{j}\frac{d^{\,q-j}\psi}{dx^{\,q-j}}\frac{d^{\,j}\chi}{dx^{\,j}} $$

şeklinde q kesirli mertebesine genelleştirilerek formüle edilmelidir. Aynı klasik çarpım kuralında olduğu gibi bölüm veya zincir kuralları da genelleştirilmeden direkt olarak kesirli türevler için kullanılamaz [4].

Kesirli Türev-İntegral İlişkisi

Kesirli kalkülüste "geçmişe bakan" sol operatörler I_{a+}^{q} D_{a+}^{q} ile "geleceğe bakan" sağ operatörler I_{a-}^{q} D_{a-}^{q} simetrik tanımlıdır. Türev ve integral çiftinin geçmişe ve geleceğe bakan tanımlar için temel bağıntıları aynıdır. Yani, $D_{\pm}^{q} I_{\pm}^{q} f(t) = f(t)$ tam terslik sağlar.

Newton Mekaniğinin Genelleştirilmesi

Newton'un ikinci yasası, zamana göre kesirli mertebeli türev kullanılarak

$$ \frac{d^q x(t)}{dt^q} = \frac{\boldsymbol{F}}{m} = f $$

Şeklinde genelleştirilebilir. Kesirli mertebeden bu diferansiyel denklemin çözümü katsayıların başlangıç konum, hız, ivme vb. değerler taşıdığı özel ve homojen çözümlerden meydana gelir. $q = 2$ için klasik sabit ivmeli hareket,
$q = 1$ için sabit hızlı Aristotalesçi hareket, $q = 3$ için ise sabit jerk'li hareket temsil edilir. Ayrıca q'nun kesirli mertebeleri (ara eğriler); tam sayı mertebeli çözümler arasında makul bir şekilde interpolasyon yapmaktadır; yani kesirli mertebeli ara çözümler, $q = 1$ ile $q = 3$ (özellikle $q = 2$) durumları arasında kalan, beklenebilecek davranışlardır.

$$ x(t) = \frac{d^{-q}f}{dt^{-q}} + c_1 t^{q-1} + c_2 t^{q-2} + \cdots + c_k t^{q-k} = \frac{f t^q}{\Gamma(1+q)} + c_1 t^{q-1} + c_2 t^{q-2} + \cdots + c_k t^{q-k}. $$

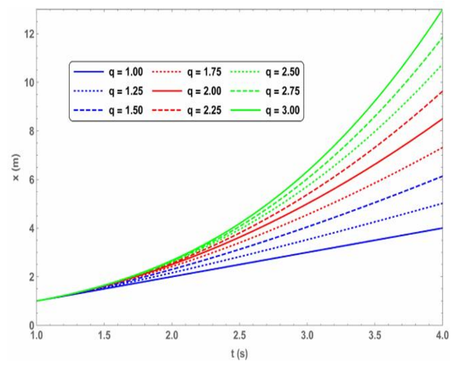

Gravitasyonel Potansiyel

Riesz potansiyeli, klasik Poisson denkleminden sapma gösteren sistemleri modellemek amacıyla geliştirilmiştir. Bu yaklaşım, klasik Laplace operatörü ∇ yerine kesirli mertebeden bir diferansiyel operatör olan kesirli Laplace operatörü $(-\nabla)^{q/2}$ kullanılarak genelleştirilmiş Poisson denklemi ile ifade edilir. Bu bağlamda, potansiyel fonksiyonu *V(r)* sabit yoğunluklu küresel bir dağılım altında kesirli Poisson denkleminin analitik çözümünü sunar ve q parametresi aracılığıyla sistemin klasik dışı davranışlarını temsil edebilme esnekliği sağlar.

$$ V_{RZ}(r) = V(r) = -\frac{G}{a}\int_{R^3}\frac{dM}{(s/a)^q} = -\frac{G}{a}\int_{R^3}\frac{\rho(r')\,d^3r'}{\left(|r-r'|/a\right)^q} $$

Küre yarıçapı R_o ve sabit yoğunluk ρ_0 için iç-dış potansiyel şu bileşik ifade ile verilir:

$$ V(r) = -\frac{2\pi G\,\rho_0}{a^{1-q}\,(q-2)\,(q-3)\,(q-4)\,r}\times \begin{cases} (r+R_0)^{3-q}[\,r-(3-q)R_0\,] + (R_0-r)^{3-q}[\,r+(3-q)R_0\,], & 0 \le r \le R_0\,; \\ (r+R_0)^{3-q}[\,r-(3-q)R_0\,] - (r-R_0)^{3-q}[\,r+(3-q)R_0\,], & r > R_0\,. \end{cases} $$

Mertebe $q = 2$ sınırında klasik $-\frac{G\,M}{r}$ potansiyeline geri döner; $q < 1$ aralığında ise potansiyel uzak mesafede daha yavaş sönerek galaktik ölçekte düz dönüş eğrilerini üretebilecek "uzun kuyruk" davranışı gösterir [5]. Q ara değerler için kütleçekimsel potansiyel, Newton potansiyeline kıyasla daha uzun menzilli bir etki gösterir. Uzak mesafelerde *V* Newton'a göre daha büyük kalır.

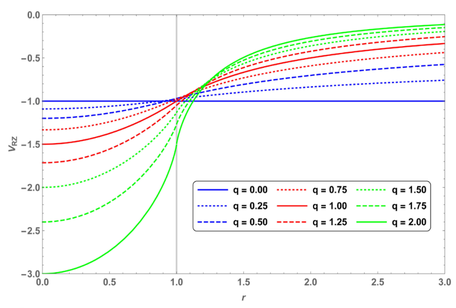

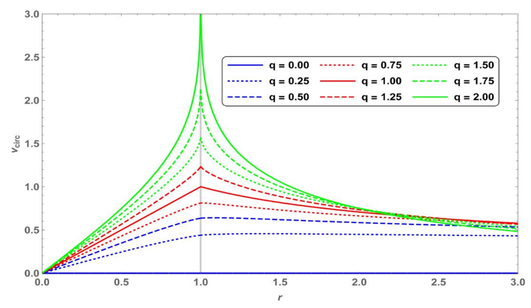

Alan $-\int_r^{R_0} g(r)\ dr$ ifadesinden türetilir ve buna karşılık dairesel hız.

$$ v_{çev}(r) = \sqrt{r\,\frac{|\boldsymbol{F_{RZ}}(r)|}{m}} = \sqrt{\left|\frac{dV_{RZ}(r)}{dr}\right|} $$

İfadesi ile elde edilir. Grafiklere bakıldığında, kesirli mertebenin $q = 1$ 'den $q \to 0$ aralığına inmesiyle dış yörüngelerdeki hız profillerinin hızla düzleştiği görülür; $q = 0.25$ için çizilen mavi noktalı eğri büyük yarıçaplarda neredeyse tamamen yataydır. Bu davranış, galaksilerin Newton kuramının öngördüğünden yüksek ve hemen hemen sabit kalan gözlemsel dönme hızlarını andırır. Henüz galaktik veriyle sayısal eşleştirme yapılmamış olsa da, düşük q değerlerinin — özellikle $q \to 0$ sınırında — karanlık madde varlığını taklit edecek ölçüde düz hız profilleri üretebileceği kuramsal olarak ortaya konmuştur; dolayısıyla sonuçlar, literatürdeki popüler alternatif kütle-çekim yaklaşımlarına zemin hazırlar.

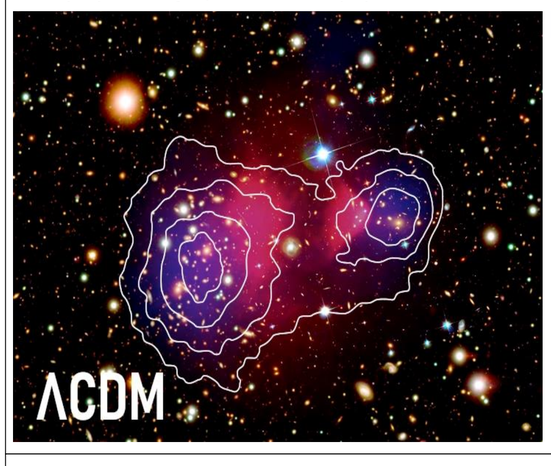

Model	Mesaj
MOND	Newton ivmesinin altındaki rejime yumuşak geçiş ekleyerek galaktik düz dönüş eğrilerini karanlık madde varsayımsız açıklamayı hedefler.
TeVeS	Skaler-vektör-tensor karışımıyla MOND'u genel görelilikle uyumlu kılar ve ışık bükülmesiyle kozmoloji testlerine genişletir.
BIMOND	İki etkileşen metrik arasındaki farktan doğan terimlerle hem Newton hem MOND davranışını tek eylemde birleştirir.
Calcagni'nin Fraktal Kozmolojisi	Uzay-zaman boyutunu ölçeğe bağlı değişken kabul ederek kesirli kütleçekimin kozmolojik genişleme ve kuantum graviteye yansımasını araştırır.
Bullet Cluster	Bu kümede kütle lenslemesi ile baryonik gaz ayrışması, çoğu alternatif modelde hâlâ sınayıcıdır; kesirli mertebe q ≈ 0,8 seçimi lenslemeyi baryonlarla yeniden eşleştirme umudu sunar.

KAYNAKÇA

[1] Herrmann, R. (2014). *Fractional calculus: An introduction for physicists*. World Scientific.

[2] Liouville, J. (1832). Sur le calcul des différentielles à indices quelconques. *Journal de l'École Polytechnique*, 13, 1–68.

[3] Caputo, M. (1967). Linear models of dissipation whose Q is almost frequency independent—II. *Geophysical Journal International*, 13(5), 529–539.

[4] Podlubny, I. (1999). *Fractional differential equations* (Vol. 198). Mathematics in Science and Engineering. Academic Press.

[5] Miller, K. S. & Ross, B. (1993). *An introduction to the fractional calculus and fractional differential equations*. Wiley-Interscience.